QUANTUM OPTOELECTRONICS: NANOSCALE TRANSPORT IN A NEW LIGHT

A Dissertation
Presented to
The Academic Faculty

By

Jose Ignacio Gonzalez

In Partial Fulfillment
Of the Requirements for the Degree
Doctor of Philosophy in Chemistry

Georgia Institute of Technology

May 2006

QUANTUM OPTOELECTRONICS:
NANOSCALE TRANSPORT IN A NEW LIGHT

Approved by:

Professor Robert M. Dickson, Chairman
School of Chemistry and Biochemistry
Georgia Institute of Technology

Professor C. David Sherrill
School of Chemistry and Biochemistry
Georgia Institute of Technology

Professor Mostafa A. El-Sayed
School of Chemistry and Biochemistry
Georgia Institute of Technology

Professor C. P. Wong
Materials Science and Engineering
Georgia Institute of Technology

Professor Thomas M. Orlando
School of Chemistry and Biochemistry
Georgia Institute of Technology

Date Approved: March 31, 2006

ACKNOWLEDGEMENTS

I thank my family and especially my parents, Jose Ignacio and Amparo Beatriz, sisters, Mariapilar and Marcela, and Danielle for their love, support and encouragement. Thanks are extended to my supervisor for stimulating dialogue and to my fellow group members for their help and friendship. I thank my thesis committee and Professor Mike Barnes for their help and support. Additional thanks go to my early mentors, Tom Pemble, Jane Crum, and Chris Free.

TABLE OF CONTENTS

LIST OF FIGURES

LIST OF SYMBOLS AND ABBREVIATIONS

AC	alternating current
AFM	atomic force microscope
APD	avalanche photodiode
CCD	charge coupled device
CFD	constant fraction discriminator
DC	direct current
DOS	density of states
EDS	energy dispersive spectroscopy
E_F	Fermi energy
EL	electroluminescence
FET	field effect transistor
FRET	fluorescence resonance energy transfer
FWHM	full width at half maximum
G	giga (10^9)
GPIB	general purpose interface bus
$\hbar$	reduced Planck's constant ($h/2\pi$)
HOMO	highest occupied molecular orbital
Hz	Hertz (cycles per second)
IETS	inelastic electron tunneling spectroscopy
K	Kelvin or kilo (10^3)
k	wavevector or wavenumber (scalar)
k_B	Boltzmann's constant
LED	light emitting diode
LUMO	lowest unoccupied molecular orbital
M	mega (10^6)
MIM	metal insulator metal
n	nano (10^{-9})
NA	numerical aperture
NDR	negative differential resistance
p	momentum or pico (10^{-12})
RF	radio frequency
SAM	self-assembled monolayer
SEM	scanning electron microscope
STM	scanning tunneling microscope
TAC	time to amplitude converter
TEM	transmission electron microscope
TTL	transistor transistor logic
μ	micro (10^{-6})

SUMMARY

Common to molecular electronics studies, nanoscale break junctions created through electromigration also naturally produce electroluminescent arrays of individual gold nanoclusters spanning the electrodes. These nanoclusters exhibit bright, field-dependent emission in the near infrared (650–800 nm). Intensity autocorrelation of spatially isolated individual nanocluster emission driven at high electrical frequency (f_{AC} ~ 200 MHz) reveals antibunched electroluminescence at room temperature. These results demonstrate the single quantum nature of several-atom gold molecules and suggest their use as room-temperature electrically driven single-photon sources.

In addition, the electrode-molecule couplings are readily probed by the individual molecule's light emission resulting from inelastic transport between them. The individual electroluminescent gold clusters act as very sensitive probes of the local electric field to reveal details about the immediate nanoenvironment including the electrode-cluster coupling strength, electrode restructuring, and local electrostatic charging. Most importantly, single-molecule electroluminescence is a non-controversial, corroborative tool to track nanoscale transport dynamics in real time through a molecular electronic device.

Arrival time stamping of detected photons demonstrates that charge injection to the clusters is directly modulated by dynamic coupling to individual electrodes. These several-atom nanoclusters ($Au_{\sim 18\text{-}22}$) electroluminesce due to inelastic electron tunneling into cluster electronic energy levels. AC electrical excitation with time-stamping of photon arrival times enables fast and local tracking of electrode-nanocluster coupling

dynamics. The electrode-nanocluster coupling rate fluctuates by nearly an order of magnitude and, due to the asymmetry of the electromigration process, exhibits preferential charge injection from the anode. Directly reporting on (and often facilitating) nanoscale charge transport, time-tagged single-molecule electroluminescence reveals a significant mechanism for nanoscale charge transport in nanoscale gold break junctions, and offers direct readout of the electrode-molecule interactions that can be correlated with current flow.

I. TRACKING ELECTRONS WITH PHOTONS

1.1 Nanoscale Charge Transport in Perspective

Advancements in the physical sciences and industrial innovation have steadily driven a decrease in the dimensions of functional electrical elements striving for faster, more efficient devices.[1] At the most fundamental level, these breakthroughs were ushered in by developments in classical wave models of long range transport and an understanding of how wave-like charges interact with band structures of metallic and semiconductor lattices. The identification and development of solid-state materials with different electronic band structure and the ability to tune the free carrier density in these materials by ion-doping was also important. This framework provided a suitable description for much of the physics governing long range charge flow in bulk materials but could not capture the particle-like behavior of electrons manifested in quantum-confined materials with dimensions comparable to the electron Fermi wavelength.[2-4] Under low potentials and small current, these behaviors appear in the range of several nanometers (~10^{-9} m). Studies of charge transport below this critical scale require a quantum mechanical treatment of the molecular, cluster, or nanoparticle electronic structure interacting with the electric field.

First proposed by Aviram and Ratner,[5] the idea of using individual molecules as active electronic devices for current gating and rectification introduced a laundry list of challenges for both theorists and experimentalists. Transport through a molecule was initially described as the scattering current though a system of interacting conductance

channels (analogous to molecular orbitals) with transmission and reflection coefficients as given by Landauer's formalism.[6] While a powerful first approximation for conductance, this picture is valid only at low temperatures and small bias and ignores inelastic effects such as thermal scattering and coupling to molecule vibronic transitions.[7, 8] Complementary models have since been proposed that deal with inelastic molecular transport coupled to molecule transitions in two-dimensional films[2, 9, 10] and chemisorbed to an STM tip[11, 12] as well as interactions with phonons[13] and thermal baths.[14] However, much of the complexity of typical computational models used to calculate even resonant transport through a molecular wire arises in dealing with the geometry of the contacts (and the spatial dependence of the electrostatic potential) and the electrode-molecule coupling.[15-17] Because the molecule's electronic structure is modified by coupling to metal contacts, a molecular wire is more accurately modeled as an "extended molecule" which contains the original molecule and surrounding electrode regions.[16]

Enabling true nanoscale transport measurements and revealing a variety of new nanoscale phenomena, the development of powerful lithographic techniques[18-24] and conducting probe microscopies for imaging and manipulation of matter has paved the way for elaborate routes to attach various types of molecules and nanostructures to electrodes. The ability to manipulate individual molecules and nanostructures and attach electrodes to them is the first step in building molecular electronics devices. By placing a single molecule between electrical contacts, the discrete molecular states can in principle be exploited as Landauer channels to give the new wire unique conductance characteristics which depend on the bridging molecule's electronic structure. Conducting probe atomic force microscopy (AFM) has been used to measure current through self-

assembled monolayers (SAMs) of long carbon chains as well as individual functionalized molecules diluted in the SAMs.[25, 26] Scanning tunneling microscopy (STM) of similar systems[15, 27-30] shows evidence of conformational switching and negative differential resistance (NDR) due to resonant tunneling through individual molecule states. However, these demonstrations, while very promising in the pursuit of molecular wires and electronic devices, were not free from controversy. For example, current flow through SAMs was found to be much more complex than previously imagined encompassing many alternate transport pathways involving several molecules. Even when the electrodes are placed over slightly more conductive molecules dispersed in the SAMs, a large contribution to the current arises from lateral hoping between different alkyl chains of the SAM. In addition, these measurements are often plagued with reproducibility issues brought about by the conductance dependence on the SAM's dynamics and mechanical stability. A loosely-packed SAM is more floppy, which increases dynamics while reducing the electrode-molecule coupling and lowering the average conductance.

1.2 Break Junctions and Three Terminal Devices

Much of the progress in molecular wire fabrication has been made in the area of metal breakjunctions. Gentle breaking of a metal wire (usually gold) produces a very narrow, electrically-accessible gap for the study of individual atoms, molecules, or other nanostructures. Initially, nanoscale gaps were produced by mechanical breaking of notched gold wires.[31] Deposition of molecules into the gap from solution was reported both before[22] and after[21] the breaking process. The successful inclusion of a molecule in the junction cannot be verified by imaging or other direct means. Instead, the existence of

a molecular bridge is merely inferred from monitoring the total junction conductance throughout the course of fabrication. This method results in the creation of two-terminal tunnel gaps, but mechanically controlled breakjunctions are not amenable to gating by a third electrode. This problem was solved by selective breaking of a gold wire deposited over an oxide layer and gate electrode. Selective breaking of the active wire was achieved by electromigration, the same mechanism responsible for circuit failure under large current densities.[23] The combination of a gate electrode with the convenience of electromigration-induced breakjunctions has enabled the study of nanoscale transport phenomena (Fig. 1.1) presumably through individual organometallic complexes,[32, 33] carbon fullerenes,[24, 34, 35] and metal clusters.[36-38] While both methods produce small tunneling gaps, the resulting electrodes and their interactions with any bridging molecule are difficult to characterize because of high structural heterogeneity, spontaneous production of molecule-like metal clusters and surface structures, electrode restructuring, and dynamic coupling to the molecule.

The gate electrode in these devices is, in some respects, quite similar to the gate electrode of a three-terminal field effect transistor (FET). In both systems, the gate provides an electric field that shifts the chemical potential of the junction's active region relative to the chemical potentials of the electrodes. In an FET, the gate electrode is separated from the other electrodes by an insulating oxide and placed in between the transistor source and drain (Fig. 1.2(a)). The size of the gap between the source and drain electrodes is comparable to the size of the gate electrode, so the active region (whose electrochemical potential is modulated) is limited to this interelectrode gap. When a gate

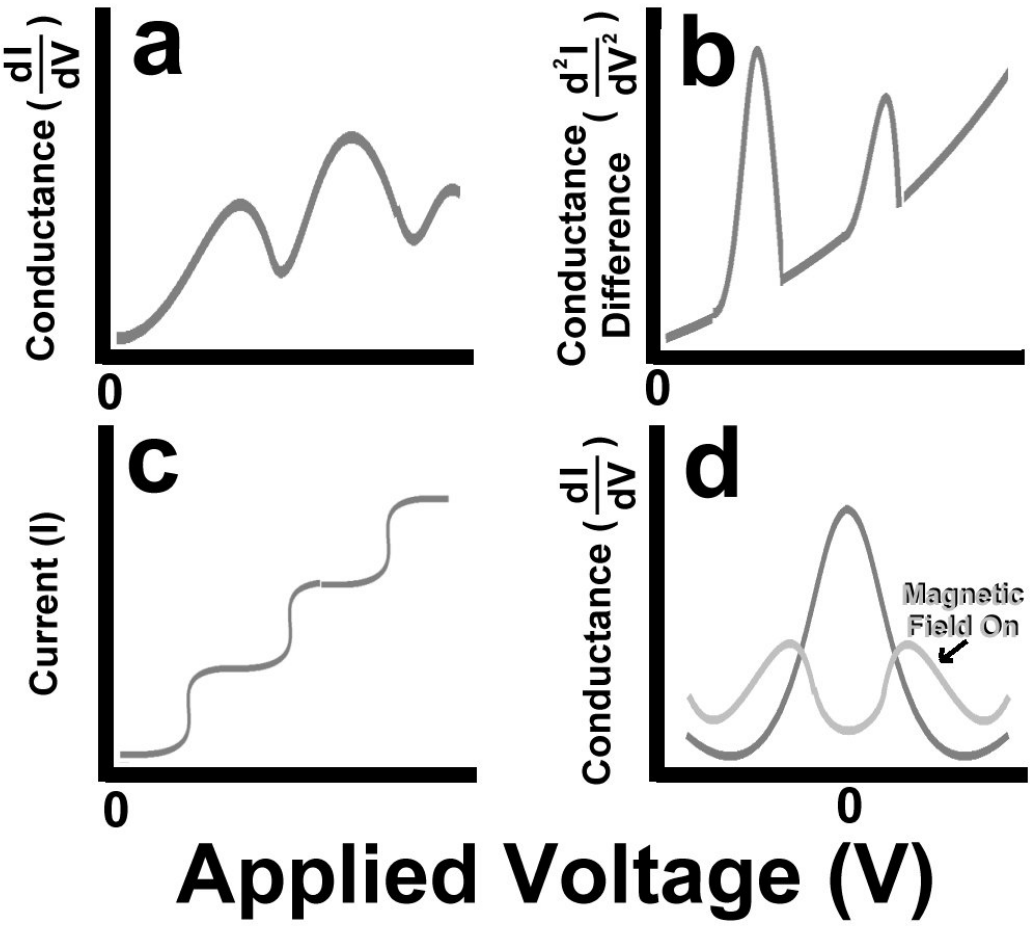

Figure 1.1. Examples of nanoscale transport phenomena. (a) Resonant (elastic) tunneling can occur when the chemical potential of the electrode is set to match one of the molecule energy states. At low temperature, a plot of the molecular wire's conductance vs. applied voltage reveals NDR and well defined peaks due to increased tunneling at the molecule energy levels[22]. (b) Tunneling can also proceed inelastically by coupling to molecule vibrations or electronic transitions. In molecule-doped metal-insulator-metal tunnel junctions, a plot of the change in conductance with respect to voltage contains spectral peaks which match optically observed molecule vibrational modes[76]. (c) Coulomb blockade effects due to quantized charging, or single electron tunneling, has been observed in a variety of nanostructures[32, 38, 86] when the thermal energy falls below the coulomb charging energies. The observed "staircase" in the plot of current vs. voltage is reversible with approximately equal step sizes resulting from the energy needed to add one electron to the molecule. (d) At low temperatures, the screening of a localized spin (e.g., a magnetic atom[32, 33] or gold quantum dot[36, 37] with an unpaired electron) by surrounding conduction electrons results in a conductance peak at zero bias. This effect is known as Kondo-assisted tunneling, and the resulting peak intensity decreases logarithmically with temperature. In the presence of a magnetic field, Zeeman splitting of the molecule spin states results in a splitting of the zero bias conductance peak.

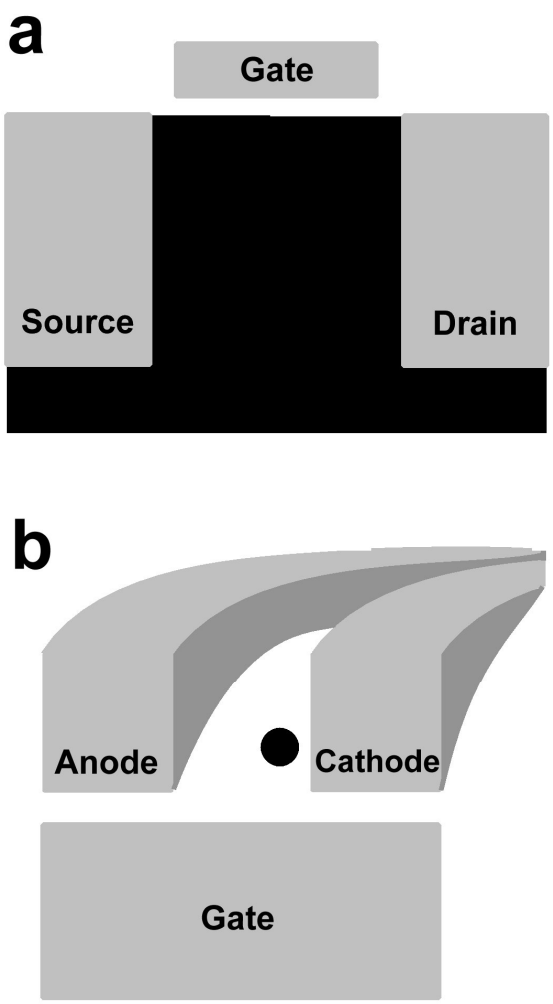

Figure 1.2. Diagrams of three-electrode devices on the meso- and nano-scale. (a) The gate electrode of a mesoscopic field effect transistor (FET) spans the active area of the device but does not overlap with the source and drain electrodes. The active region, through which current is gated, separates the source and drain electrodes completely and uniformly. (b) The gate electrode of a three-terminal molecular junction is proportionally much larger than its mesoscale counterpart. In this device, the gate covers the entire tunnel gap as well as the source and drain electrodes. The molecule (black dot) is very small (~1 nm) compared to much larger cross-sectional area of the source and drain (~80 nm).

potential is applied, the electrochemical potential of the inter-electrode gap is shifted relative to the chemical potential of the drain electrode.

The relative dimensions of three-terminal nanoscale break junctions are very different, and therefore, the relative size of the active region whose chemical potential is affected by the gate will be very different too. First, even the smallest state of the art electrodes defined by complex lithographic schemes are still nearly two orders of magnitude larger than the bridging molecule or nanostructure (Fig. 1.2(b)).[24, 32, 33, 36] This drastic size difference means that a vast cross-section of the junction is unobstructed by the molecule and, therefore, available for charge transport through alternate mechanisms such as conduction through temporary electrode short circuits, field emission and non-resonant transport, as well as resonant and inelastic transport through electromigration-formed metal clusters within the junction.[39, 40]

Second, while the gate electrode is enormous compared to the molecule, it is also larger than the source or drain. This is to be expected since fabricating a gate electrode that spans only a region the size of the active molecule would be extremely difficult, and creating a break junction via electromigration precisely over the tiny gate electrode would be even more challenging. In addition, the field created by such a small electrode would depend highly on its atomic structure, position, orientation, etc. and its effect on the molecule's chemical potential would also be unclear.[16] Instead, typical three-terminal molecular junctions use a very large gate electrode, and much smaller source and drain electrodes are defined upon it (Fig. 1.2(b)).[24, 33] The large gate electrode is separated from the electromigration-defined tunnel gap (~1-10 nm) by an insulating oxide layer. Solution deposition of molecules into the gap is inferred from a conductance increase. In this type

of setup, the gate is much larger than the inter-electrode gap (and bridging molecule) and extends over the edges of the source and drain electrodes. In principle, this means that these electrode edges (not just the molecule and gap) are also subject to electrochemical potential modification by the gate's electric field. However, this effect is likely small compared to the effect felt by the isolated molecular chemical potential in the gap. The net result is a gate-induced chemical potential shift of the molecular density of states relative to the source and drain electrodes.[7, 24]

1.3 Alternative Transport Mechanisms and Other Considerations

Despite great strides in both theoretical sophistication and experimental ingenuity, some technical difficulties have brought the field of molecular transport to a virtual stand-still.[3, 16, 41] One challenge of studying transport through a molecular bridge is in characterizing all of the different mechanisms that contribute to the total current flow. Even when the electrodes are strongly coupled to the molecule's energy levels, resonant transport will be accompanied by a relatively small amount of inelastic transport and non-resonant field emission.[2, 39, 42] It is unclear how much current may flow through the molecular channels before the inelastic contribution drives enough intramolecular vibrational relaxation to destroy the molecular bridge (or its connection to the electrodes). In the case of electromigration-induced junctions, the most dominant of these mechanisms is not resonant transport through the molecular bridge. Rather, most of the current is due to field emission of electrons from one electrode to the other. Because the interelectrode distance in these junctions is on the order of ~1 nm, a 1-V bias produces very high field strengths (about a billion Volts per meter) and significant current density

extending from one electrode out to the other. In addition, electron tunneling may couple inelastically to molecular vibrational or optical transitions. Relaxation rates for optical transitions are on the order of 1 GHz, and vibrational rates are typically much higher (~100 GHz). The amount of inelastic transport depends on the electrode-molecule coupling strength, which gives rise to a coupling rate that competes with the vibronic transition's rate of relaxation. At coupling rates exceeding these transition rates, virtually all of the resonant transport is elastic. When the relaxation rate is comparable to or higher than the coupling rate, inelastic electron tunneling becomes a significant transport mechanism. In this case, resonant transport into an excited molecular state is followed by relaxation (or energy dissipation in the molecule) and resonant transport from the ground state. As mentioned above, however, the source and drain electrodes are much larger than a typical small-molecule diameter, leaving plenty of room for unobstructed non-resonant field emission across the junction.[43-45] At such high field strengths, dynamic restructuring of the electrodes may also play a large role in transport by creating temporary conducting protrusions of material extending into the junction. In more extreme cases, such protrusions could fully span the junction to cause short circuits between the electrodes.[46, 47] Electrode restructuring near the molecular bridge can affect transport by modulating the electrode-molecule coupling as well as the energy distribution of resonant tunneling electrons. These observations detail the complexity of electrodes commonly used in molecular electronics experiments, as nearly all so-called "molecular" effects are observed from the electrodes alone without the addition of exogenous molecular conductors.[36-40, 48, 49]

Another difficulty lies in dealing with complex (and often dynamic) electrode-molecule interactions. As mentioned above, the electronic structure of an electrically contacted molecule is inherently modified by coupling to the electrode density of states. Attempts to understand electrode-molecule transport must therefore include a description of the contact couplings.[7, 16] In practice, high control of the contact coupling can be achieved by covalent bonding of an organic molecule to metallic electrodes via electronegative linker atoms like sulfur.[18, 20-22, 25-27, 30] At cryogenic temperatures, the strong (covalent) electrode-molecule coupling produced reproducible structures in the current-voltage characteristics at the expense of the original (unbroadened) molecule DOS. Preservation of transport phenomena unique to molecular channels (i.e., NDR) brought about by the molecule's discrete density of states should be readily achieved by the inclusion of an insulating tunnel gap between the molecule and its metallic electrodes. Such a gap can provide sufficiently low coupling strengths to preserve discrete molecular states but allows resonant electrode-molecule tunneling.[2, 10] The tunnel gap solves the problem of molecule DOS modification but lessens the need for structural control that requires, once again, characterization of the contact couplings. However, this larger tunnel gap reduces current flow, increasing the likelihood of transport through alternate channels as described above. While theoretical treatments of the couplings has improved dramatically,[16] experimental characterization suffers from low sensitivity (and signal-to-noise ratio) in current measurements requiring long integration times that prohibit observation of fast coupling dynamics.

1.4. On Single Molecules and their Dynamics

The promise of molecular electronics is based on the notion of building molecular wires that can act as nanoscale analogs of conventional electronic devices like transistors and diodes.[5] But, as mentioned above, the general idea of linking metal electrodes by a single bridging molecule (and thereby restrict the passage of electrons to conduction channels made up of the bridge's molecular orbitals) is mired in controversy and poses serious challenges. The transistors and diodes of conventional electronics are expected to perform the same task in identical fashion several billions of times per second for a span of many years. Such remarkable performance is possible only because the dynamics of these devices' state variable (their charge) are well-understood and can be controlled under operating conditions. In single-molecule experiments, the state variable of interest (whether it's current flow, fluorescence intensity, emission wavelength, radiative lifetime, three-dimensional orientation, atomic conformation, or electrode-molecule coupling) fluctuates stochastically in time (Fig. 1.3).[50-57] This means that the time trajectory of a single molecule's state variable can never be exactly reproduced. Fortunately, the statistical properties of a molecule's trajectory, which give rise to some distribution, are reproducible and can be extracted to further our understanding of that molecule and its surroundings. However, differences in local environments between two neighboring molecules ensure that even "identical" molecules will exhibit unique state variable distributions. Such environmental sensitivity and detail is obscured by ensemble measurements (consequently, this is the main reason conventional mesoscale devices appear so stable). Herein lies an obvious question: can we harness a stochastically fluctuating molecular property to form a reliable device? Attempts to control these fluctuations clearly require an understanding of their origins.

At a fundamental level, individual molecules are highly responsive probes of their own local nanoenvironment.[51] Dynamics arise because a molecule's observable properties fluctuate as it stochastically samples its potential energy surface, and this surface is dynamically modified by changes in the surroundings. Even in the absence of environmental interactions at low temperature, a molecule's state may change by tunneling through a potential energy barrier.[58-60] At room temperature, for the most part, thermal or environmental fluctuations (like interactions in condensed phase and amorphous systems) and photoinduced transitions or excitation into a triplet state give rise to single-molecule dynamics.[51]

The study of single-molecule dynamics clearly requires the ability to measure a molecule's state variable with reasonable time resolution while excluding all contaminating information about other nearby molecules. Fast measurements require high sensitivity and signal-to-noise ratio (low background) for a given observable. In the case of fluorescence detection, the isolation of light from just one molecule can be accomplished by several methods. In dilute samples, the most straight forward approach involves confocal microscopy. By placing a small pinhole at the focal plane prior to detection, out-of-focus light is rejected, enabling detection from an area comparable to the light's diffraction limit.[61]

In more concentrated samples, confocal microscopy does not provide the needed level of background rejection, and other methods must be used. Instead of illuminating a large section of the sample and using confocal microscopy, a very small section of the sample can be illuminated. One way of doing this is through two-photon excitation of the fluorophores.[62, 63] Another strategy involves the use of a small illuminating probe. Near-

field scanning optical microscopy (NSOM) is a method for measuring single-molecule fluorescence and observing its dynamics within concentrated samples.[64-66] The NSOM method involves the excitation of a fluorescent molecule from only a few nanometers away in the molecule's so-called "near-field". This is accomplished by scanning the sample with a transparent probe whose sides have been coated with a reflective metal sheath. The scanning probe provides topographical information about the surface and also serves as a waveguide for illumination of the sample surface. The single molecule fluorescence is detected from below through a transmissive substrate. Because the probe's cross-section is smaller than half the fluorescence wavelength, NSOM also produces sub-diffraction limit resolution. And, since the NSOM tip itself can perturb the properties of the fluorescing molecule, this technique was useful for studying the effects of nanostructures near an emitter. Interactions between the molecule and the small electric field generated by the tip's sheath have a quenching effect on the emission which shortens the lifetime.[65] By measuring the molecule's emission lifetime at different positions with respect to the tip, it is possible to map out the tip's small local field. Since the NSOM tip itself strongly perturbs the single-molecule under observation, the technique is not widely used. The modification of a molecule's density of states by nearby structures is well-known and serves as another example by which individual molecules dynamically probe their environment. Proper characterization of this effect is particularly relevant to transport through electrode-coupled molecules.

The ability to assign arrival times to a stream of detected photons forms the basis of single-molecule dynamics studies in the range of 10^{-7}-10^{3} seconds.[51] Creating a time series of a molecule's fluorescence intensity, lifetime, orientation, electrode coupling, etc.

allows observation of dynamics that are characteristic of single molecule behavior. For example, switching back and forth between two or more emission states (Fig. 1.3(a)) allows tracking of the time spent in different emissive states,[54] and splitting the light over several crossed polarizers allows tracking of an emitting dipole's orientation.[67] This can also be accomplished by collection through a high numerical aperture objective and imaging on a CCD to determine the emission pattern's angular dependence (Fig. 1.3(b)).[57, 68] Tracking a single molecule's three-dimensional orientation in a heterogeneous host environment can be used to characterize the host's dynamics. Dispersing a single molecule's fluorescence with a grating allows time-dependent monitoring of its emission spectrum (Fig. 1.3(c)).[56] Together with autocorrelation analysis (Fig. 1.3(e)), single-molecule spectroscopic data can provide information about the rates of fluctuation between different molecule states.[50] The time scales and power dependence of these fluctuation rates can reveal the nature of the mechanisms giving rise to them (i.e., two-level tunneling, thermal, or photoinduced) and can provide information about the molecule's *environmentally-dependent* potential energy surface.

Conformation dynamics of larger molecules are readily tracked by fluorescence resonance energy transfer (FRET).[69, 70] Dichroic mirrors can be used to simultaneously measure the fluorescence intensity of two different dyes in a sample. The efficiency of energy transfer between the molecules will scale as R^{-6}, where R is the distance between the molecular dipoles. If the excitation spectrum of one of these dyes (called an acceptor) is made to overlap with the emission spectrum of the other (called a donor), the energy transfer at small distances will be very efficient. Exciting the donor molecule when the two dyes are far apart causes only the donor to fluoresce. But, when the dyes are close

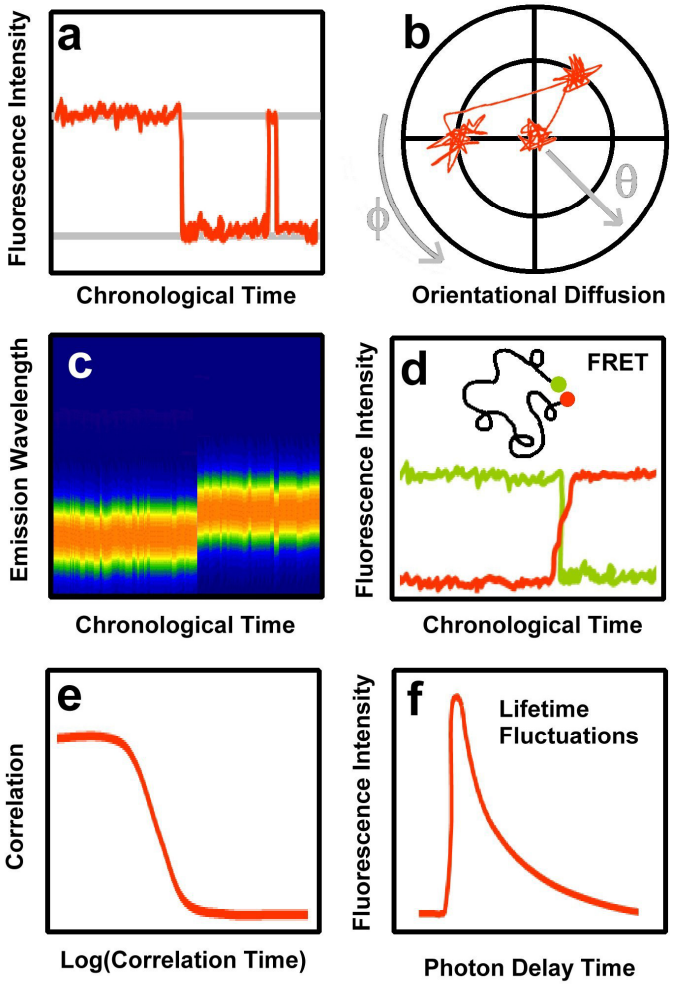

Figure 1.3. Examples of techniques in single-molecule dynamics experiments. (a) The fluorescence intensity time trajectory from a single molecule shows on/off blinking behavior. (b) The polar plot of a single molecule's three-dimensional orientation changing in time can be used to characterize the dynamics of the host matrix. In this plot, each line segment represents a constant time spacing of the orientation measurements. (c) Spectral shifts of a single molecule's emission spectrum, whether from thermal spectral diffusion or photoinduced spectral hopping, can reveal a lot about the molecule's potential energy surface. (d) The time trajectories of a FRET donor-acceptor pair can be used to measure dynamic changes in nanoscale distance. When attached to the same macromolecule, FRET pair fluorescence can be used to track single molecule conformation dynamics. (e) The time constants involved in all of the above time trajectories can be understood through correlation analysis in one or several dimensions. (f) Fluorescence lifetimes are measured by time correlated single photon counting and, along with real-time tagging of all the photons in the trajectory, can provide measurements of interaction dynamics between the molecule and its nano-environment.

enough for energy transfer, the donor fluorescence will decrease in favor of more acceptor emission. The high sensitivity at very close distances provided by FRET forms the basis of a measuring tool on the nanoscale (Fig. 1.3(d)). Attaching a donor-acceptor pair on opposite ends of a macromolecule allows monitoring of the molecules conformational dynamics since different conformations produce slightly different donor-acceptor distances. Dispersing a low concentration of labeled molecules in condensed phase enables the study of conformational dynamics that can be correlated to environmental fluctuations.[71]

Dynamics on the scale of 10^{-11}-10^{-6} seconds can be tracked by time-correlated single photon counting methods whereby the arrival of photons from the sample is synchronized to a modulated excitation (such as a pulsed laser).[51, 72] Coupled with the time-tagging technique described earlier, such a setup allows real-time tracking of a single molecule's fluorescence lifetime (Fig. 1.3(f)). More advanced so-called photon-by-photon techniques based on Bayesian analysis and information theory can extract higher order correlation functions to and determine intensity change points from very short time trajectories. [52, 73] This kind of analysis is a powerful tool that can be used to extract information about the system beyond what the one-dimensional correlation provides. The use of multiple detectors also allows photon correlation measurements as will be discussed in chapter 5.

An interesting solution to the problems of tracking molecular charge transport dynamics discussed in the previous sections may lie in the detection of photons created by inelastic processes rather than detecting the electrons themselves.[49] Commonly called electroluminescence (EL), these photons are generated as a direct result of inelastic

charge transport and electron-hole recombination so the resulting light intensity is electric field dependent. In addition, photon detection offers higher sensitivity and faster time-response over electron (current) measurements, and in principle, can provide the emitting molecule's orientation as well as specify its position to well below the light's diffraction limit (this is true of far-field measurements if well isolated and observed with high signal-to-noise ratio).

1.5 Electroluminescence in the Bulk

The generation of light as a byproduct of inelastic charge transport is well-understood in bulk semiconductor optoelectronic devices like light emitting diodes (LEDs)[1]. A diode is an electrical element exhibiting charge transport only under forward bias. When the voltage polarity is reversed (and the voltage is kept reasonably low), a diode passes no significant current. In the case of semiconducting gallium arsenide (GaAs), each gallium atom (group III) has three electrons in its outermost shell and each arsenic atom (group V) has five, resulting in an average of ~4 outer shell electrons per atom of the pure bulk crystal. The addition of "p-type" dopant atoms from group II (like zinc) slightly decreases this average number resulting in increased hole mobility. Conversely, addition of "n-type" dopants from group VI (like selenium) increases electron mobility. The interface, or junction, formed by linking n- and p-type GaAs constitutes the active region of a GaAs pn-diode. Under forward bias, the difference in charge carrier mobilities within the different device regions will cause electrons (from the n-type side) and holes (from the p-type side) to accumulate at the pn interface (Fig. 1.4(a)).

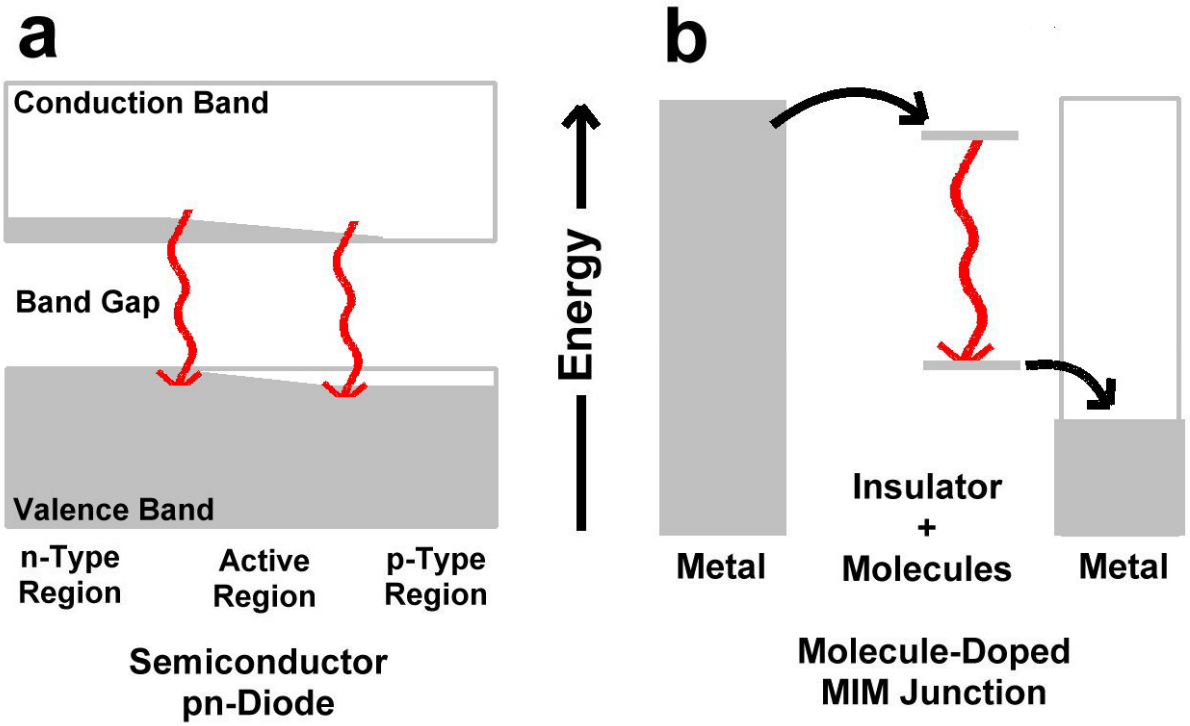

Figure 1.4. Diagrams of a light emitting diode (LED) and inelastic electron tunneling spectroscopy (IETS). (a) Recombination in a forward-biased pn-junction light emitting diode is shown for comparison with (b) inelastic electron tunneling coupled to a molecule vibronic transition within the insulating layer of a metal-insulator-metal junction.

The term "semiconductor" refers to a material whose electronic structure exhibits a low density of states around the material's Fermi energy (called the band gap), with a high density band at higher energy (called the conduction band) and a high density band at lower energy (called the valence band).[1] As in all materials, electronic transitions in semiconductors must obey the laws of conservation of energy and momentum. Light emission (as well as light detection) in semiconducting materials typically occurs through electronic transitions between the conduction and valence bands.[74] From conservation of energy, it follows that the emitted photons will have energies equal to the difference between the electrons' initial and final states. The photon energy usually closely matches the band gap energy. In the pn-diodes discussed above, a forward bias results in electron-hole separation with an electron in the conduction band and a hole in the valence band. This charge separation is typically called an exciton because the electron and hole can be thought of as a single pair. As mentioned above, the electron-hole pair can recombine radiatively to produce a photon (thereby conserving energy in the system), but recombination must also conserve momentum. In the event of such a recombination, the momentum of the photon is given by[1]

$$p = \hbar k_{ph} = \hbar \frac{2\pi}{\lambda}, \tag{1.1}$$

where ħ is Planck's constant divided by 2π, k_{ph} is the photon wavevector, and λ is its wavelength. A similar expression is used to describe the electron and hole momenta, i.e.,[1]

$$p_{e,h} = \hbar k_{e,h}, \tag{1.2}$$

and the energy of a free electron is given by[1]

$$E_e = \frac{p^2}{2m_0} = \frac{\hbar^2 k_e^2}{2m_0}, \tag{1.3}$$

where m_0 is the free electron mass which has a value of 9.109 x 10^{-31} kg. However, a calculation of the electron and hole energies in a semiconductor crystal is not as straight forward because the carrier effective mass depends on the material's dispersion relation, ε(k). The dispersion relation of a system describes its energy density at momentum ħk, and in general, one can define an effective mass, m*, for electrons and holes which is given by[1]

$$m_{e,h}^* = \hbar^2 \left[\frac{d^2 \varepsilon(k_{e,h})}{dk_{e,h}^2} \right]^{-1}. \tag{1.4}$$

Thus, the effective mass depends on the second derivative of the density of states with respect to k and is usually stated in units of m_0. It follows from equations 1.3 and 1.4 that electrons only have constant effective mass in materials for which the dispersion relation is (at most) quadratic in k. When the dispersion relation reaches a relative maximum or minimum, as is often the case in radiative recombination, the function can be approximated as quadratic in k and an effective mass can be estimated.

Taking into account both conservation of energy and momentum, the energy of a photon created from recombination of an electron-hole pair is then given by[1]

$$\hbar\omega = E_e - E_h = \left[E_c + \frac{\hbar^2 k_e^{\,2}}{2m_e^*}\right] - \left[E_v - \frac{\hbar^2 k_h^{\,2}}{2m_h^*}\right], \tag{1.5}$$

where the subscripts c, v, e, and h are used to indicate conduction band, valence band, electrons, and holes, respectively. From equation 1.1, we can calculate the wavenumber of the emitted photon. For example, a photon with an energy of 1.8 eV has a wavelength of about 700 nm corresponding to a k_{ph} value of ~1.4 x 10^{-4} $\mathring{A}^{-1}$. The photon k-value is several orders of magnitude smaller than reasonable electron or hole wavevector in semiconductor devices, and as such, the conservation of momentum in electron-hole recombination can be assumed when the hole momentum matches the electron momentum. When this condition is met, recombination is said to proceed via a "vertical" or "direct" transition. An electron and hole with mismatched momentum may also recombine by coupling to lattice vibrations (this is known as an "indirect" transition) or through non-radiative Auger processes by which a third charge carrier is excited into the conduction band. For a direct band gap transition, we may set the electron and hole wavenumbers equal to each other and rewrite equation 1.5 as

$$\hbar\omega = E_{bandgap} + \frac{\hbar^2 k^{\,2}}{2}\left(\frac{1}{m_e^*} + \frac{1}{m_h^*}\right) = E_{bandgap} + \frac{\hbar^2 k^{\,2}}{2m_r^*}, \tag{1.6}$$

where m_r* is the reduced mass of the electron-hole quasiparticle (the exciton).[1] From equation 1.6, we see that the lineshape reflected in the emission spectrum will clearly

depend on the carrier occupation function and the density of states function of the semiconductor material. Diodes made from direct bandgap semiconductors, like GaAs, act as light emitting diodes because conduction band electrons and valence band holes recombine radiatively to generate light with energy close to the crystal's bandgap energy (~1.5 eV for doped GaAs at room temperature) as described above.[75]

Another interesting example of inelastic transport occurs in metal-insulator-metal (MIM) junctions through which tunneling is mediated by inelastic coupling to molecular vibronic transitions within the insulating layer of alumina (Al_2O_3).[2, 76-80] This type of transport forms the basis for Inelastic Electron Tunneling Spectroscopy (IETS) in which the metallic electrode chemical potential is scanned relative to the molecule-doped alumina density of states (Fig. 1.4(b)).[2, 81] A plot of the junction's second derivative in current with respect to voltage, $\frac{d^2I}{dV^2}$, versus voltage reveals peaks at energies corresponding to molecular vibrational modes (see Fig. 1.1(b)). Electron tunneling can also proceed inelastically by coupling to molecular electronic transitions to produce photons.[77, 78] As in the semiconductor example, this light generation mechanism also depends on the tunneling current and can, in principle, be used as a reporter of current density. While very useful in this regard, MIM junction current and light emission measurements contain information about a large ensemble of molecules and alternate transport pathways. Robust, room-temperature light emission from spatially-resolved nanoscale sources that can be correlated with current flow can provide a convenient route to controlled studies of fundamental nanoscale transport phenomena.

1.6 Electroluminescence on the Nanoscale

In analogy to bulk electroluminescence, EL from a single molecule or nanostructure can potentially be used to study electron transport through its molecular orbitals. There are a handful of examples of nanoscale electroluminescence in the literature to date. Field dependent electroluminescence has been demonstrated from individual electrically-contacted semiconducting carbon nanotubes as well as colloidal semiconductor nanorods and quantum dots. In these setups, light generation is driven by a constant DC field. Injection of charge carriers from both sides of the long carbon nanotubes produces excitons that radiatively decay, and light emission from nanorods is attributed to inelastically scattered electrons coupling to the semiconductor bandgap transition. In both cases, the emission is from individual nanostructures and highly polarized, but the size of the recombination region along the nanostructure is quite large. In addition, these structures posses very shallow confinement potentials, precluding single-electron transport above cryogenic temperatures. Fabrication of electrically-contacted semiconductor quantum dots has also been demonstrated using epitaxial deposition of a small amount of p-type material on an n-type surface. This strategy results in a nanoscale pn-junction that produces electroluminescence under DC and pulsed electrical excitation. At liquid helium temperatures (for which k_BT falls below the quantum dot's weak electron confinement potential), this structure was shown to behave as a single quantum system with antibunched emission. At higher temperatures, the EL's quantum mechanical nature is lost. All of these nanoscale electroluminescent systems are quite interesting in their own right, and under the right operating conditions, can provide a great deal of information about the underlying transport phenomena. But, while several experiments have been conducted to show the field and temperature dependence of these

mechanisms, attempts to address the transport's time-dynamics have been limited to a few exceptions (i.e., silver nanocluster transport dynamics reported by Lee, et al.[39]).

The remainder of this dissertation describes a new class of noble metal quantum dots that exhibit strong fluorescence in aqueous solution,[82-85] as well as electroluminescence within deposited films.[39, 48, 49] Behaving as multielectron artificial atoms, these nanogold species should provide facile routes to producing strong single-photon emitters, even approaching telecommunication wavelengths. The sub-nm metal quantum dots have size-tunable emission throughout the visible and near infrared, with Au_{31}, for example, absorbing at 780 nm and emitting at 870 nm with high quantum yield.[82] Low density arrays of 18–22 atom Au nanoclusters can also be produced *in situ* during electromigration-induced nanoscale break junction formation,[40, 48] allowing facile electro-optical interrogation of individual strongly electroluminescent species. Even at room temperature, single gold nanodot electroluminescence enables real-time tracking of local electrode-molecule transport fluctuations on the single electron level, an impossible feat by purely electrical measurements.

II. TECHNIQUES IN QUANTUM OPTOELECTRONICS

2.1 Overall Experimental Scheme

The general setup for creating, characterizing, and controlling gold nanocluster electroluminescence is rather uncomplicated because of the relative simplicity of the apparatus and high stability of these structures at room temperature. In general, the experimental apparatus (Fig. 2.1) has three parts: electrical excitation, a gold nanojunction, and detection.

The electrical excitation is provided by either a power supply (DC field), a crystal-based oscillator driven by a power supply (AC field), or a high-frequency function generator (Pulsed field with many frequency components). After leaving the source, an electrical signal can be conditioned with attenuators, amplifiers, filters, or inverters to achieve the desired excitation profile. This excitation profile can be monitored with an oscilloscope (see f. below). The gold nanojunction is produced by electromigration (see c. below) on top of a transparent glass coverslip and the entire assembly (including electrical access to and from the excitation source) is held under vacuum for the duration of the experiment. This portion of the apparatus will be discussed below in greater detail (see b. below).

The detection part of the apparatus is often the most complex and includes electrical measurements as well as light detection. Electrical measurements are carried out by different instruments depending on magnitude and modulation frequency of the current (see d. below). For direct current, the power supply's ammeter or (for currents

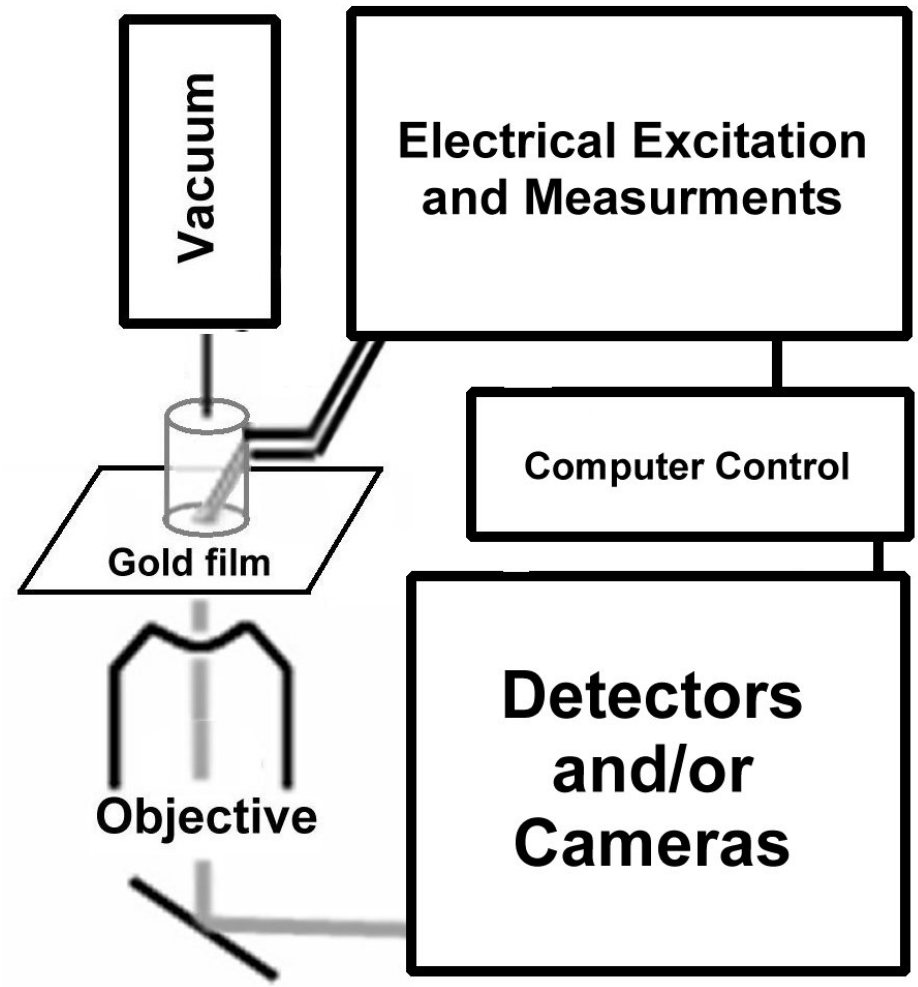

Figure 2.1. Schematic arrangement of nanoscale electroluminescence experiments. The experimental apparatus has three parts: electrical excitation, a gold nanojunction, and detection. The electroluminescence from gold nanoclusters within the break junction is imaged using a high numerical aperture, oil-immersion objective (Olympus; either 100X 1.4NA plan-apochromat, or 60X 1.45NA plan-apochromat) on an inverted microscope (Olympus; either IX-70 or IX-71). All excitation and detection parameters can be computer controlled and synchronized to each other.

exceeding ~5 mA) an additional picoammeter may be used. For alternating current or modulation by pulse sequences, the voltage across a transformer coil (placed around the cathode) may be monitored by an oscilloscope.

Light detection is done through the transparent window upon which the gold junction is created. The coverslip (and the rest of the vacuum assembly) is placed atop an inverted optical microscope and electroluminescence is collected through a high numerical aperture objective. The light may be sent to an imaging monochrometer, a charged-coupled device (CCD) camera, a photomultiplier tube, or an avalanche photodiode (APD). Prior to detection, spectral filters and/or spatial filters (e.g., a pinhole or optical fiber) may be used to exclude undesired light, and beam splitters may be used to distribute the emission over several devices (see g.-i. below).

The electrical signals produced by the APDs are sent to a single photon counting module where they are time-tagged and counted (see h. below). Detector pulses can be tagged relative to the beginning of the experiment (this tag is called a *macro*time) to produce a real time trace of the photon intensity, and they can also be tagged relative to the arrival of pulses synchronized to the excitation source (called a *micro*time) to produce an intensity vs. time histogram of the emission.

2.2 Metal Film Preparation and Patterning

To prepare electroluminescent gold junctions, new microscope coverslips are first cleaned by ozonation and placed in an e-beam or filament evaporator. Gold films approximately 20-nm in thickness are deposited on the glass coverslips. The thickness can be confirmed by profilometry. Gold films are reduced to ~150-μm wide strips simply

by using a new razor blade. The ends of the strips are coated with small drops of silver paint no more than ~2 mm apart that act as electrical contacts. The coverslip forms the bottom window of a microscope-mounted vacuum chamber (< 10^{-5} Torr) with the vacuum forcing electrical contact between spring-loaded electrodes and the silver paint. Fully assembled, the gold wire resistance prior to break junction formation is < 10 Ω.

2.3 Break Junction Formation and Impedance Monitoring

Once fully assembled and evacuated as described in the previous section, the gold film is ready for electromigration-induced break junction formation. The spring loaded electrodes which contact the gold film are accessible on the outside of the vacuum assembly and connect directly to a DC power supply. Application of a constant 1 to 3 VDC, ~150 mA for ~10 s produces a break junction near the center of the Au film, creating highly emissive Au nanoclusters within the nanoscale gap. Junction formation can be monitored by measuring the current through the circuit. The final gold nanojunction resistance and density of electroluminescent clusters created depend on the precise details of the electromigration process (i.e., the voltage, time, and peak current) as well as the level of vacuum, the method of film deposition, and film thickness. A stronger vacuum and thinner film produce more electroluminescent clusters. Films produced by filament evaporator tend to be more heterogeneous than those deposited in the e-beam evaporator; this heterogeneity translates into a higher cluster density within the junction. The electrodes and gap may be imaged by a variety of methods as described in section e. below.

2.4 Junction Electrical Response Measurements

Characterization of the junction electrical response is accomplished by measuring the current in one of two ways. DC measurements of high currents (> ~5mA) the power supply ammeter (Agilent E3646A) is used. For lower DC currents, a picoammeter (Kiethley 6485) placed in series between the excitation source and the sample can be used. The current measurements are then recorded through a computer via General Purpose Interface Bus (GPIB) connection. The GPIB interface also allows synchronization to optical measurements. For AC or pulsed current measurements, we use a digitizing oscilloscope to monitor the voltage across a transformer coil (Solar Electronics) surrounding the junction cathode (Fig. 2.3,4). Numerical integration of the induced voltage yields the time dependent current.

2.5 Film Imaging and Energy Dispersive Spectroscopy

Imaging of the gold film before and after electromigration-induced breaking can be accomplished by optical and electron microscopy methods. Because the gold film is very thin and not completely opaque to visible light, the electrodes can be imaged on an optical microscope by standard transmission or reflection microscopy methods. Transmitted or reflected light from a lamp is imaged using a high numerical aperture, oil-immersion objective (Olympus; either 100X 1.4NA plan-apochromat, or 60X 1.45NA plan-apochromat) on an inverted microscope (Olympus; either IX-70 or IX-71) and measured with a CCD camera (Roper Scientific, MicroMax; or Andor, Ixon). The nanoscale gap is too small to image optically but was imaged with a scanning electron microscope (SEM) (Hitachi 3500H). The elemental composition of the electrode region

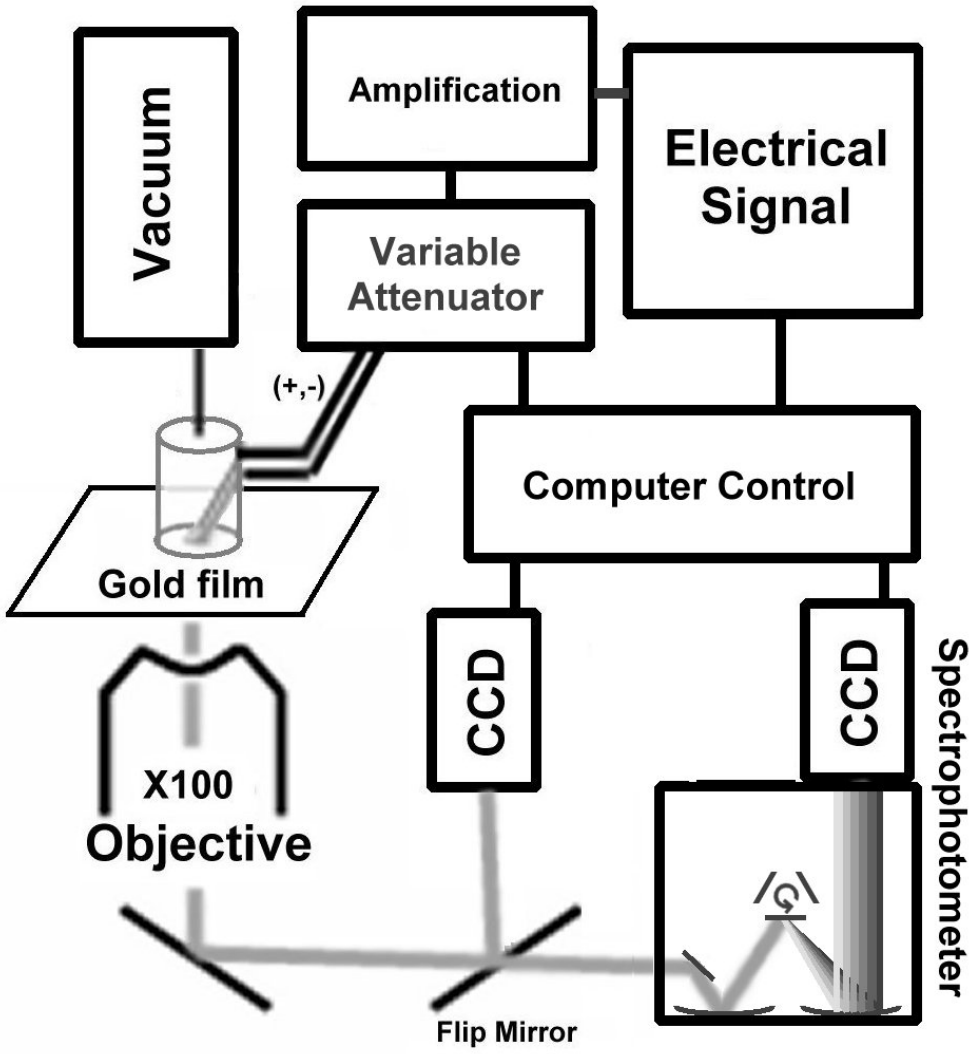

Figure 2.2. Schematic arrangement for electroluminescence emission spectroscopy. The electrical signal is a high frequency oscillator (Minicircuits, ZOS-300) driven by a DC power supply (Agilent E3646A). The signal is then sent to an amplifier and attenuated. The emission is passed to either an imaging monochromator (Acton, sp300i (300 mm) 150 1/mm grating) or a CCD (Roper Scientific, MicroMax; or Andor, Ixon) for alignment purposes. The excitation frequency and attenuation as well as both cameras are computer controlled.

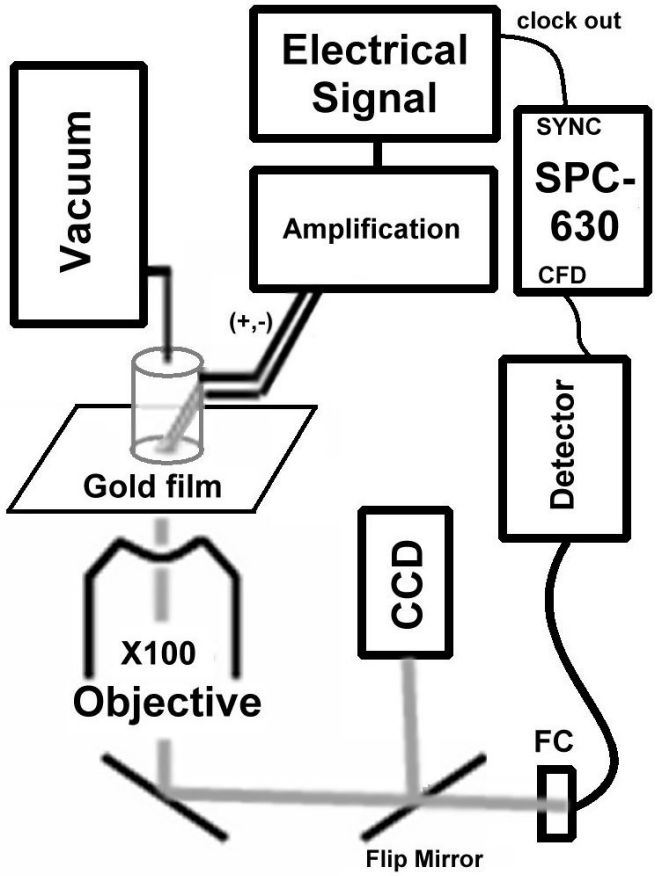

Figure 2.3. Time-tagged, time-correlated single photon counting setup for measurement and imaging of gold nanodot electroluminescence. An electrical waveform generator and amplifier excites the gold electromigration-induced break junction held under vacuum (10^{-5} Torr) by an oil-free turbo pump (Varian). The electroluminescence is collected through a 1.4NA, 100X microscope objective and either imaged on a CCD or focused through an optical fiber and passed to a Perkin Elmer Avalanche Photodiode (APD). The detector signal is passed to the CFD (Stop) of a Becker & Hickl SPC-630 photon counting module and synchronized by either the frequency-divided excitation clock (Pulse Research Lab, PRL-260NT) or an external clock (Start).

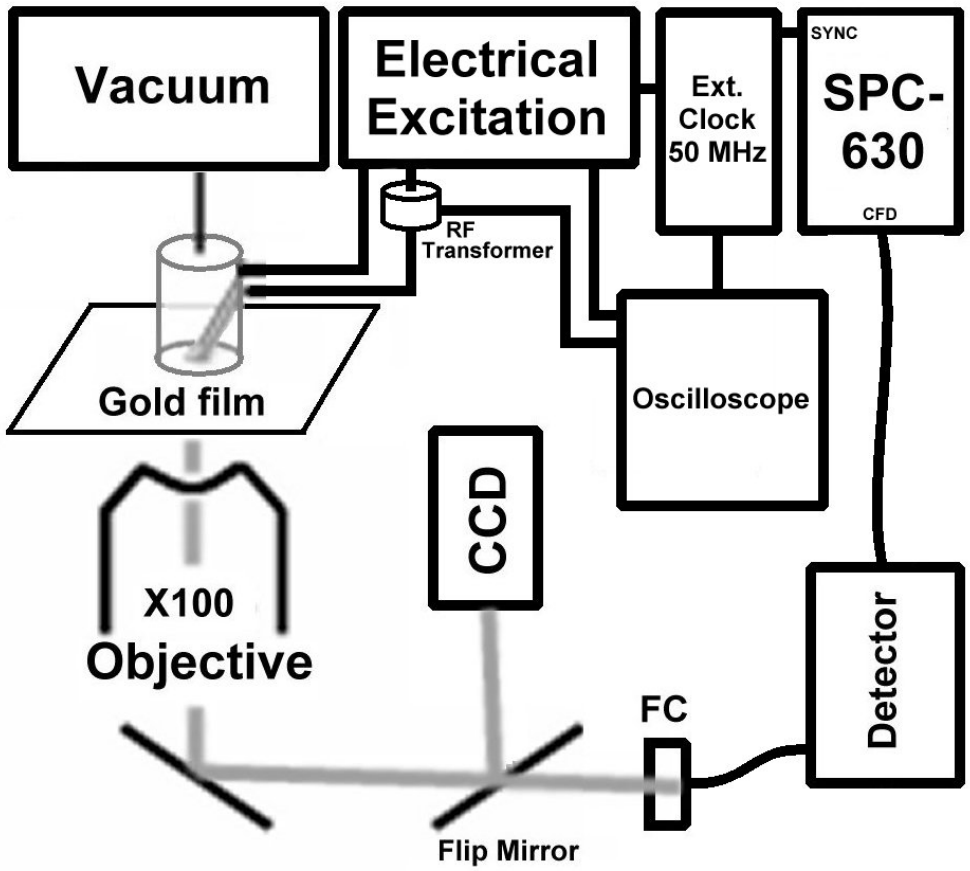

Figure 2.4. Time-correlated single photon counting and wide-field imaging setup for measurement and excitation spectroscopy of gold nanodot electroluminescence. An electrical function generator (Datron 2000) excites the gold electromigration-induced junction held under vacuum (10 microTorr) by an oil-free turbo pump (Varian). A multichannel digitizing oscilloscope monitors the excitation signal from the function generator and the total junction RF current from a current probe (Solar Electronics 9203-1) placed around the cathode. The electroluminescence is collected through a 100X microscope objective and either imaged on a CCD or focused through an optical fiber and passed to a Perkin Elmer Avalanche Photodiode (APD). The detector signal is passed to the Constant Fraction Discriminator (CFD) of a Becker and Hickl SPC-630 photon counting module and synchronized by an external 50-MHz clock (SYNC). The same external clock is used to trigger the electrical function generator and all oscilloscope measurements.

surrounding the nanoscale gap was determined by energy dispersive spectroscopy (EDS). The 2.98 keV, and 0.53 keV lines of silicon, and oxygen (respectively) were measured at 1 micron increments along a line perpendicular to the nanoscale junction. To control for the substrate's oxygen content, the ratio of the oxygen to silicon lines was measured from a bare section of the coverslip and from a freshly deposited gold film. The remaining oxygen at each point is attributed to the electromigrated gold film and a relative gold to oxygen ratio can be estimated by comparing to gold line intensity.

2.6 Electroluminescence Excitation Schemes

Electroluminescent gold junctions were excited by three different methods: DC excitation (Agilent E3646A), AC excitation (Minicircuits, ZOS-300), and two-pulse excitation (Datron 2000) which emulates one full period of an AC field. The relevant parameters for each method are voltage magnitude and polarity (DC mode), amplitude and frequency (AC mode), and each pulse's amplitude, polarity, width, and interpulse delay (two-pulse mode). The parameters can be controlled by GPIB interface and externally or internally synchronized to optical and electrical measurements. The precise excitation profile can be recorded using an oscilloscope.

2.7 Electroluminescence Imaging and Emission Spectroscopy

The electroluminescence from gold nanoclusters within the break junction is imaged using a high numerical aperture, oil-immersion objective (Olympus; either 100X 1.4NA plan-apochromat, or 60X 1.45NA plan-apochromat) on an inverted microscope (Olympus; either IX-70 or IX-71) with a CCD camera (Roper Scientific, MicroMax; or

Andor, Ixon). Alternatively, an imaging monochrometer (Acton, sp300i (300 mm) 150 1/mm grating) can be used to collect emission spectra. All cameras can be externally triggered to synchronize the image acquisition to changes in the excitation parameters (Fig. 2.2).

2.8 Electroluminescence Time-Stamping and Decay Measurement Schemes

Time-dependent and correlation (see i. below) measurements of the electroluminescence were carried out using one or two fiber coupled APDs. An optical fiber (ranging in core diameter from 62.5 to 200 microns) routes light from a microscope-coupled fiber launcher to each APD (Fig. 2.3). A fused fiber splitter can also be used to act as a 50/50 beam splitter for distributed light collection on two APDs. The microscope end of the fiber acts as a spatial filter much like a pinhole to reject unwanted light and helps to spatially isolate an individual cluster of interest. The microscope fiber launcher can be attached to the microscope side port or trinocular head to allow for easy switching between different modes of detection (e.g., CCD camera and APD, or CCD camera and imaging monochrometer). Of course, beam splitters can be used to collect light using two or more detectors at once, and these schemes are limited by the available EL intensity and each detector's sensitivity.

The electrical signal out from the APD is a digital TTL pulse and must be inverted and attenuated before it is sent to a single photon counting board (Picoquant, Time Harp 100; or Becker & Hickl SPC-630). The board has two inputs: a sync channel (labeled "sync"; which is typically sent pulses coinciding with the start of each excitation signal period) and a signal channel (labeled "cfd" on the SPC and "Start" on the Time

Harp; which is typically sent the inverted, attenuated APD signal); both inputs lead to a constant fraction discriminator (CFD), time-to-amplitude converter (TAC), and an analog-to-digital converter. The signal from several detectors can be sent to the SPC's "cfd" channel by using a router purchased from Becker & Hickl. The APD signals are registered by the board to create a two-part time tag composed of a macrotime and a microtime. The macrotime represents the photon arrival time with respect to the beginning of the experiment and can be thought of as "chronological time". In reality, the macrotime coincides with the arrival of the sync pulse immediately preceding photon detection. Using the macrotime tags, a real time trace of the EL intensity can be constructed to study the system dynamics. The resolution of macrotimes registered by the SPC-630 is 50 ns.

The other part of the tag, the microtime, represents the photon arrival time with respect to last detected sync pulse. Using the microtime tags, intensity vs. time histograms can be compiled to measure the emission decay traces. The resolution of microtimes registered by the SPC-630 can be adjusted to either 256 or 4096 channels of the TAC window. The microtime range is limited by the size of the TAC window requested by the user, but the microtime range is determined by the delay between two sync channel pulses. If each sync pulse corresponds to one period of the excitation, this means that at most one period of the excitation will appear in the window. Several excitation periods can be squeezed into the data window by dividing the sync frequency in one of two ways: a dividing factor can be specified in the SPC control panel (divides the frequency by factors of two up to 16) or an external frequency divider (Pulse Research Lab, PRL-260NT) may be used (divides by any integer factor up to 256). The

position of the emission in the TAC window can be adjusted by the inclusion of a digital delay module (Stanford Research, DTG) between the APD and the board/router. The histogram of microtimes from photons having a selected sub-range of macrotimes represents the emission decay trace from some subset of the experiment. Analogously, the chronological or macrotime trace from photons having a selected sub-range of microtimes represents the time-gated emission. Numerical analysis of large time-tag arrays can be preformed by a variety of methods.

2.9 Photon Interferometry Scheme

For measuring the photon correlation in gold nanocluster electroluminescence, a 50/50 beam splitter was placed on the microscope side port before two fiber launchers attached to two APDs in a Hanbury-Brown and Twiss interferometry arrangement (Fig. 2.5). The APD signals were sent to the Time Harp board (one to each channel) to produce a histogram of inter-photon arrival times. Prior to reaching the board, the signal from the APDs was inverted and attenuated to conform to board voltage and polarity specifications (the Picoquant board requires negative NIM pulses). In addition, the signal from one of the APDs (the one connected to the sync channel) was delayed by ~75 ns using an analog delay module (Ortec 425A). The region of interest of the coincidence vs. time histogram is the so-called “zero delay” time representing the time of simultaneous two-detector photon detection. There are some useful methods to ensure that this region is within the TAC window.

The most reliable method for adjusting zero-delay for proper placement within the TAC window requires a modulated photon source with an adjustable excitation period. A

pulsed laser diode with adjustable pulse frequency may be used, but AC or pulse-mode electroluminescence is especially well suited for the task. In this method, inter-photon arrival time histograms for ensemble EL driven at several different AC frequencies are collected. Similar to an intensity autocorrelation, these histograms are all symmetric about the true zero-delay. This means that unlike all other times in the histogram the position of zero-delay is insensitive to the AC driving frequency. Thus, overlaying all of the histograms reveals one un-shifted peak which corresponds to zero-delay. The position of this peak in the TAC window can be adjusted with the analog delay module.

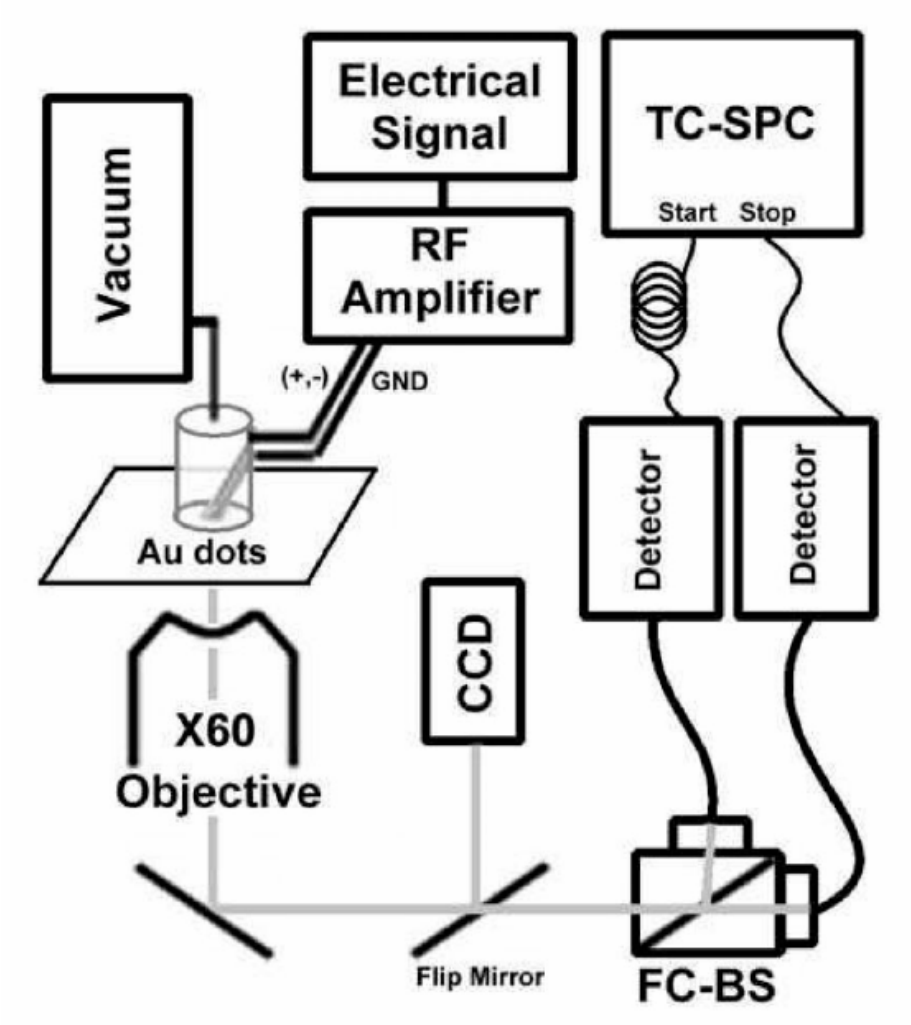

Figure 2.5. Schematic of Hanbury Brown and Twiss interferometer for single molecule electroluminescence intensity correlation measurements. Electroluminescence from electrically contacted gold nanodots (10^{-5} Torr) was projected onto a CCD camera through a high numerical aperture (NA = 1.45) oil-immersion 60X microscope objective. After further optical expansion of the image (1.6X), nanoclusters were positioned such that their spatially resolved emission was equally split, and aligned into two 100 μm multimode optical fibers coupled to single-photon sensitive avalanche photon diodes (APDs). Electrical pulses from the two detectors are inverted, delayed with respect to one another, and sent to the ‘‘start’’ and ‘‘stop’’ channels of a time-to-amplitude converter in a time correlated single-photon counting board (TC-SPC, Picoquant, TimeHarp 100). Start-stop photon pairs (coincidence counts) were recorded as a function of relative delay τ to produce an excellent approximation of the intensity correlation function, $g^{(2)}(\tau)$, at short times. This measurement reflects the true intensity autocorrelation in the limit of short delays with respect to the inverse count rate. The 50-ns window in τ is well within the range afforded by our observed average count rate of ~10 kHz.

III. TRACKING ELECTRODE-MOLECULE TRANSPORT DYNAMICS WITH NANOSCALE ELECTROLUMINESCENCE

While crucial to the understanding of nanoscale transport physics, the non-equilibrium dynamics of electrode-molecule coupling by an external electric field are not well characterized and become washed out in conventional time-averaged molecular electronics experiments.[24, 32, 33, 41, 87, 88] As even state-of-the-art nanofabricated electrodes[22, 23] are much larger than molecular dimensions, many conduction pathways and mechanisms of charge transport through and around the molecule are active, further obscuring interpretations. While bulk conduction through an insulating layer typically occurs via capacitive charge-discharge cycles or short range tunneling, charging effects on the nanoscale become quantized and tunneling dominates through available resonant channels.[4, 89] Routinely demonstrated in the absence of high efficiency resonant pathways,[24, 32, 38, 89-91] quantized charging and coulomb blockade is exhibited at temperatures for which available thermal energy is smaller than the energy level spacings of a bridging nanoparticle.

When an external field is strong enough to overcome the deep confinement potential posed by the metal-insulator interface, nonresonant tunneling (field emission) ensues and decreases exponentially with interelectrode distance.[92] Introduction of a molecule into the junction mediates tunneling of electrons resonant with its discrete energy levels by providing a non-zero charge density within the barrier potential.[22] Depending on the strength of coupling to each electrode, molecule-mediated tunneling processes can also proceed inelastically as the injected electrons lose energy to transitions

between vibrational or electronic states. Nearly 40 years ago, Lambe and coworkers reported peaks in the differential conductance of molecule-doped metal-insulator-metal junctions.[76] The peaks, appearing at a few tens of meV, were both IR- and Raman-active vibrational modes of the dopant molecules resulting from inelastic tunneling. More sophisticated versions of these experiments have been carried out on the single molecule scale within three-terminal devices[24, 34, 93, 94] and scanning tunneling microscopes.[28, 95, 96] Electrically-driven mechanical vibrations of fullerenes[24, 34] and optical transitions of individual noble metal nanoclusters[39, 48] and semiconductor quantum dots[93, 94] were also recently reported. Such inelastic tunneling through electronic transitions was predicted[2] in 1968, and electroluminescence (EL) was observed soon thereafter.[77, 78]

3.1 Nanoscale Electroluminescent Breakjunctions

Recently, we have studied electroluminescent metal-insulator-metal junctions to probe optoelectronic dynamics of individual small gold,[39, 48] silver,[97, 98] and copper[40] molecular-scale clusters. While nanocluster emission is highly dependent on the material, all cluster systems exhibit bright EL under both DC and AC electric fields. Important both as electrodes in nanoscale electronics[22-24, 34, 36, 38] and as size-tunable quantum dots,[82] nanoscale gold has many promising optoelectronic properties. Even many-body electron spin correlations attributed to small gold clusters have been observed[36] in recent low-temperature electrical measurements of nanoscale gold break junctions. Because we can track the electrode-nanocluster coupling dynamics by counting EL photons, single molecule electroluminescence constitutes the first corroborative and non-controversial readout of nanoscale current flow. While an inefficient charge transport pathway,

inelastic electron tunneling through radiative electronic states provides a non-invasive probe of nanoscale junction dynamics. With high frequency AC excitation such that charge injection and excited state lifetimes are comparable to the excitation period, time-tagged electroluminescence photon counting provides previously inaccessible, background-free information about the field and injection dynamics within nanoscale break junctions.

To create electroluminescent junctions, we thermally evaporate 20nm-thick gold films on glass substrates. Substrates are transparent and thin enough to enable imaging with a 1.4NA (Numerical Aperture) oil-immersion objective mounted on an optical microscope. Two leads are attached to the gold surface and the entire assembly is placed under vacuum as described in chapter 2.[48] The sample holder and electrode assembly are encased with mu-metal to prevent radio frequency (RF)-interference with other instruments. Under DC bias, momentum transfer from electrons to the Au atoms results in void formation at some critical current density and temperature combination.[99] Film resistance rises dramatically as this void enlarges to break the film. Commonly known as electromigration, this phenomenon is often employed to produce very small break junctions in metal wires.[23] In the presence of a constant DC potential at or above some critical level (~2.5 V), the junction formation can be monitored by measuring increasing film impedance. The final junction impedance reaches $>10^6\Omega$ in a few seconds with a total charge consumption on the order of $1C/\mu m^2$. Since the fabrication process is carried out under constant polarity, the mechanical forces generated by the external field serve to structurally and chemically polarize the metal film. As a result, slight structural asymmetry is incorporated into the junction and is observable by both optical and

electrical measurements. The final junction is very heterogeneous with many sub-nanometer interelectrode gaps. Dramatic irreversible changes in film morphology after electromigration-induced breaking also allow monitoring of junction formation by observing film optical properties. This asymmetric change in the film refractive index, makes the junction easily discernible by phase contrast microscopy (Fig. 1b), suggesting the creation of a *hetero*junction as opposed to the homojunction behavior commonly assumed when utilizing such gold break junctions for molecular electronics studies.[23, 24, 32, 33, 35]

Spatially-resolved electron Energy Dispersive Spectroscopy (EDS) probes electrode chemical composition (Fig. 1a), revealing slightly higher oxygen content on the anode. During junction formation, gold undergoes an asymmetric combination of thermal and electrochemical oxidation consistent with our observed chemical composition. The final result is a disordered array of isolated gold nanodots created within the break junction in a gold-insulator-Au_n-insulator-gold configuration. Electrochemical and x-ray photoelectron spectroscopic studies[100, 101] of oxide formation on gold surfaces suggest that the atomic configuration of these oxide regions may be a mixture of insulating auric oxide (Au_2O_3) and gold hydroxide ($Au(OH)_3$) created from physisorbed water and hydroxyl moieties. These oxygen-rich insulating layers are analogous to the aluminum oxide tunneling barriers employed in conventional inelastic electron tunneling spectroscopy (IETS) measurements.[2] Large band-gap insulators such as Al_2O_3 are an indispensable element of these systems because they electrically isolate the leads from the analyte being studied. Separation of the gold nanodots from metallic electrodes enables charge transport through clusters while preserving their low density of states near

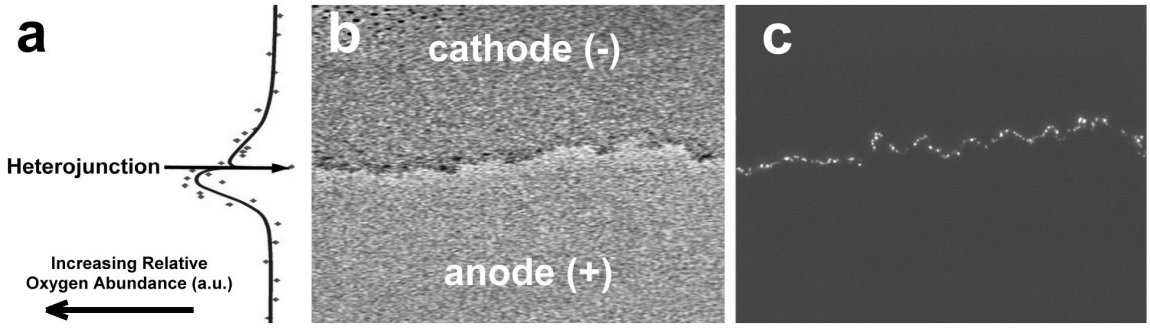

Figure 3.1. Characterization of electromigration-induced gold break junctions. (a) Energy dispersive spectroscopy (EDS) of a gold film after electromigration-induced junction formation showing relative oxygen content (horizontal axis) versus distance from the junction (vertical axis). Each point represents integration over a 1 μm square. The line through the data is not a fit and is provided for ease of viewing. (b) Optical phase contrast micrograph of a gold junction collected immediately after electromigration. (c) Electroluminescence image collected through a 1.4NA objective using a CCD (Micromax, Princeton Instruments). A ±2.5 VAC signal at 205 MHz was used as the electrical excitation.

the HOMO-LUMO gap. Without the insulating gap, the metallic electrodes' continuous density of states would broaden the molecule's discrete states precluding sharp tunneling resonances, charge separation, or observable electroluminescence.[16] As we now report, under continued electrical excitation, bright near IR electroluminescence is observed from gold clusters, providing a map of the junction (Fig. 1c) which is otherwise too narrow to characterize by optical methods. While only small, several-atom clusters with discrete states electroluminesce, typical electromigrated gold junctions are very heterogeneous and may contain much larger isolated grains.[38]

3.2 Electroluminescence from Individual Molecules in DC and AC Fields

For applied biases of more than 3 VDC, light emission is observed from individual gold nanoclusters, and electroluminescence intensity increases with increased current flow (Fig. 2a). Transport through room-temperature gold break junctions is monitored by observing the electroluminescence from individual several-atom gold clusters and overall current through the whole junction. Emitted light is either routed (see chapter 2) to a CCD camera for imaging or spatially filtered by fiber-coupling to an avalanche photodiode (APD). Electrical pulses from the APD are properly conditioned and counted by a Becker & Hickl photon counting module.[52, 102] As electrons pass through the insulating gap, they inelastically tunnel through both vibrational and vibronic levels of junction-bound gold molecules which act as temporary charge reservoirs. Initial hole injection (ionization) followed by electron injection results in recombination yielding electroluminescence.[48] Above ~10 VDC, gold nanodots within the junction are thermally or oxidatively destroyed. Consequently, the cavity conductance and

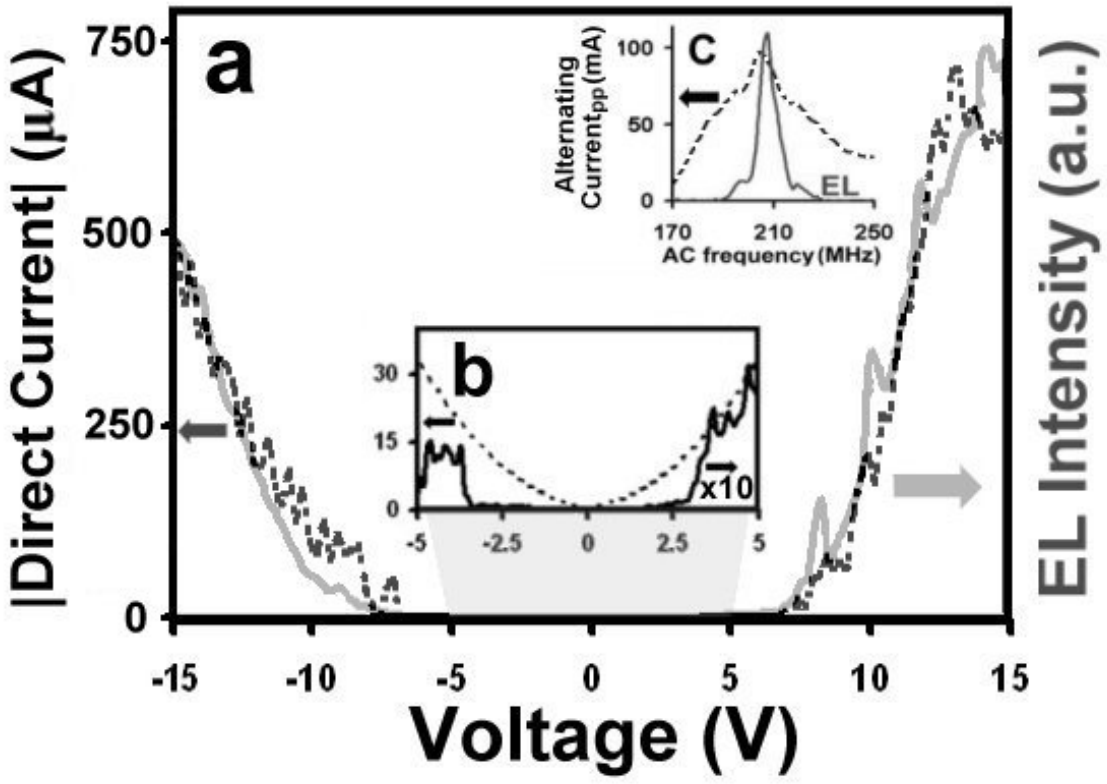

Figure 3.2. Time-averaged electrical (dotted traces) and optical (solid traces) response of a gold junction after electromigration. (a) Comparison of the electrical and optical response of the junction. The noise floor of the ammeter used here (Agilent E3646A) is approximately 100 μA and has been subtracted from the data. (b) Low voltage DC measurements of the junction current (dotted), using a Keithley 6485 picoammeter, and EL intensity (solid). (c) Frequency response of the total junction current (dotted) and EL (solid). AC current amplitude was measured using an RF transformer (Solar Electronics 9203-1) placed around the cathode.

electroluminescence irreversibly increase with voltage to produce the peaks observed in the current and emission intensity (Fig. 2a). The electrical and luminescent properties of the junction under low voltage DC excitation (Fig. 2b) are typically stable for a few hours of continuous operation, and EL has been observed at biases as low as +2.5VDC.

Similar gold electrodes fabricated using electromigration-induced break junction techniques[23, 36, 38] produce many interelectrode spacings measuring <10 nm. Purely electrical characterization of these systems is limited by inherent averaging over the entire cross-sectional area of the junction. Therefore, proper characterization of the electrodes in single molecular devices ultimately requires a single-molecule probe of the local electric field and electrode-molecule coupling, both before and after introducing the molecular bridge. Because light emission from gold nanoclusters is representative of the applied potential and the coupling to individual clusters, electroluminescence provides a local measurement of the electric field within the junction with higher sensitivity than possible with electrical measurements. Simultaneously measurable with current flow, nanoscale EL avoids contributions to the current from other conducting pathways and charge transport mechanisms, thereby providing corroborative and complementary information on local transport dynamics.

As electromigration is a destructive process, even the initially formed gold electrodes will further restructure under constant DC bias. Below a certain current level, DC electromigration-induced junction restructuring is minimal and the electrodes adopt a stable structure. Applying a larger DC bias across the electrodes restructures them further to a new morphology stable at the new voltage level. At 5 V bias, the total current through a typical ~100-μm junction (Fig. 3a) decreases steadily for the first 500 sec from

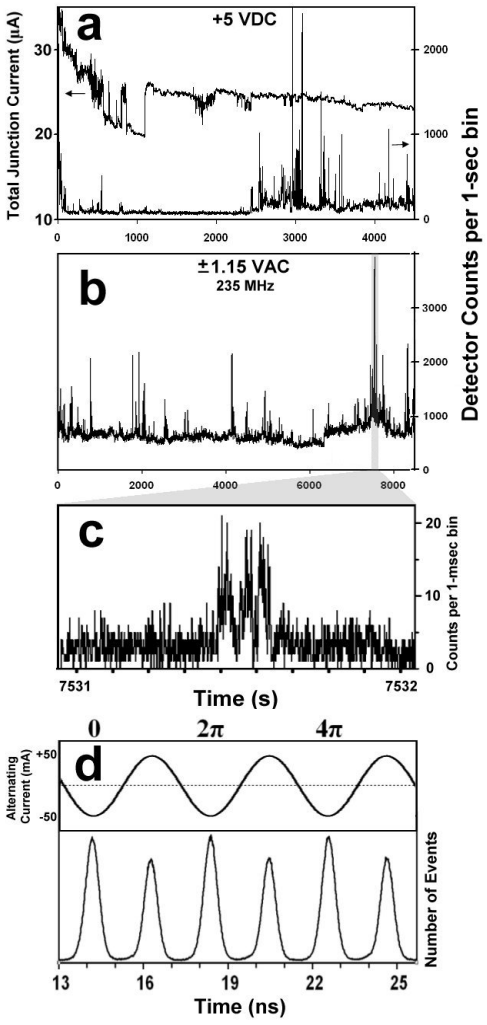

Figure 3.3. Time traces of electroluminescence intensity and total junction current under (a) DC and (b) AC bias. Electroluminescence was measured in the configuration shown in chapter 2. The dark count rate of our Perkin Elmer Avalanche Photodiode is approximately 100 Hz. DC current was measured using a Keithley 6485 picoammeter; AC current amplitude was measured using an RF transformer (Solar Electronics 9203-1) placed around the cathode. (a) 4500-sec series of total junction current measurements (300-ms bins) and EL intensity detected from an individual cluster under a constant +5 VDC field. (b) An 8500-sec time series of EL intensity detected from an individual gold cluster in ±1.15 VAC external field at 235 MHz. EL time series in a and b are binned by 1 sec. The sudden shift in EL intensity in b at ~6100 sec is an artifact of refocusing the image to correct for mechanical drift of the optics. (c) EL time series in b re-binned by 1 msec in the range 7531 sec to 7532 sec. (d) AC mode electroluminescence decay trace (histogram) collected by phase-locking to the excitation field. Three periods of the excitation are shown for all photons collected over the entire 8500-sec interval; the EL decay trace bin width is approximately 12 ps.

an initial value of 35 μA to 23 μA. A period of large, repeated current fluctuations follows from 500 sec to 1200 sec as the junction stabilizes. After 1200 sec at constant 5 V bias, the current fluctuations never rise above 2 μA suggesting that junction reorganization is minimal. After 1200 sec, the slow decrease in the current (<1μA over one hour) corresponds to the junction's gradual irreversible destruction brought about by heat and additional electromigration of the relatively high voltage DC field.

To minimize restructuring and stabilize emission, the junction-forming DC bias can be immediately switched off in favor of lower voltage, impedance-matched (AC) EL excitation. Matching the junction's natural resonance frequency produces strongly enhanced EL observed under high frequency AC excitation (Fig. 2c). At the junction resonance frequency (typically between 190 and 240 MHz), capacitive and inductive reactances exactly cancel, resulting in a true resistance of ~50 Ω for the circuit. This resonance exclusively results from the junction electrical properties (series RLC circuit), and correlates with electroluminescence due to increased charge flow. The resonant AC operating conditions produce strong EL and greatly increased stability at lower voltage than does the more thermally destructive DC excitation. At the junction resonance, AC current through the junction reaches ±50 mA (Fig. 3d) with peak-to-peak current fluctuations no greater than 100 μA for the duration of the experiment. Spatially resolved electroluminescent features result from individual gold nanocluster emission as evidenced by blinking, dipolar emission patterns, and antibunched EL.[48] Based on the jellium free-electron model and previous solution studies of gold nanodots,[82] Au nanocluster transition energies (~1.8 eV) scale with inverse cluster radius suggesting that these transition energies result from ~18-22 atom gold particles.[48]

3.3 Tracking Real-Time Transport Fluctuations

Typical DC mode electroluminescence (Fig. 3a) excited at +5V results in periods of intense light emission separated by long dark periods in which no EL photons are detected. In contrast, typical AC mode electroluminescence (Fig. 3b) rarely turns off for periods longer than 1 sec as demonstrated by the baseline EL count rate of approximately 600 Hz. Frequent bursts of electroluminescence intensity rise above this baseline to reach detected count rates as high as 4 KHz. The fast intensity fluctuations observed in figure 3b can be further resolved by 1-msec binning, and expansion of the 4-KHz spike at 7531 sec (Fig. 3c) reveals a series of much shorter bursts (< 10-msec duration) in rapid succession reaching more than 20 counts per 1-msec bin. It is interesting to note that while AC excitation is applied at lower voltage than is the DC field, resonant AC mode produces more photons per second and higher peak intensities during bursts. This discrepancy likely arises from clusters only needing to couple to one electrode for AC EL. Since charge must flow *through* the junction in DC excitation and *around* the junction in AC excitation, efficient DC EL requires weak, but significant nanocluster coupling to both electrodes while AC EL requires such coupling to only one. These coupling rules suggest that a given nanocluster is more likely to electroluminesce in an AC field than in a DC field of equivalent voltage. Because each AC-driven photon corresponds to hole and electron injection from the same electrode,[48] and injection from the electrodes is separated in time by the oscillating field polarity, all information about the anode- and cathode-nanocluster coupling dynamics contained in the AC EL time series is separable.

An on-board 20 MHz macrotiming clock (Becker & Hickl SPC-630) provides the timing resolution to build the chronological EL-photon arrival time series shown in figure 3a-c, with bin widths down to 50-ns. In all experiments, the APD counts routed to the Constant Fraction Discriminator (CFD) are further referenced to an external clock. In the case of DC mode electroluminescence, an external pulse generator starts the time-to-amplitude conversion in the photon counting module. Because such an external pulser is not synchronized with the EL excitation, no DC EL decay information is collected. However, modulation of the excitation field as in AC mode enables phase-locked synchronization of the CFD to the EL excitation, analogous to the synchronization of a fluorescence signal by a modulated laser in a frequency-domain lifetime measurement. AC mode EL photon arrival times are thus synchronized to the same AC excitation field that drives the electroluminescence, and it is possible to gather phase information from each EL photon. Electronically dividing the excitation clock frequency by an integer, N, (Pulse Research Lab, PRL-260NT) allows phase-locked detection of EL pumped above the 200-MHz synchronization limit of our Becker & Hickl SPC-630 time-to-amplitude converter while producing histograms spanning N complete excitation periods. Using this phase information, we can build a histogram of the EL decay profile (Fig. 3d). The histogram shows two EL peaks for every full period (2π) of the excitation sine wave. For the 235 MHz excitation field applied, the full 13 ns window shown here contains 6 peaks and three complete periods (6π). In each period, the first peak at 0 corresponds to EL resulting from charge injection through the anode and is more intense than the second peak appearing near π.[48] The smaller peak near π corresponds to gold nanodot EL resulting from cathode injection. Because the potential applied across the junction is an

oscillating field of alternating polarity, the electric field driving charge injection from the anode side is identical to that from the cathode side, but shifted in phase by π. The intensity difference between anode and cathode peaks is then a direct result of asymmetric coupling between the electroluminescent gold cluster and the electrodes used to inject charge. Any electrode chemical asymmetry (Fig. 1) only minimally affects the charge injection asymmetry. The original junction polarization resulting from electromigration likely plays the major role. As a compilation of all photons in the 8500 sec time series, the histogram (Fig. 3d) represents a time-averaged picture of the electroluminescent junction asymmetry revealing a slight preference for nanodot charge injection from the anode over that from the cathode. It is interesting to note the narrow linewidth of the peaks in the histogram as compared with the broader sinusoidal excitation field used to generate them. This narrowing is a direct result of the discrete nanocluster energy levels and inelastic electron tunneling into these states. As the same two-pulse polarity is observed for Au EL as that reported previously for Ag,[97] a hole must first tunnel from the injecting electrode into the bridging nanocluster's ground state and an electron must follow, one-half period later, tunneling into a discrete cluster excited state. Confirmed by extensive pulse-excitation data (in preparation), this process results in characteristic cluster turn-on voltages as evidenced by narrow EL excitation peaks. Consistent with previously reported EL lifetimes of ~400 ps and our 500-ps-limited detection, the peaks in the histogram appear largely symmetric with a small observable exponential component from the sub-ns cluster radiative decay.

3.4 Tracking Coupling Dynamics by Field Modulation

In both AC and DC mode operation, the applied electric field raises the chemical potential of one electrode with respect to the other as it drives the system away from equilibrium. These conditions give rise to time-dependent charge transport through the junction. Comparison of the relative peak heights in the EL decay histogram indicate that, for long times, the relative coupling strengths between cluster and electrode slightly favor anode injection. By synchronizing detection to the oscillator driving the AC mode EL, we ensure that the photon arrival times contain phase information corresponding to the excitation field. It is then possible to separate out the different electrode contributions to the chronological EL time series by analyzing (or post-acquisition gating) it in different phase ranges. The EL time series containing only photons within the range ($-\pi/2$, $\pi/2$) provides time-dependent information about the anode-cluster coupling strength.[48] Similarly, the EL time series of only photons within the range ($\pi/2$, $3\pi/2$) provides time-dependent information about the cathode-cluster coupling strength. Within any microtime histogram, the normalized difference of these two contributions to the EL time series is given by

$$A(t) = \frac{EL_{\left(-\frac{\pi}{2},\frac{\pi}{2}\right)}(t) - EL_{\left(\frac{\pi}{2},\frac{3\pi}{2}\right)}(t)}{EL_{\left(-\frac{\pi}{2},\frac{\pi}{2}\right)}(t) + EL_{\left(\frac{\pi}{2},\frac{3\pi}{2}\right)}(t)}$$

and represents the time-dependent charge injection anisotropy for a specified binning time. When $\boldsymbol{A}(t)>0$, charge transport through the cluster resulting in electroluminescence is dominated by injection from the anode. Times for which $\boldsymbol{A}(t)<0$ correspond to EL from

cathode injection. When $\boldsymbol{A}(t)=0$, the electroluminescent cluster is coupled equally to both electrodes.

A plot of the normalized gated intensity difference, $\boldsymbol{A}(t)$, is shown in red (Fig. 4a) alongside the total EL time series shown in black. As expected from the time-averaged EL decay histogram (Fig. 3d), junction transport shows an overall preference for anode injection with $\boldsymbol{A}(t)>0$ for most of the time series. The mean value of $\boldsymbol{A}$ for the entire 1-sec binned time series is +0.080 with minimum and maximum values of -0.48 and +0.71, respectively. It is interesting to note that large changes in the gated intensity difference occur in short bursts with similar duration as the bursts in EL intensity. In fact, side by side comparison of the intensity and gated intensity difference reveals a high degree of correlation. The coincidence of peaks in the two traces indicates that the electroluminescence bursts in the total intensity time series (Fig. 3b) are a direct result of large-amplitude, short-lived changes in the cluster electrode coupling strength. As mentioned above, the arithmetic sign of the bursts in the red trace indicates the electrode to which the coupling has increased. The time required to transition from equal coupling to either strong anode ($\boldsymbol{A}(t)>0$) or cathode ($\boldsymbol{A}(t)<0$) coupling is typically <10 ms. Times at which the gated intensity difference is low (slightly above 0) correspond to the weak constant "on" state with electroluminescence rate of ~600 Hz suggesting that, at these low Voltages, the cluster rarely couples strongly to both electrodes at once. An estimate of the junction's injection efficiency, obtained by correlating EL emission rate with excitation rate,[103] indicates injection rates of 22 MHz and 3.3 MHz for the "strong" and "weak" coupling regimes, respectively. Occurring on timescales much slower than the modulation frequency of the driving AC field, these large coupling rate fluctuations are

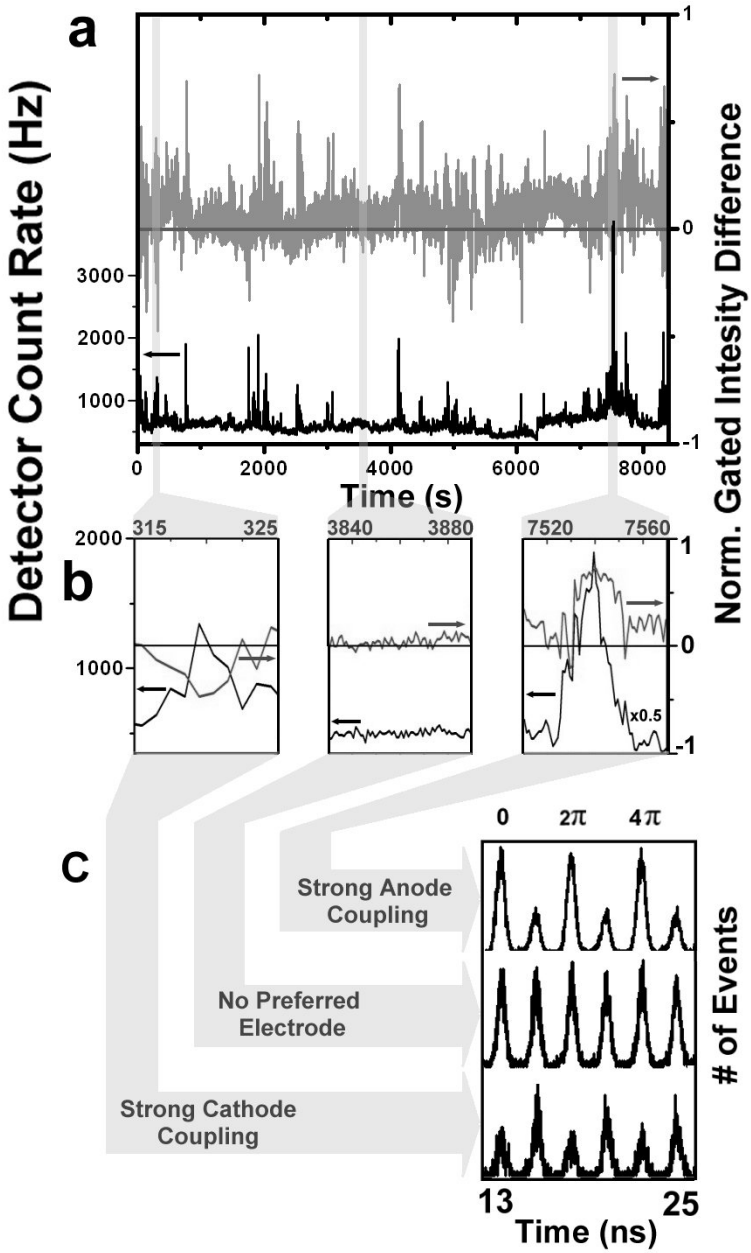

Figure 3.4. Normalized gated EL intensity difference (gray) along side the total AC mode EL intensity (black). (a) The full 8500-sec time series is expanded for ease of viewing (b) at three regions denoted by vertical gray bars. (c) EL decay traces corresponding to each expanded region of the time series showing three distinct electrode coupling regimes. Three periods of the excitation are shown.

likely also present under DC fields. The coupling fluctuations are still fast enough to be obscured by time-averaged DC transport measurements and may give rise to large variances in perceived junction DC conductance. The time-dependence of transport tracked by nanoscale EL illustrates the importance and need of additional dynamics studies in molecular electronics.

The observed cluster emission dynamics indicate three distinct coupling regimes which result in AC electroluminescence, namely strong anode coupling, strong cathode coupling, and weak coupling to both. An example of each coupling regime is presented (Fig. 4b) by expanding portions of the full time series, denoted by vertical gray bars (Fig. 4a). From left to right, the panels illustrate strong cathode coupling ($\boldsymbol{A}(t)<0$, grey) with strong emission (black), no electrode preference ($\boldsymbol{A}(t)\sim0$) with weak emission, and strong anode coupling ($\boldsymbol{A}(t)>0$) with strong emission. EL decay histograms containing only the photons in each expanded region are shown (Fig. 4c) for comparison with the full time series histogram (Fig. 3d). The relative anode (2π) and cathode (π) peak heights are quite different for the strong coupling cases while the middle histogram corresponding to the weak coupling regime shows identical peaks spaced by π.

The obscuring effect of averaging in nanoscale transport is also evident in the cluster injection anisotropy distributions. EL from a total of 103 nanoclusters was measured in the same way as above, but for shorter overall times. A histogram of the 90-sec-binned $\boldsymbol{A}$ for the ensemble (Fig. 5a) has a mean value of +0.030 with a minimum of -0.29 and a maximum of +0.87, matching closely the dynamic range exhibited by the cluster in figure 4. Histograms of the 1-sec-binned $\boldsymbol{A}$ for this cluster (Fig. 5c) and three other arbitrarily chosen clusters (Fig. 5d-f), each observed for several hours as in Fig. 3,

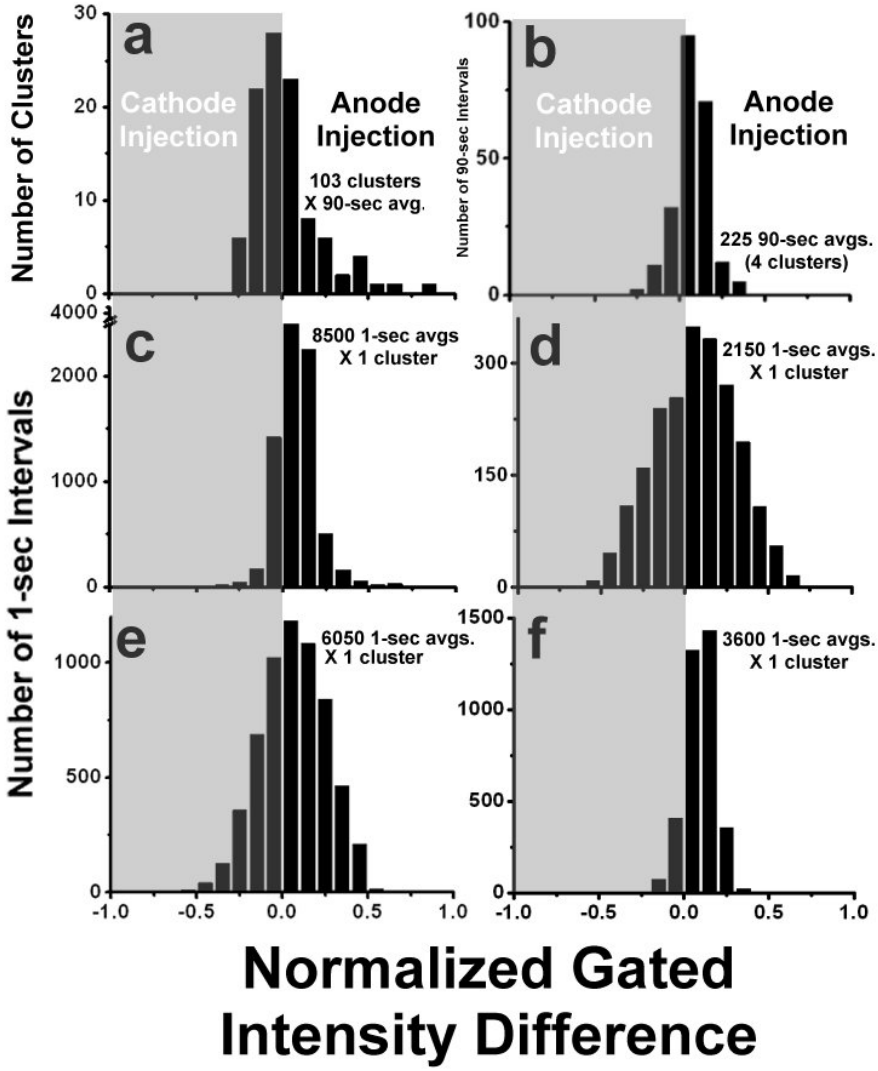

Figure 3.5. Histograms of the normalized gated intensity difference, ***A***(t), for 103 gold nanoclusters. (a) The 90-sec averaged ***A***(t) value for 103 individual clusters is provided for comparison with (b) the 90-sec averaged ***A***(t) value sampled 225 times from the four gold nanoclusters summarized individually in c through f, each with 1-sec binning.

are shown for comparison. While the maxima, minima, and widths of each cluster anisotropy distribution vary, all histograms are asymmetric with a positive mean showing anode preference. Addition of the individual cluster histograms (c-f) and re-binning at 90-sec results in a distribution of $\boldsymbol{A}$ sampled 225 times from 4 clusters (Fig. 5b). For very high values of $\boldsymbol{A}$, the tail in the ~ensemble-averaged distribution (Fig. 5a) is not yet observed in the sub-ensemble time-averaged distribution (Fig. 5b). This may be due to a combination of our limited observation times (a few hours per cluster) compared with our relatively large ensembles, and the greater environmental sampling inherent in averaging over many clusters between heterogeneous electrodes. Moreover, while the $\boldsymbol{A}$ value for transport through an individual cluster may vary dramatically yielding a broad distribution (Fig. 5d-e), the distribution variance is significantly diminished when integrating for long times, as in (b), or over many transport pathways, as in (a). The qualitative similarities in anode preference and variance between the cluster-averaged $\boldsymbol{A}$ distribution (a) and the time-averaged $\boldsymbol{A}$ distribution (b) suggest that the system is approximately ergodic.

The mechanism by which electrode-nanocluster coupling may change remains unknown, and could involve dynamic changes in the molecule's orientation or position relative to the charge injecting electrode as well as small electromigration-induced electrode morphology changes. The three coupling regimes detailing the dynamics of typical, resonance-AC-excited electroluminescent clusters are sufficient for describing 100 of the 103 molecules for the duration of our experiments. In the remaining three molecules studied, however, EL arising from additional charge transport mechanisms is observed. These three molecules further demonstrate the inherent heterogeneity of the

break junction environment. The EL decay histograms of these clusters (Fig. 6, right) show additional light-emission peaks (shaded) phase-shifted from those appearing at π and 2π. This type of emission yields much narrower lineshapes than typical EL, and may result from small DC offsets in the local potential due to electrostatic charging of islands near the nanocluster. The narrow lineshapes and negative phase-shifts observed are consistent with transient, local charging on large scales. Static floating of a sinusoidal potential by even a few percent can cause an observable delay in the time at which the discrete cluster turn-on voltage is reached. The left panels in figure 6 illustrate how such an offset polarity and magnitude could translate into a phase-shift, φ, in detection. In all the examples (Fig. 6, left), only portions of the sinusoidal potential exceeding the discrete cluster turn-on voltage (shading) may drive cathode- or anode-injection and EL. In the absence of charging (top panel), hole and electron injection proceed from the same electrode as the applied potential crosses the cluster turn-on voltage precisely at 0 or π. These conditions generate a "typical" EL decay trace with alternating anode and cathode peaks at 0 and π, respectively.

The proposed electrostatic charging of a nearby grain may perturb the local junction potential near an electroluminescent cluster by temporarily inducing a DC offset. Consistent with previous experiments, assuming that only the electron injection step occurs into a discrete energy level, negative offsets (middle panel) would result in earlier cluster turn-on from the anode producing an additional EL peak detected slightly before the normal anode-injection EL peak (2π). Because negative offsets drive electron injection exclusively from the anode, any EL driven by a negative-offset field should be detected in the range (π, 2π). Conversely, positive offsets (bottom panel) might drive

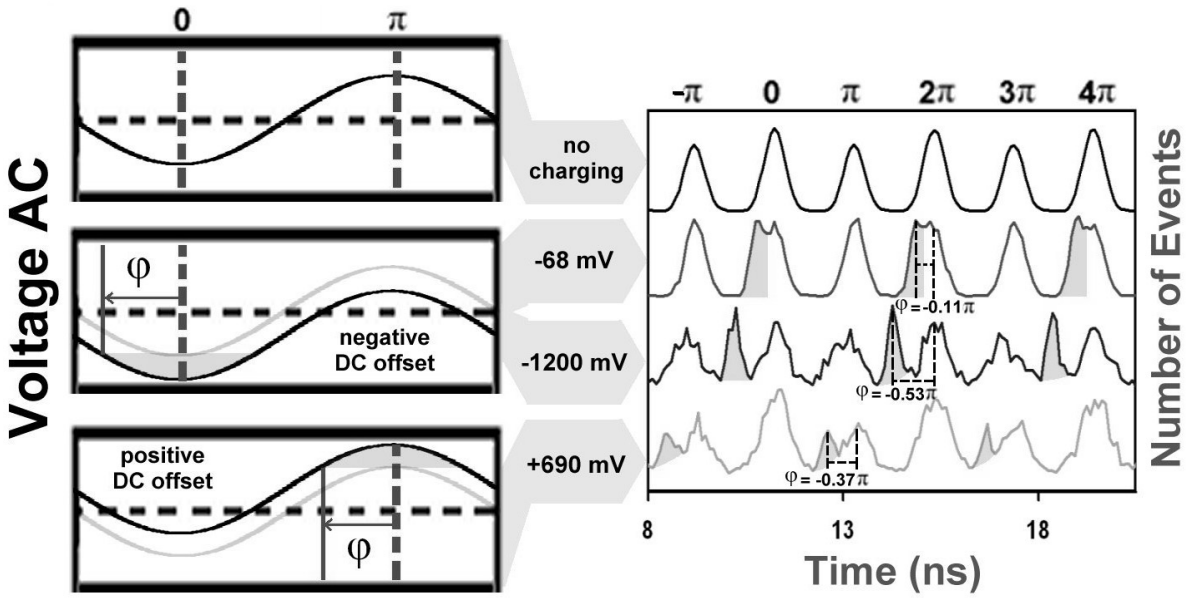

Figure 3.6. Time-dependent voltage diagram and EL histograms. (top) Typical cluster emission under AC excitation is shown for comparison with cluster emission in the proposed presence of (middle) negative and (bottom) positive electrostatic charging of the injecting electrode. EL histogram bin width is approximately 97 ps.

electron injection from the opposite polarity cathode producing EL in the range (0, π). Following this model, observed peak phase-shifts away from their expected anode- or cathode-injection emission phases (times) of -0.11π, -0.53π, and -0.37π would correspond to DC offsets in the local potential of -68 mV, -1200 mV, and +690 mV, respectively. The observed emission switches back and forth between phase-shifted and non-phase-shifted EL suggesting that the charging effect is not constant. Such transient charging of isolated grains could likely be modulated by electromigration and is consistent with the slow but dynamic electrode restructuring and dynamic coupling to individual nanoclusters observed in DC and AC experiments. In contrast to alternating anode- and cathode-injection peaks found in typical emission, the proposed additional charging-induced peaks appear only once per excitation period. This is presumably because the charging must be stable for at least several seconds, and raising the potential for injection from one electrode requires an equal lowering of the potential for injection from the opposite electrode one-half period later.

In summary, we have observed dynamic electrode-molecule couplings in electroluminescent gold break junctions. Phase-locking the AC mode excitation and detection allows a phase-gated analysis of the photon stream and separation of the individual electrode contributions to charge transport in the absence and presence of static charging. These electroluminescent, molecular gold clusters within electromigrated gold break junctions are created *in situ* during the asymmetric writing process and act as nanoscale reporters of the electric field spanning the junction. The fluctuations in charge injection asymmetry are biased toward the anode which is defined as the positive electrode during junction formation. This asymmetry is likely a general feature common

to electromigrated gold break junctions arising from an inherently asymmetric fabrication process, and it is consistent with recently reported asymmetric Kondo resonances[36] and Coulomb blockade.[38] The optoelectronic properties of these systems arise from a combination of the electrical properties of the gold-insulator-gold junction with the optical properties of the isolated nanoclusters within the junction. Therefore, even at room-temperature, the observable cluster emission reveals previously inaccessible information about the rich physics governing tunneling across the electromigrated gold break junctions so commonly employed in molecular electronics.

IV. EXCITATION SPECTROSCOPY OF ELECTROLUMINESCENT GOLD NANODOTS

Single molecule spectroscopy's ability to elucidate local environmental and nanoscale dynamics has facilitated its evolution into a remarkably successful tool for the study of physical, chemical, and biological processes[53, 54, 104-106]. Measurements of single molecule fluorescence intensity[54, 104] and lifetime[65] fluctuations, spectral[55, 104, 107] and orientational[57, 108-111] diffusion, as well as molecular-scale charge transport[18, 22, 36, 37] and quantized nanoparticle charging[32, 38, 89] routinely provide insight into sub-ensemble phenomena otherwise lost to bulk averaging. Complementary to the last two observables, single molecule electroluminescence has recently emerged as an optical probe of quantized charge transport dynamics across nanoscale tunneling gaps.[39, 40, 48, 49, 97] Even at room temperature, quantum confined free electron metals such as several-atom copper,[40] silver,[39, 40, 84, 97] and gold[39, 48, 82, 112, 113] nanoclusters behave as multi-electron artificial atoms with deep confinement potentials and strongly electroluminescent transitions between discrete energy levels. An optical observable directly correlated to inelastic electron tunneling, single molecule electroluminescence (EL) provides a much cleaner readout of local transport with increased sensitivity over inherently heterogeneous electrical measurements that may encompass multiple parallel current pathways, as even nanoscale electrodes are orders of magnitude larger than the molecular conductor.

Electroluminescence from individual gold nanoclusters ($Au_{\sim 18\text{-}22}$) produced within electromigration-induced nanoscale junctions has been successfully employed as a probe of electrode-molecule coupling and nanoscale charge transport.[49] However, the complex

geometric and electronic structure of these "molecular metals" is not well-characterized and has been addressed in only a few theoretical studies.[114-119] Inelastic tunneling spectroscopy of surface adsorbates was first carried out at cryogenic temperatures by Lambe and coworkers.[76, 77] Ensemble averaged measurements of the tunneling current through an analyte-doped insulator revealed inelastic coupling to dopant vibrational[2, 76, 81] and electronic transitions[77, 78] with increased differential conductance and spectrally broad light emission at characteristic potentials. Above cryogenic temperatures, these molecular signatures are obscured by thermal broadening and excited state coupling to non-radiative decay pathways. While we have shown that gold nanoclusters readily electroluminesce at room temperature[48], other sources of heterogeneity limit bulk characterization of cluster electronic structure. For example, small variations in the local electrode geometry surrounding individual nanoclusters and local electrode-molecule coupling rates that may change independently over time both contribute to an averaged ensemble measurement, possibly even when individual emitters are spatially resolved.

To create arrays of electroluminescent gold nanoclusters, thin gold films are first evaporated onto glass coverslips and electrodes are attached. The film is then placed under vacuum (~1 μTorr) and broken by computer-controlled electromigration to form a nanoscale junction, as described in chapter 2.[48, 49] Electrode-coupled gold nanoclusters are inherently created within the nanoscale junction during the breaking process and readily produce field-dependent electroluminescence as previously demonstrated in both DC and AC external fields.[39, 48, 49] Gold nanocluster electroluminescence is collected (see chapter 2) from below through the glass coverslip substrate using an inverted optical microscope with a 1.4 NA (numerical aperture) objective. The emission may be imaged

on a CCD or detected by a fiber-coupled avalanche photodiode (APD). The APD output is sent to the constant fraction discriminator of our single photon counting module (Becker & Hickl SPC630) which is synchronized to an external 50-MHz clock which also triggers the electrical excitation. Detected photons are time-tagged and a histogram of their arrival times relative to the synchronization clock is generated. To measure the RF current in our tunnel junction circuits, a current probe (Solar Electronics) is placed around the cathode which acts as the single-turn primary coil of an RF transformer. The induced voltage across the secondary coil is monitored by an externally triggered digitizing oscilloscope. This signal is recorded and numerically integrated to obtain the RF current. Triggering oscilloscope measurements of the excitation voltage and junction current with the same clock used to synchronize photon detection permits comparison of voltage, current, and electroluminescence on the same time axis. In this manuscript, we demonstrate gold nanocluster electroluminescence driven by electrical pulse sequences as a method for exploiting electrode-molecule coupling asymmetries to tune the relative charge injection from one electrode versus the other. Control over which electrode is responsible for hole- and electron-injection over a broad spectral range enables careful interrogation of cluster excited states as reported by their electroluminescence from discrete electronic levels.

4.1 Controlling Charge Injection in Time and Energy

In order to tune the relative electron injection from the anode and cathode, we drive the EL using a train of opposite-polarity electrical pulse-pairs (Fig. 4.1) separated in time by intervals of zero bias. The time dependent excitation voltage, V(t), and total

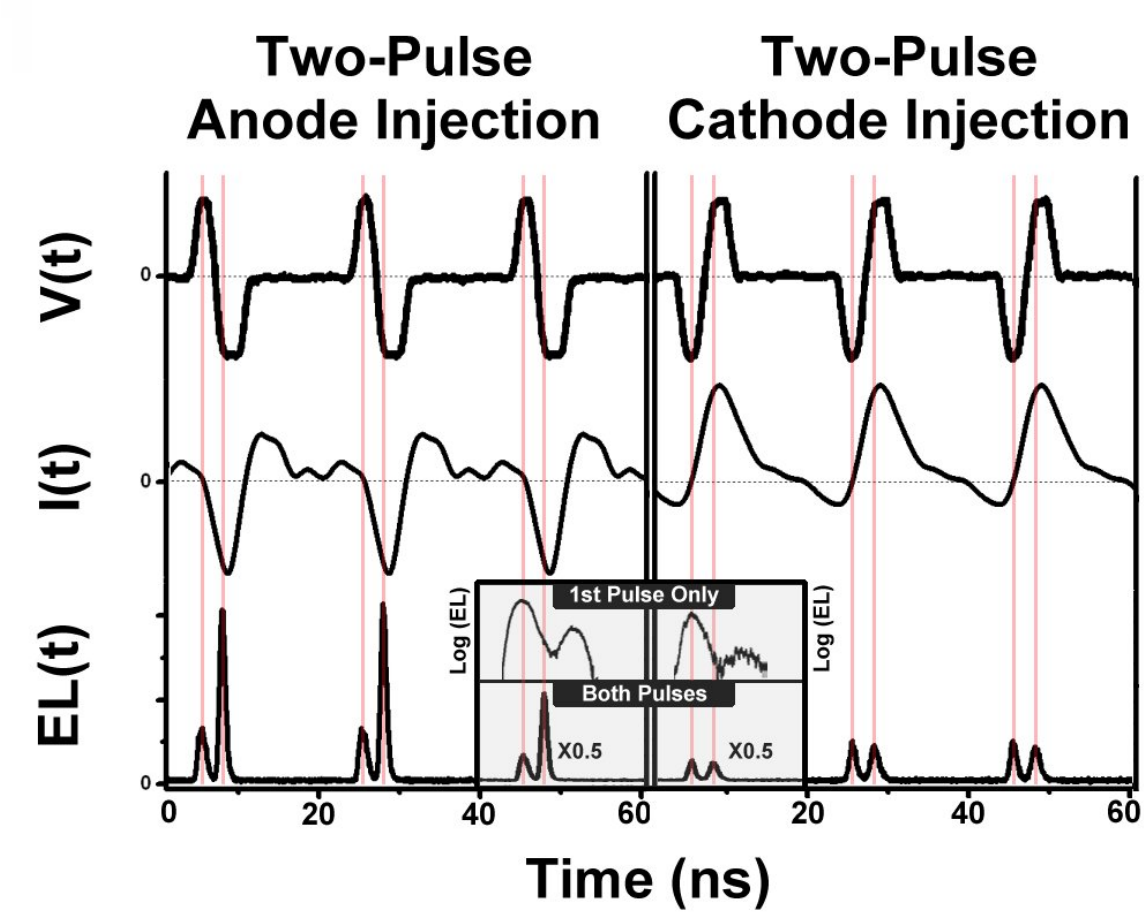

Figure 4.1. Typical excitation voltage (V), total junction current (I), and electroluminescence (EL) time characteristics from an individual gold nanodot for two pulse sequences of opposite polarity. A positive-negative pulse polarity sequence with resulting current and EL characteristics (left panel) is shown for comparison with characteristics produced by a negative-positive pulse polarity sequence (right panel). The external timing clock frequency was electronically divided prior to synchronization of the SPC-630 counting module producing three excitation periods of 20 ns each. The maximum and minimum excitation voltage in both cases is ±1.4 V. (Inset) Time histograms of one-pulse excited electroluminescence intensity are plotted on a log scale.

junction current, I(t), are plotted for two excitation sequences. Both sequences are composed of an initial 2-ns pulse (FWHM) followed, ~2.5 ns later, by a 3-ns pulse, and each pulse pair is separated from the next by 20 ns. Synthesis of the pulse-pair excitation field begins with two individual channels of a function generator set to emit electrical pulses at 50 MHz. The polarity, duration, and amplitude of pulses from each channel can be tuned independently and an interpulse delay of ~2.5 ns is set before both signals are sent through a 3-GHz signal combiner (Minicircuits) and on to the tunnel junction. The interpulse delay is set to match the junction electrical resonance which varies slightly from sample to sample. Varying the pulse widths from 2 ns to 3 ns (FWHM) and the amplitudes from 0.3 V to 3.0 V (into 50 Ω) results in a library of excitation sequences comprised of pulse-pairs separated in time by 20 ns with a ~15-ns zero bias interval from the end of one pulse-pair to the beginning of the next. Monitoring the electroluminescence intensity from individual gold nanoclusters as one or more of these excitation parameters is scanned can provide molecule-specific information about time-scales and energies involved in electrode-cluster transport.

The two voltage traces in figure 1 differ only in polarity such that one is the mirror image of the other about 0 V, but equal in amplitude at all times. In each case, the measured total current flow around the junction shows much slower rise and fall times than do their corresponding voltage traces. This smoothing effect can be understood in terms of the junction transmission spectrum. Under external AC excitation, electromigration-induced nanoscale break junctions behave as effective series RLC circuits with a narrow transmission window in the MHz regime.[48] Gold junctions (typical peak transmission ~220 MHz) act as band-pass filters attenuating all of the electrical

frequency components outside the transmission window. The current traces in figure 1 reveal the junction's inability to respond to signal frequency components higher than ~300 MHz. In addition, unlike their corresponding voltage traces, the left and right current traces are not equal in amplitude at all times. The left current trace shows an additional peak, not present in the right trace, 4.5 ns after each pulse-pair, indicating an asymmetry in the junction transport properties. The observed asymmetry in current is consistent with previously reported structural, chemical, and electrode-molecule coupling asymmetries in electromigrated gold break junctions,[48, 49] and likely arises from enhanced harmonic ringing of the junction at its characteristic resonance frequency of ~220 MHz when excited by a positive-negative pulse polarity sequence.

Excitation of gold nanocluster electroluminescence in an AC electric field proceeds via two-step sequential hole- and electron-injection to the cluster energy levels from the same electrode via the positive and negative portions of the AC signal. Analogously, in two-pulse experiments, positive polarity at the coupling electrode drives hole-injection into the cluster. Reversing the field polarity with a second (negative) pulse drives electron-injection from the same electrode into a nanocluster excited state. Radiative decay of the resulting cluster charge separation occurs on the sub-ns scale and is readily observed as highly polarized, antibunched electroluminescence.[48] In pulsed excitation mode, each pulse-pair emulates one full period of an AC field where the first and second pulses provide the hole- and electron-injection driving fields, respectively. The pulse-pair polarity sequence determines which electrode will act as the dominant charge-injecting electrode. A positive-negative pulse polarity sequence into the anode (Fig. 4.1, left) drives hole-injection and, subsequently, electron-injection into the

nanoclusters from the anode. While this sequence can also drive electron-injection followed by hole-injection from the cathode, this charge carrier injection order would not result in cluster charge separation or EL.[97] A positive-negative pulse sequence, therefore results in electroluminescence almost exclusively driven by anode injection (as defined through the initial asymmetric DC electromigration process to form the electrodes). Conversely, the opposite polarity sequence injected into the anode (negative-positive) should produce EL driven mostly by cathode injection, at which the pulses appear positive-negative to the cathode-coupled nanocluster.

Electroluminescence intensity vs. time histograms from many excitation cycles of an individual gold nanocluster are shown for comparison below their corresponding RF voltage and current traces (Fig. 4.1). A ±1.4 V positive-negative polarity sequence (Fig. 4.1, left) applied at the anode produces two intensity peaks per excitation period in the histogram with an inter-peak delay of approximately 2.5 ns. The second peak has a slightly narrower linewidth than the first and nearly four times its intensity. A negative-positive polarity sequence (Fig. 4.1, right), also applied at the anode, drives charge separation via cathode injection and yields the same two-peak EL from the same cluster but with different peak intensities. The peaks produced by the negative-positive sequence are of similar intensity and match closely the intensity of the first peak in the positive-negative case. Taken together, the EL traces from both pulse polarity sequences illustrate preferential charge injection from the anode, common to electromigration-induced nanocluster arrays. Generation of the first peak in each pair requires only the first pulse in the excitation sequence (Fig. 4.1 inset) to establish weak, but sufficient, coupling to both electrodes simultaneously. Similar to the mechanism of DC-driven electroluminescence,

a single electrical pulse (of either polarity) may simultaneously drive hole-injection from one electrode and electron-injection from the other. EL is produced by one excitation pulse only when the excitation pulse amplitude becomes large enough to compensate for the cluster-electrode coupling asymmetry and drive both carrier-injection processes. Because both electrodes must couple to the light emitting cluster simultaneously, an equal rate of electroluminescence is expected from positive and negative pulses, consistent with the observation of similar first-peak intensities. Plotting the one-pulse EL intensity on a log scale reveals an additional weak peak nearly 6 ns after the first, likely due to harmonic ringing of the junction.

Unlike the first-peak intensities, the intensity of the second EL peak in each two-pulse excitation period is largely dependent on the polarity sequence used. A positive-negative sequence (Fig. 4.1 left) produces nearly three times more photons as a negative-positive sequence (right) applied to the same nanocluster, indicating that the dominant mechanism for the creation of this EL requires a change in polarity and, therefore, both pulses in the sequence. This mechanism of light production is similar to the mechanism of AC-driven EL[39, 40, 48, 49] and thus requires weak, but sufficient, coupling to only one electrode. In this mechanism, the coupling electrode (anode or cathode) becomes the dominant charge injecting electrode from which both hole- and electron-injection occur sequentially (not simultaneously). The relative intensity of electroluminescence produced as the second peak in the EL histograms is directly determined by the relative cluster coupling to the dominant charge injecting electrode. The second-peak intensity produced by cathode injection (right) is similar to that of the first peak in both cases. This is not surprising since the rate of first-peak electroluminescence produced by the two-electrode

(DC) mechanism is limited by injection from the weaker coupled electrode (cathode coupling). It is interesting to note that the first and second peaks in both EL decay traces are well separated in time, suggesting that nearly all carrier injection (hole *and* electron) occurs above some threshold voltage (not throughout their duration), and that the excited state lifetime is shorter than the interpulse separation. To further investigate the injection time-scales and energies required for gold nanocluster electroluminescence, several excitation parameters were optimized.

To optimize the charge injection timing for maximum electroluminescence generation, the widths of each pulse in the excitation sequence were scanned independently from 2.0 ns to 3.0 ns while holding the pulse amplitudes constant at ±1.8 V. In particular, the effects of pulse width on the time dependence of electroluminescence generation were explored. One full period of the time-correlated voltage, total junction RF current, and typical normalized electroluminescence from an individual gold cluster is shown (Fig. 4.2A) for each of 4 distinct anode injection excitation sequences (two short pulses, two long pulses, long pulse followed by short pulse, and short pulse followed by long pulse). Comparison of EL traces with their corresponding voltage and current illustrates the contrast between the slow total junction current response versus the faster driving voltage modulation and EL response. The four electroluminescence histograms presented show small relative offsets in their turn-on and peak intensity times. By synchronizing all of the voltage, current probe, and photon arrival time measurements to the same external clock, our setup ensures accurate determination of the relative electroluminescence onset times. Inspection of the turn-on order and relative offsets for the four excitation sequences shown (Fig. 4.2A) closely matches observed time offsets in

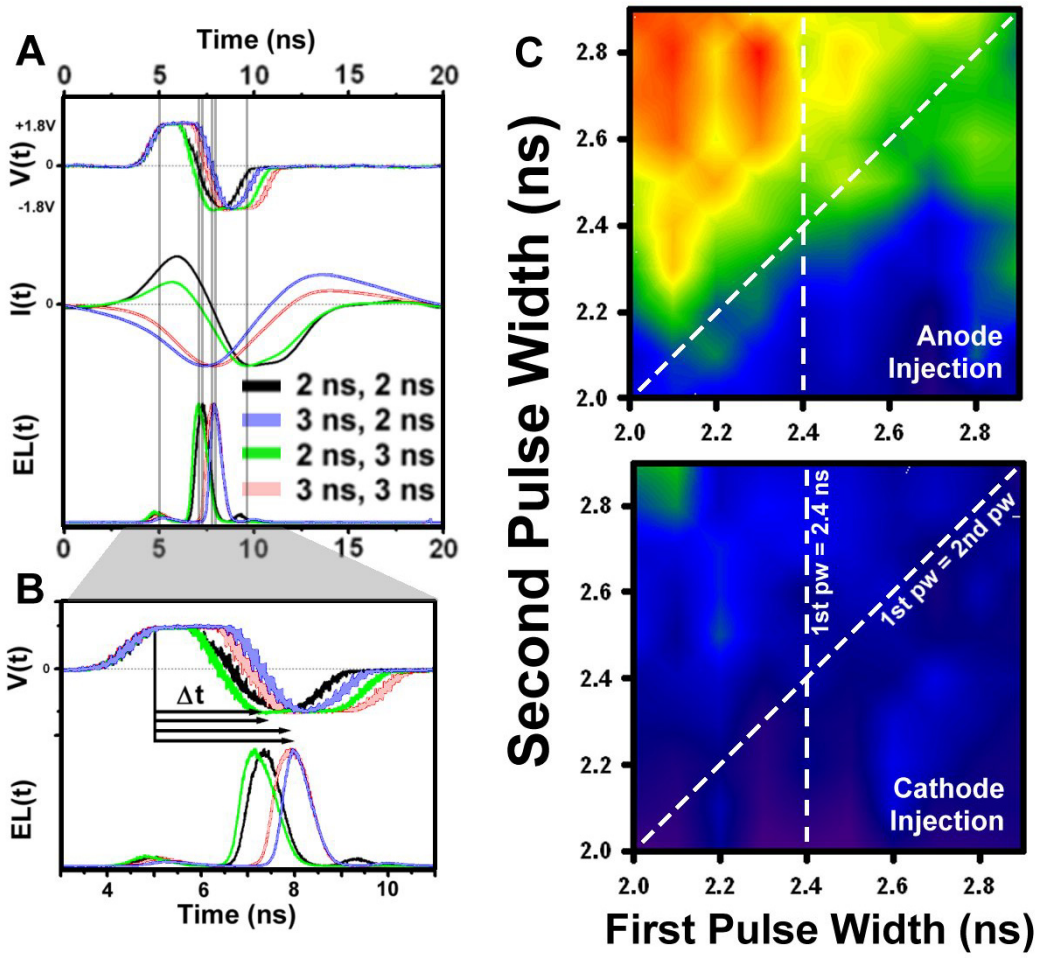

Figure 4.2. Pulse-width dependence of electroluminescence (A) timing and (B) intensity. (A) Four different excitation sequences of varying pulse widths produce a time-dependent total junction current and normalized electroluminescence. All four EL traces were collected from the same individual gold nanodot. One 20-ns period of the excitation is shown. (B) The contour plots summarize relative EL intensities from a total of 38 gold nanoclusters driven by several pulse-width combinations, and the upper and lower plots represent the EL driven by positive-negative and negative-positive pulse polarity sequences, respectively. Both pulse widths were scanned from 2.0 to 2.9 ns with a resolution of 0.1 ns (FWHM). The vertical and diagonal dashed lines indicate special ranges of pulse-width combinations (see text).

the RF voltage measurements. Expansion of the plots in figure 4.2B allows a closer look at the EL-peak offsets. In all sequences, the small initial EL peak near 10 ns coincides with the beginning of the initial +1.8 V excitation pulse. The maxima of the dominant second EL peaks, driven by one-electrode sequential injection, fall between 7 ns and 8 ns and are offset in time relative to each other. The positions of these EL-peak maxima are independent of pulse amplitude and line up remarkably well to the maximum voltage onset of the corresponding excitation pulse. As expected, the EL peak widths increase with excitation pulse width. Small variations in EL peak width result in a cluster-specific EL turn-on time sequence which is determined by the particular turn-on voltage of the cluster excited state being interrogated. Matching the EL offsets to time differences in the voltage sequence series (Fig. 4.2B) reveals a threshold of approximately -1.5 V for electron-injection and resulting electroluminescence.

Two contour plots (Fig. 4.2C) summarize the total anode- and cathode-driven EL intensity from 38 gold nanoclusters within a typical nanoscale junction as a function of applied first- and second-pulse width combination. The results for the positive-negative sequence (anode injection) are displayed in the top panel while EL driven by the negative-positive sequence (cathode injection) is shown in the bottom panel. For nearly all first and second pulse width combinations, the positive-negative sequence is clearly more efficient than the negative-positive sequence in EL generation. Again, this is a direct manifestation of preferential charge injection from the anode resulting from the asymmetric electromigration junction creation process. Both the anode and cathode injection sequences show strongest EL for small first-pulse widths (~2.1 ns) and larger second-pulse widths (~2.8 ns). The anode-driven electroluminescence intensity (Fig.

4.2C, top) decreases as the first-pulse width is *increased* above 2.4 ns, and it drops more gradually as the second-pulse width is *decreased*. This may indicate that the HOMO is more strongly coupled to the electrode and its density of states than is the LUMO. Cathode-driven EL (Fig. 2C, bottom) shows the same qualitative trends, but the intensity is muted by relatively low cluster coupling to the cathode. Extracting mechanistic information from these qualitative trends is not straightforward, however, because (as in the case of AC-driven EL)[48] the observed electroluminescence may reflect the nanocluster response convoluted with the junction response. Therefore, prior to discussion of charge carrier dynamics in the clusters, it is necessary to ascertain the degree to which junction transmission modulates EL generation.

Previously reported time-correlated gold nanocluster electroluminescence driven by RF AC excitation was shown to be phase-locked to its driving field[49]. The driving frequency corresponding to maximum EL generation (~200 MHz AC) is typically within a few MHz of the maximum total junction current transmission frequency. In contrast, the results of the width tuning studies in pulse excitation mode summarized by the contour plots (Fig. 4.2C) do not mirror the junction transmission frequency response. Moreover, agreement of the EL turn-on order with negative-pulse onset for each sequence (Fig. 4.2B) suggests that EL response times are not subject to direct screening by the junction transmission window. Despite the narrowing effect of the -1.5 V turn-on threshold on the EL decay histograms, the junction response (manifested as RF current) is too slow to account for the much faster observed electroluminescence response (see Fig. 4.2A). Both AC- and pulse-driven EL show strong correlation between the field modulation frequency and modulation of light emission, but only AC EL exhibits

emission peaks coinciding with the junction RF current maximum. The apparent dependence of AC-driven EL on junction transmission is merely the result of a phenomenon unique to sinusoidal excitation functions. Namely, the frequency of the total RF current is always equal to that of the RF Voltage. This is not the case in two-pulse excitation since there exist multiple frequency components and each is attenuated differently by the junction transmission profile. It is important to note that both excitation modes drive sequential one-electrode injection, but only two-pulse excitation provides the choice of dominant injecting electrode (by specification of the pulse polarity sequence) tempered by the lower efficiency single pulse injection and relative nanocluster-electrode coupling strength. Driving EL via anode (cathode) injection minimizes the cathode's (anode's) contribution to EL generation and therefore circumvents any artifacts of junction transmission. These results suggest that two-pulse driven EL (Fig. 4.2A, B, C) represents the nanocluster's response to the driving field with only minor contribution from the junction response.

Consequently, the observed decrease in anode-driven EL intensity for first-pulse widths longer than 2.4 ns (Fig. 4.2C, top) suggests that electrode-HOMO coupling is strong enough to accommodate short pulses, but longer 1^{st} pulses cut into the 2^{nd} pulse width, thereby decreasing EL intensity. This may be interpreted in terms of hole-injection timescales. Because holes must reside in the nanocluster until the second (electron-injection) pulse to result in EL, the 2.4-ns threshold likely represents the average hole injection time. Similarly, the observed increase of electroluminescence intensity with increased second-pulse duration contains information about electron-injection timescales. Under bias, the electrode-nanocluster coupling strength determines the effective rate of

electron injection into an emissive state. For injection and EL to occur, the coupling rate (~10 MHz) should be substantially lower than the cluster's inverse decay rate (~2.5 GHz). In this regime, increasing the duration of the electron-driving pulse from 2 ns to 3 ns greatly increases the chances for excited state injection and EL generation (Fig. 4.2C, top).

Because the electrode-molecule coupling strengths are dynamic and favor the anode, further study of cluster-specific turn-on voltages requires long integration times for EL detection and a separation of anode and cathode driven EL. Though separated in time by a few nanoseconds, anode- and cathode-driven EL are both present in AC EL making separation of the electrode contributions very tedious. By driving charge injection almost exclusively from one electrode, two-pulse excitation overcomes electrode separability problems. In addition, faster rise and fall times of pulsed excitation over AC mode afford higher control over the energy distribution of injected electrons.

To study the voltage dependence of anode-driven electroluminescence, first- and second-pulse amplitudes were varied independently from 0.3 V to 3.0 V while fixing the first- and second-pulse widths at 2.1 ns and 2.8 ns, respectively. Voltage, current, and EL traces from four different excitation sequences (two small amplitude pulses, two large amplitude pulses, small amplitude pulse followed by large amplitude pulse, large amplitude pulse followed by small amplitude pulse) are shown for comparison (Fig. 4.3A). In all cases, the voltage traces reach their respective maxima and minima at precisely the same time relative to the external trigger (see chapter 2). These normalized EL traces clearly differ from the width-scanned traces of figure 4.2. Fixing the excitation pulse widths results in the elimination of the EL peak offsets such that all excitation

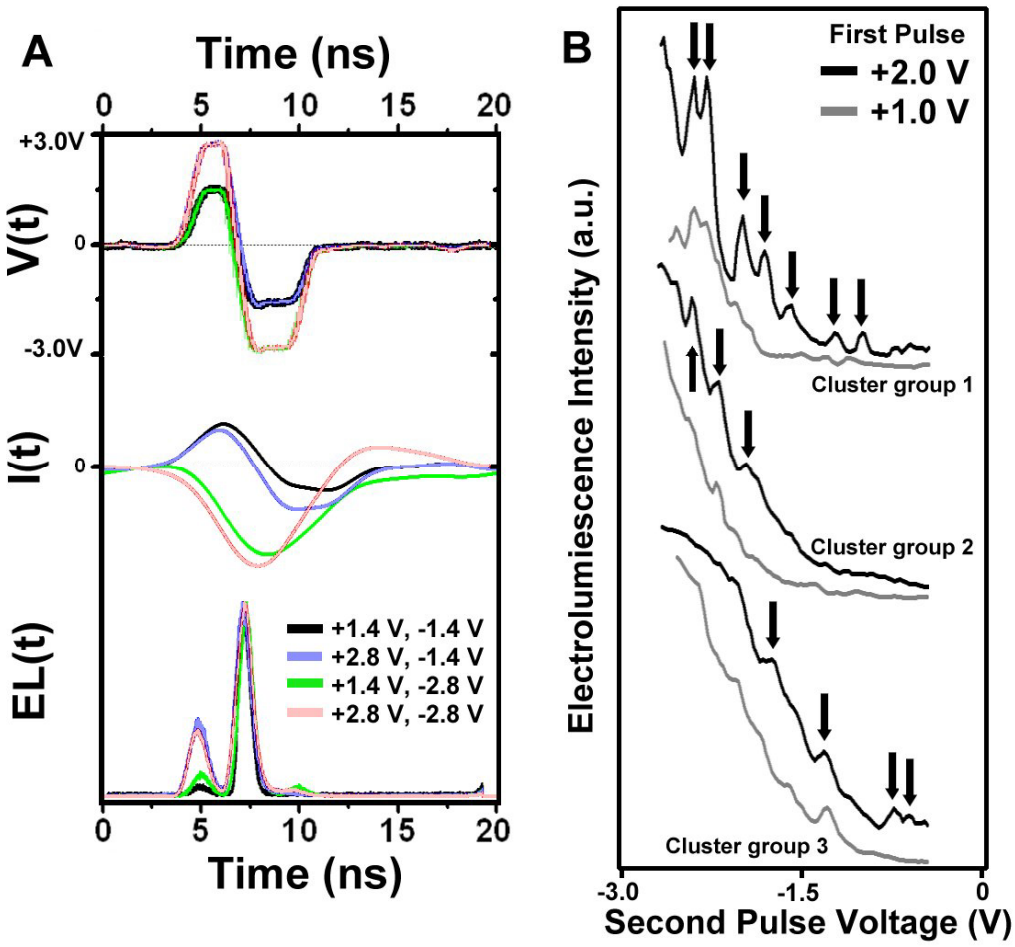

Figure 4.3. Pulse-amplitude dependence of electroluminescence (A) timing and (B) intensity. (A) Four different excitation sequences of varying pulse amplitude produce a time-dependent total junction current and normalized electroluminescence. All four EL traces were collected from the same individual gold nanodot. One 20-ns period of the excitation is shown. (B) The three plots summarize relative EL intensities from three distinct groups of gold clusters driven by varying pulse amplitude sequences. For each nanocluster group, a constant first-pulse voltage of +1.0 V (gray traces) or +2.0 V (black traces) was applied while the second-pulse amplitude was scanned from -0.3 V to -3.0 V with a resolution of ~0.05 V. Black arrows denote spectral peaks.

sequences result in a weak emission peak centered at 5 ns and a more intense peak centered at 7.5 ns. The relative intensity of the first EL peak in each case varies with each different excitation sequence. The small emission peak is produced solely by the first pulse in each excitation sequence, and its relative intensity is not affected by the second excitation pulse amplitude. This first peak's intensity increases relative to that of the second EL peak as the amplitude of the driving pulse is raised. Recall that generation of this first emission peak requires simultaneous hole- and electron-injection from the anode and cathode, respectively. Further raising the potential for anode-coupled hole-injection (first pulse) past the cluster turn-on voltage is unlikely to increase the electroluminescence efficiency because of very fast electronic reorganization of valence-band holes.[97, 98] However, an increase in the cathode-coupled driving potential would help to counter preferential injection of holes from the anode by increasing the likelihood of electron injection from the cathode. For two-pulse driven emission, the fraction of total cluster electroluminescence produced by single-pulse driven injection (simultaneous carrier injection from both electrodes) is constant for a given first pulse amplitude but increases as this voltage is raised. The appearance of a much smaller, third emission peak at ~10 ns (Fig. 4.2A, 4.3A) is likely due to harmonic ringing of the electron-driving potential across the cluster-anode gap. The peak intensity increases with second pulse amplitude and vanishes for excitation voltages less negative than -1.8 V.

Regardless of the driving field, an individual cluster's total electroluminescence output is determined by the injected-electron energy distribution, the degree of overlap between this distribution and the molecule's density of states (DOS), and the electrode-cluster coupling strength. Resulting from inelastic electron tunneling, pulsed

electroluminescence requires anode-cluster coupling weak enough to allow charge separation but sufficiently strong to facilitate resonant transport into nanocluster excited states. This weak coupling regime and sufficiently large electrode-molecule tunneling gap prevents significant energy level broadening and modification of the molecule DOS. Fixing the excitation first-pulse amplitude at +1.0 V and scanning the second-pulse amplitude from -0.3 V to -3.0 V (Fig. 3B, gray traces), we can precisely scan the chemical potential of the anode relative to individual nanocluster eigenstates. Consequently, total EL plotted against second-pulse amplitude constitutes a particular molecule's EL excitation fingerprint that includes information about coupling, energy overlap, and the density of states at each excitation voltage. Successful extraction of information about nanocluster eigenstates from EL fingerprints is made all the more challenging by the dynamic nature of the electrode-molecule coupling strength.[49] To address this problem, the EL outputs were averaged over several scans for a cumulative time of 30 seconds at each excitation energy. From a total of 38 nanoclusters studied, 12 showed EL excitation voltage fingerprints with reproducible peak structures significantly different from the bulk response of all molecules in the junction. The remaining 26 nanoclusters showed either spectrally dynamic peaks or a monotonically increasing EL intensity with no discernible structure, suggesting that these measurements may be obscured by large electrode-molecule coupling fluctuations. From the original 12 nanoclusters with discrete injection energies, three distinct groups of identical excitation spectra were identified and plotted (Fig. 4.3B). Cluster groups 1, 2, and 3 are respectively composed of two, six, and four nanoclusters with identical, but slightly offset, peak structures. For example, the EL fingerprints from six individual gold nanoclusters

comprising cluster group 2 show the same series of three peaks at approximately -1.9 V, -2.3 V, and -2.6 V with identical relative intensities. While the energy spacings between the peaks are identical in all six fingerprints, the absolute peak positions from molecule to molecule may vary by as much as 0.3 V. The observed shifts in peak energy are well below the nanocluster HOMO-LUMO gap (~1.8 eV)[48] and likely arise from local variations in geometry surrounding individual nanoclusters which, in turn, modulate the local work function and shift the cluster states relative to the electrode Fermi energy.[39] Numerically removing the offsets prior to summing the fingerprints in each cluster group reveals an electroluminescence excitation spectrum for three distinct types of gold nanoclusters created within electromigration-induced breakjunctions (Fig. 4.3B). Increasing the hole-injection driving potential (first-pulse amplitude) increases the total EL intensity, but the presence of these peaks is independent of first-pulse amplitude. Driving the EL with a +2.0V first-pulse (Fig. 4.3B, black traces) improves the modulation depth of all peaks without a significant change in their relative positions, consistent with an increased likelihood of anode coupled hole-injection that translates into a higher rate of electroluminescence.

Consistent with previously reported EL mechanisms in silver nanoclusters,[39, 97] the electroluminescence intensity from gold nanodots is proportional to the tunneling current between an emitting molecule and the injecting electrode. The observation of discrete peaks in the excitation spectra (Fig. 4.3B) suggests much narrower electron energy distributions than present in the high coupling limit of simple resonant tunneling through electrically-contacted organic molecules.[22] In this type of molecular wire, all electrons below the chemical potential of the contact can tunnel through available

conductance channels giving rise to a so-called "eigenvalue staircase."[89] Following hole-injection into the nanoclusters (ionization), resonant electron re-injection likely proceeds through field emission from the anode. The Fowler-Nordheim description of field emission predicts very narrow tunneling electron energy distributions exhibiting scattering structures due to the discrete energy levels of surface adsorbates.[44, 120, 121] The observed peaks in the EL excitation spectra (Fig. 4.3B) represent a direct measurement of each cluster type's DOS convolved with a narrow field emitted electron energy distribution at each applied potential. While the excitation peaks are well-defined, the observed modulation depth in each spectrum is limited by vibronic and electrode coupling, thermal broadening of the discrete cluster states at room temperature, and non-resonant tunneling into emissive states. All three cluster group spectra (Fig. 4.3B) show peak progressions starting at or below -0.8 V with an average turn-on threshold at approximately -1.5 V, consistent with time-resolved measurements described above (see Fig. 2B). In addition, we observe a leveling off of EL intensity at applied potentials below -2.5 V, and well-defined peak structures give way to broad features (Fig. 4.3B). This leveling of the EL likely arises from a combination of factors including significantly increased two-electrode driven emission at higher potentials and resonant injection into high energy cluster conduction bands with nearly-constant DOS.

4.2 Electroluminescence Lifetimes

Time-resolved characterization of individual gold nanocluster EL decay lifetimes poses several challenges. Because of large heterogeneities in the electrode composition and local geometry surrounding the clusters, the same excitation profile applied to many

molecules may result in a distribution of work functions, tunneling barriers, and turn-on voltages. Time-resolved collection of individual cluster EL is readily achieved by modulation of the driving field as in AC or pulsed mode, but a lack of information about cluster injection timing and the underlying electro-optical instrument response function precluded accurate deconvolution of the nanocluster response. To gain an understanding of the relationship between excitation profile and instrument response, time-correlated single photon counting measurements of electroluminescence from the same molecule were compared for AC and two-pulse driving fields of equal amplitude (Fig. 4.4). The frequency components of the pulsed anode and cathode injection profiles (Fig. 4.4A) were chosen to maximize the rate of electroluminescence and minimize junction ringing (see Fig. 4.1). The AC driving field frequency (245 MHz) was adjusted to match the dominant falling and rising slopes of both pulse polarity sequences (Fig. 4.4A). In either pulse pair polarity sequence, electron-injection (and most of the EL) is driven by the second pulse; in AC mode, electron-injection is driven at 0 phase from the anode and at π phase from the cathode. Therefore, a direct comparison of the two-pulse driven emission from our three excitation modes (AC, positive-negative pulse pair, and negative-positive pulse pair) can be made by overlapping the portions of the excitation signals responsible for electron-injection. In other words, the two-pulse excitation profiles have been artificially offset by one-half period of the AC field such that the beginning of each second pulse in the anode and cathode driving sequences coincides with the AC trough and crest, respectively. Shifting the EL decay traces (Fig. 4.4B) by the same offsets applied to their generating excitation profiles and normalizing for total intensity results in near perfect overlap of the anode- and cathode-driven response functions. Recall that all

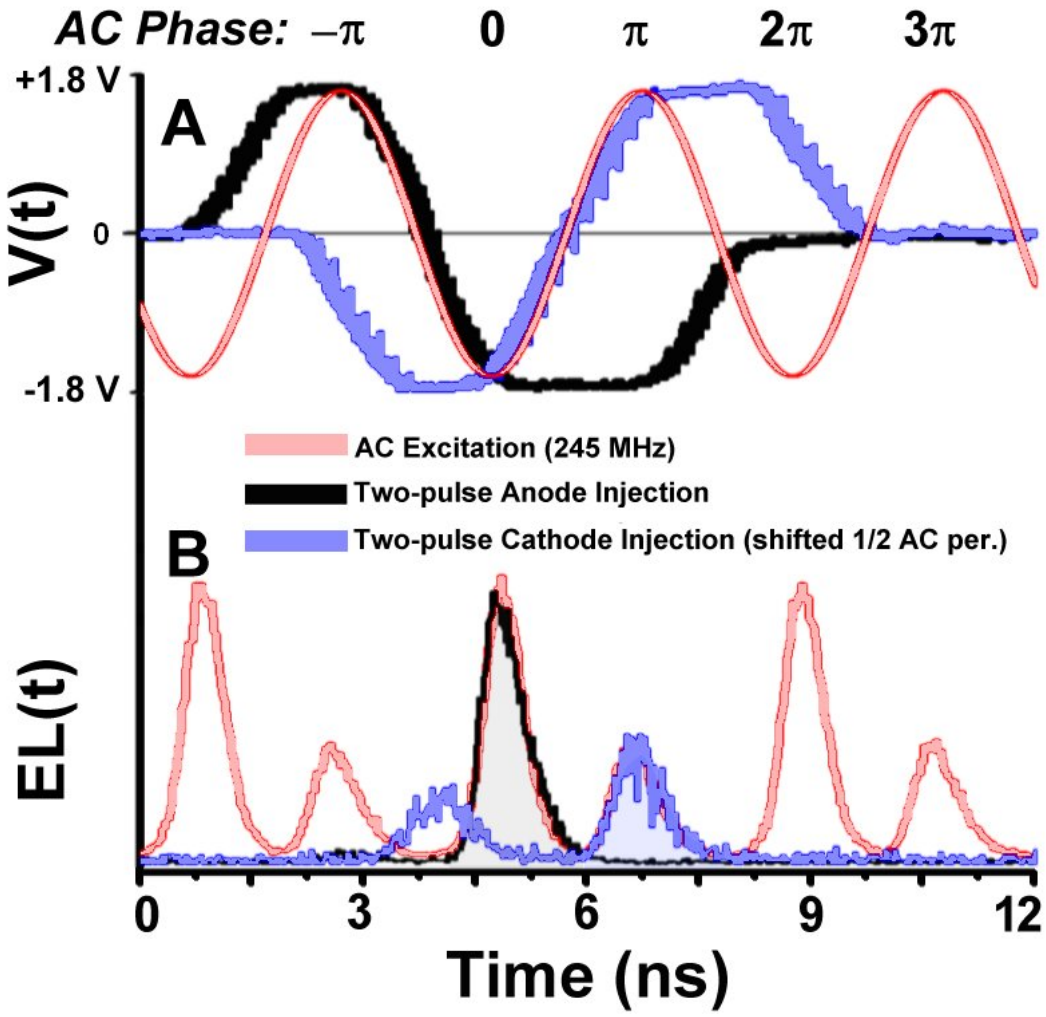

Figure 4.4. Time-dependent excitation (A) and electroluminescence (B) decay profiles for anode-, cathode-, and AC-driven emission. The maximum and minimum voltage in all excitation profiles is ±1.8 V (into 50 Ω). The dominant anode- and cathode-driven emission peaks have been shifted and normalized to coincide with AC-driven electron injection from the anode and cathode, respectively.

electroluminescence is generated near the beginning of each pulse as threshold values are reached (see Fig. 4.2B). The two-electrode driven EL (first peak) in both pulsed decay traces (~2 ns and ~4 ns) are not expected to coincide with any AC-driven emission because the first-pulse width in both cases is much longer than the crest-to-trough time of the sinusoidal field.

Because the EL decays show a high degree of overlap and were collected from one individual nanocluster, the same ~1.5-V EL turn-on threshold revealed in pulse-width tuning measurements (see Fig. 4.2B) may be assumed under AC excitation. This result indicates that electron-injection is driven only while the AC potential exceeds 1.5 V. In other words, only the top 17% of a ±1.8 VAC excitation profile drives re-injection leading to electroluminescence. The best fit of the one-electrode driven emission peaks (Fig. 4.4B) is achieved by convolution of our APD detector response (~500 ps) and a sinusoidal ±1.8 V profile truncated below 1.5 V with a single-exponential decay time of ~350 ps. This result is consistent with our previous ~400-ps estimate of gold nanocluster lifetimes using photon correlation measurements of antibunched electroluminescence streams[48].

In summary, we have observed electroluminescence-assisted inelastic tunneling between the electrodes of a nanoscale breakjunction and the individual gold quantum dots within it. By conditioning the molecule with specific electrical excitation pulse polarity sequences, we are able to control the injection timing and energy distribution as well as the relative coupling to the individual electrodes. Even at room temperature, electrical excitation spectroscopy of individual gold nanoclusters reveals electroluminescence from discrete molecular energy levels.

V. PHOTON CORRELATION AND QUANTUM-MECHANICAL ELECTROLUMINESCENCE

The variety of demonstrated quantum mechanical light sources as well as proposed schemes implementing nonclassical states has grown tremendously over the past few decades[122-131]. For example, the use of nonorthogonal bases with quantum mechanical emitters is the cornerstone of many proposed ultrasecure encryption schemes[125, 126]. This application of single-photon sources will be expanded upon later in this chapter, but a discussion of how these sources are created and characterized compels us to first define single-photon states.

5.1 Photon-Number States

When partially reflected and made to interfere on multiple detectors, the electromagnetic field produced by the radiative decay of single atoms or molecules exhibit distinctly quantum mechanical effects that cannot explained by a classical description of the light beam. Such phenomena illustrate the photon (or quantum) nature of light and consequently require a quantum mechanical treatment of the electromagnetic field. Formally, each mode of a quantized electromagnetic field having creation and annihilation operators a^+ and a may be described by[132, 133]

$$\hbar\nu\left(a^+a+\tfrac{1}{2}\right)|n\rangle = E_n|n\rangle, \tag{5.1}$$

where ħ is Planck's constant and ν is the mode's frequency. In this framework, n represents the number of photons in some mode with eigenstates (called Fock states or

photon-number states), $\{|n\rangle\}$, of energies, $\{E_n\}$. The photon-number states and their eigenvalues are summarized by[132]

$$|n\rangle = \frac{(a^+)^n}{\sqrt{n!}}|0\rangle \tag{5.2}$$

and

$$E_n = \left(n + \tfrac{1}{2}\right)\hbar\nu\,, \tag{5.3}$$

such that

$$a^+ a|n\rangle = n|n\rangle \tag{5.4}$$

with the usual commutation relation for the creation and annihilation operators,

$$\left[a, a^+\right] = 1\,. \tag{5.5}$$

A linear superposition of the photon-number states of each mode gives the total state of the electromagnetic field, i.e.,

$$|\psi\rangle = \sum_{\{n\}} c_{\{n\}} |\{n\}\rangle \tag{5.6}$$

Pure single-photon states are simply linear superpositions of photon-number states with no more than one photon (n=0,1) in each mode.

5.2 Single Photon Sources in Perspective

One interesting application of nonclassical emitters is in the field of quantum cryptography. In any exchange of secret information, two communicating parties wish to transfer a message while safeguarding against a third party eavesdropper. Classically, this is routinely accomplished by generation of a random electronic "key" (a sequence of binary bits) which is combined with the secret message prior to transmission. To decrypt the information, the intended recipient (and the eavesdropper) requires the sender-

generated key, and secure transmission depends on the security of the key. Routinely employed (classical) methods of key distribution inherently suffer from the fact that eavesdropping can occur without the communicating parties' knowledge. This problem can, in principle, be avoided by using a key composed of quantum mechanical information. Thus, quantum key distribution schemes such as the Bennet-Brassard protocol[123] ideally rely on the creation of highly polarized, wavelength-tunable pure single-photon states.

Single photon states may be prepared by attenuation of pulsed laser sources such that each pulse of the emission contains at most one photon[134]. The degree of attenuation required to achieve this condition is generally quite large and results in complete blocking of most of the laser pulses. Consequently, this approach to single-photon generation results in data rates far below the laser pulse frequency. In addition, attenuation alone cannot guarantee a zero probability of simultaneous two-photon emission. Alternatively, single photon states are readily prepared by laser-induced fluorescence of a single-quantum system. As all materials must relax with a characteristic time constant before reexcitation, simultaneous emission of two or more photons is forbidden for spatially isolated single-quantum systems. Thus, single atoms[128, 130, 135-137], molecules[138, 139], polymer nanostructures[140, 141], color centers in diamond films[142, 143], and even several-nm semiconductor quantum dots[144-146] have each been observed to emit no more than one photon at a time, independent of optical excitation intensity. The long-radiative lifetimes (> 1 ns) characteristic of fluorescent dyes and semiconductor quantum dots limit single-photon data rates but enable characterization with slower, high sensitivity detectors. While nonclassical laser-induced fluorescence has been observed

from a variety of materials, single molecule electroluminescence offers pronounced advantages by avoiding background, complexity, and cost resulting from high intensity laser excitation. Toward this goal, electrically driven nanoscale light sources have been demonstrated in carbon nanotube field-effect transistors[147], semiconductor nanowires[148], and semiconductor quantum dots at cryogenic temperature[93].

5.3 Degree of Second-Order Coherence

Verification of a light source's quantum mechanical nature ultimately requires a direct measurement of the photon statistics. An electromagnetic field's degree of second-order coherence[132, 133], denoted by $g^{(2)}(\tau)$, represents the probability of photon-pair detection using two detectors (one for each photon in the pair) separated in time by an arbitrary delay, τ. For a classical field, the observable is the light's intensity and $g^{(2)}(\tau)$ represents the intensity autocorrelation where τ is the correlation lag time. In the case of nonclassical single-mode light, the quantum degree of second-order coherence is directly related to the photon number, n, by the relation[133]

$$g^{(2)}(\tau) = \frac{\langle n(n-1)\rangle}{\langle n\rangle^2}, \tag{5.7}$$

where the brackets around each quantity represent its time-averaged expectation values. Note that while the photon-number, n, can only take on positive integer values, its mean (and thus $g^{(2)}(\tau)$) can take on any positive real value. The relationship between $g^{(2)}(\tau)$ and the photon number in eq. 5.7 provides an experimentally observable quantity that is very sensitive to the nature of the light beam. The denominator here is required for normalization. It is important to note that the quantity $\langle n(n-1)\rangle$ in the numerator

represents the average product of two *successive* (not simultaneous) measurements of a field's photon number. This subtlety may be intuitively understood by realizing that two separate observers may never detect the same photon. The numerator in equation 5.7 helps to illustrate the difference between $g^{(2)}(\tau)$ of classical versus quantum mechanical light underscoring the principle that observation of a quantum system alters its state. The quantum state being measured here is the field's photon-number which, upon measurement, changes from n to n-1. Because the intensity of a classical field is not altered by its measurement, autocorrelation at $\tau=0$ is equivalent to the intensity squared which upon normalization yields $g^{(2)}(0)\geq 1$. As expected from eq. 5.7, $g^{(2)}(\tau)$ for quantum mechanical light approaches unity for very large photon numbers. The minimum value of $g^{(2)}(\tau)$ for single-mode light is then given by the inequality[133]

$$g^{(2)}(\tau) \geq 1 - \frac{1}{\langle n \rangle}, \qquad \text{for } \langle n \rangle \geq 1. \tag{5.8}$$

In other words, the minimum value of $g^{(2)}(\tau)$ for a single-photon field is 0, and this minimum value approaches 1 for large mean photon-number.

As mentioned above, demonstration of pure single-photon emission from individual species is accomplished by measuring the light's degree of second-order coherence (in practice, this is equivalent to measuring the intensity autocorrelation function), $g^{(2)}(\tau)$, in a Hanbury-Brown and Twiss configuration[149] (see chapter 2). In such an arrangement, we measure the probability of detecting two individual photons as a function of arrival time difference, τ. Since simultaneous emission of two photons is forbidden for a single-quantum system, the intensity autocorrelation function approaches zero at zero delay, an effect known as photon antibunching. Observation of $g^{(2)}(0) \approx 0$ thus represents a definitive signature of sub-Poissonian light and is obtainable only from

a true single-quantum mechanical source[133]. Driven by a constant excitation field such as a CW laser or DC electric field, light emitted by n independent quantum mechanical systems will exhibit photon antibunching with $g^{(2)}(\tau)$ of the form[132, 133, 150]

$$g^{(2)}(\tau) = 1 - \frac{1}{n}\exp\left(-\tau\left(\alpha^{-1} + \omega\right)\right), \tag{5.9}$$

where α is the spontaneous radiative lifetime of the system's excited state and ω is the pumping rate (Fig. 5.1). The second term in the exponential may be ignored in most examples of low power laser-induced single-molecule fluorescence and in the case of gold nanocluster electroluminescence for which $\alpha^{-1} >> \omega$ (the inverse radiative lifetime is ~2.5 GHz and typical excitation rates rarely exceed ~40 kHz)[49]. The degree of second-order coherence is related to the second-order correlation function, $G^{(2)}(\tau)$, which is commonly used in measuring correlations from independent sources (e.g., in astronomy to distinguish the radiation from different stars);[149] its value increases from 1 to 2 as the mean photon number approaches 1, with its maximum value given by $1 + \frac{1}{\langle n \rangle}$.

5.4 Antibunched Gold Nanodot Electroluminescence

In this section, we demonstrate robust, nonclassical electroluminescence at room temperature from spatially isolated Au nanoclusters within easily fabricated dc-generated nanoscale break junctions. Behaving as single-quantum systems (analogous to multielectron artificial atoms)[82], these electrically contacted, spatially isolated gold nanoclusters exhibit clear photon antibunching in their strong, near-infrared electroluminescence. This result clearly establishes the viability of these species in a

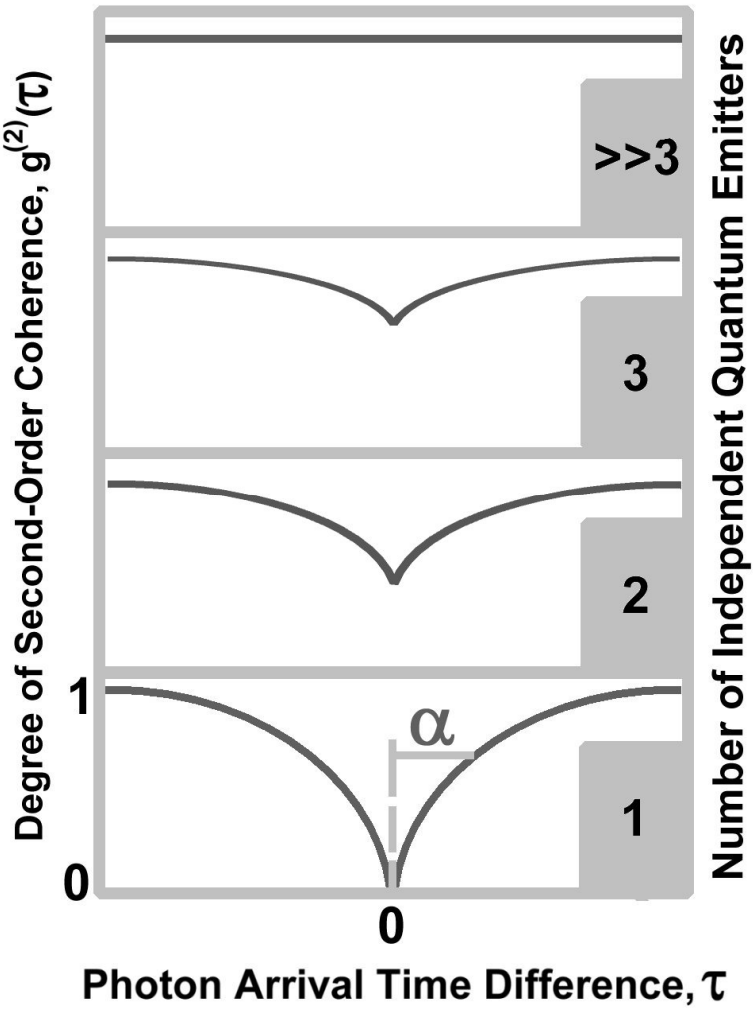

Figure 5.1. Degree of second-order coherence, $g^{(2)}(\tau)$, for an increasing number of independent quantum emitters with radiative lifetime α in the limit of $\alpha\omega \ll 1$. $g^{(2)}(\tau)$ is equivalent to the EL intensity autocorrelation measured in a Hanbury-Brown-Twiss interferometer.

photonic quantum information processing context, and suggests a promising new direction in the field of nanoscale quantum optoelectronics.

As described in previous chapters, low density arrays of 18–22 atom Au nanoclusters are produced in situ during electromigration-induced break junction formation[48, 49], allowing facile electro-optical interrogation of individual strongly electroluminescent species within the nanoscale gap (Fig. 5.2(a)). These molecule-like species exhibit clear dipolar radiation patterns under optical and electrical excitation suggestive of individual quantum emitters (Fig. 5.2(b)). While antibunched emission from electrically excited semiconductor quantum dots has been reported[93], this has only been possible in complicated nanofabricated devices at cryogenic temperatures due to the shallow electron well and band structure of several-nanometer semiconductor quantum dots[151]. While a great advance, the nonclassical, long-radiative lifetime electroluminescence disappears rapidly with increasing temperature, precluding anything but cryogenic measurements. The several-atom size of our Au nanoclusters and their behavior as multielectron artificial atoms[82], dictates that the density of states is sufficiently low such that the energy level spacings are large compared to ambient thermal energies. Consequently, in contrast to much larger semiconductor quantum dots, these Au dots should easily continue to operate far into the near IR at room temperatures.

Gold nanoclusters within electromigrated break-junctions not only electroluminesce, but also strongly fluoresce when excited at 532 nm, thereby enabling optically excited lifetimes of ~600 ps to be measured with pulsed laser excitation and time correlated single-photon counting detection (not shown). Au electroluminescence lifetimes were measured to be slightly faster (~400 ps) through comparison with

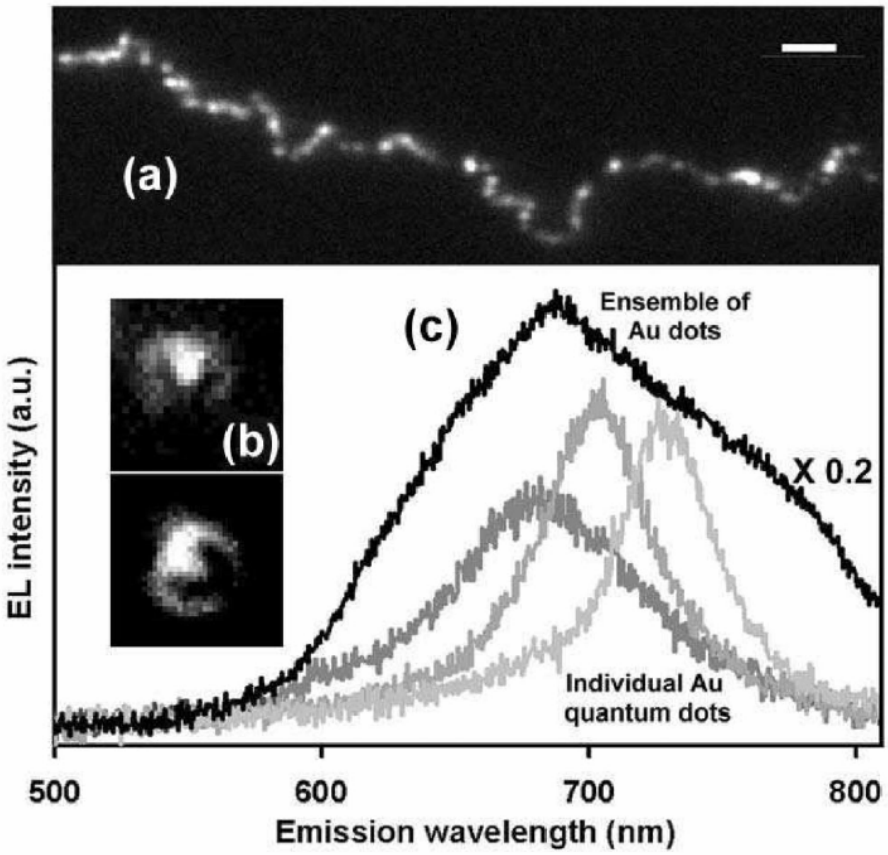

Figure 5.2. Au nanodot electroluminescence. (a) Electroluminescence (EL) from a gold nanodot array within a nanoscale break junction under high frequency AC excitation (±2.5 VAC, 220 MHz, scale bar: 5 μm). (b) Dipolar emission from individual dots. (c) EL spectra of three typical single-gold quantum dots (gray traces) compared to that of an ensemble (black line). Although both homogeneously and inhomogeneously broadened, each single dot spectrum exhibits a much narrower linewidth than does the ensemble spectrum and they range in emission maximum from ~650 to ~750 nm, corresponding to sizes of 18–22 atoms. All spectra were collected through a 300 mm imaging monochromator (Acton) with a 150 l/mm grating.

instrument response-limited Ag nanocluster emission and by deconvolution of the excitation profile above the cluster turn-on voltage (see chapter 4). Optical excitation coaxes spectrally indistinguishable emission from more molecules than does electrical excitation (Fig. 5.2); however, as only a subset of Au nanoclusters have the proper electrical contacts to electroluminesce (EL), slight quenching of the emission likely produces the slightly shorter EL lifetime.

Au nanoclusters within the nanoscale junctions are most conveniently excited with low voltage (5 V*p-p*) AC frequencies corresponding to the junction transmission window at ~220 MHz. The junction acts as a bandpass filter that is properly impedance matched only at the frequency corresponding to the transmission maximum. These junctions operate effectively as series resistor-inductor-capacitor circuits, thereby enabling low power excitation at very high frequencies[40]. The junction transmission frequency is readily tuned through computer controlled, DC-induced electromigration of the metal film. Individual Au nanoclusters are easily spatially isolated within the junction with continuous individual nanocluster emission remaining bright for several hours and junctions retaining many emissive nanoclusters for several days of operation. DC operation yields bright EL, but the high power necessary to overcome the high DC impedance rapidly restructures and destroys the junctions, precluding DC $g^{(2)}(\tau)$ measurements. Once obtained, ac-excited single nanocluster emission is equally split and aligned onto two 100 μm fiber-coupled avalanche photodiodes yielding detected electroluminescence count rates (> 10 kHz) from individual features.

The spatial distribution of emissive nanoclusters within the junctions is asymmetric with more emitters being closer to the anode as defined by the dc fabrication

process. As discussed in chapter 4, these gold junctions operate with overall asymmetry in emission and demonstrate weak light-emitting diode behavior due to preferential electron injection through the anode. Because the total time-dependent AC-driven EL is composed of an anode contribution and a delayed cathode contribution, the ensemble (multiparticle) $g^{(2)}(\tau)$ (Fig. 5.3(a)) takes the form of the total (anode *and* cathode) EL autocorrelation,

$$g^{(2)}(\tau) = \left(EL_A \oplus EL_C\right) \otimes \left(EL_A \oplus EL_C\right), \tag{5.10}$$

with sinusoidal oscillations at twice the AC drive frequency of alternating intensities. The subscripts here denote the injecting electrode responsible for electroluminescence ("A"node or "C"athode), and the "⊗" and "⊕" symbols represent correlation and direct sum operators (respectively) of each contribution to the time-dependent emission. The alternation in the degree of second-order coherence is a direct result of preferential anode injection and may be intuitively understood as the sum of four EL correlation functions. Expansion of equation 5.10 gives

$$g^{(2)}(\tau) = \left(EL_A \otimes EL_A\right) \oplus \left(EL_C \otimes EL_C\right) \oplus \left(EL_A \otimes EL_C\right) \oplus \left(EL_C \otimes EL_A\right). \tag{5.11}$$

Accordingly, the first two terms in the expression are the autocorrelations of the separate anode and cathode contributions to EL that give rise to the central peak (τ=0) in $g^{(2)}(\tau)$ and all peaks at integer multiples of 2π. The third and fourth terms in the expression correspond to the cross-correlation of anode-driven light with cathode-driven light and are manifested as smaller peaks in $g^{(2)}(\tau)$ shifted in phase by π. The intensity modulation at 220 MHz indicates that electroluminescence results from preferential injection through one electrode (the anode) but also occurs to a lesser extent through the other (the cathode). This interpretation is confirmed by the observation of light-emitting diode behavior with

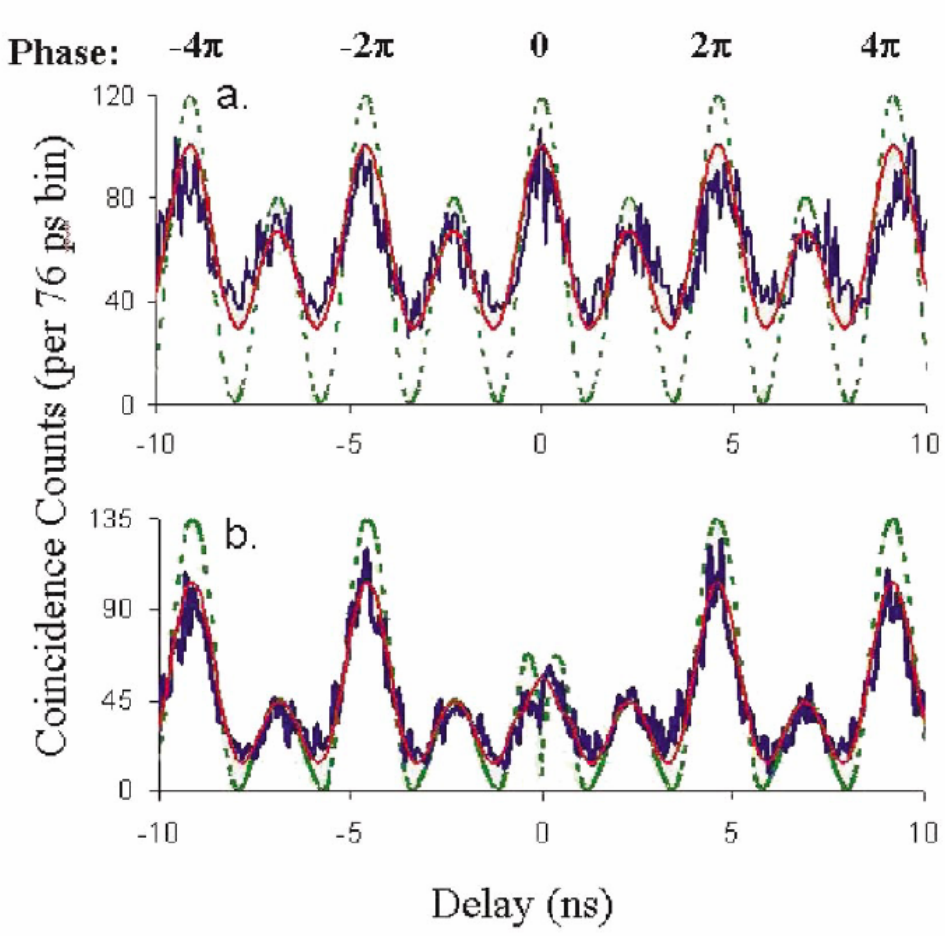

Figure 5.3. Measured (76 ps bins) and simulated degree of second-order coherence $g^{(2)}(\tau)$ of gold electroluminescence driven at 220 MHz. (a) EL intensity autocorrelation from a group of many gold dots (blue) overplotted with an ideal simulation (green dotted line) and after convolution with the finite time response of our detectors (1.1 ns, red line), all showing the 220 MHz AC excitation frequency. Smaller peaks shifted in phase by π radians arise from cross-correlation of anode- and cathode-driven EL. (b) Antibunching in single Au nanocluster electroluminescence (blue), overplotted with an ideal simulation (green dotted line), and its convolution with the detector response (red line). The small probability for injection through the cathode is again evidenced by the smaller peaks shifted by π. As described by the simulations, the $g^{(2)}(0)$ peak in (b) is substantially diminished relative to peaks shifted by higher multiples of 2π. Much faster than the AC excitation period (~4.55 ns), and the time resolution of our two APDs (1.1 ns), the short emission lifetime (~400 ps) limits the observable contrast in $g^{(2)}(\tau)$ measurements but allows for high single-photon data rates. Although readily apparent after only ~100 s, the high contrast $g^{(2)}(\tau)$ at high repetition rates such as that in (b) is obtained in 25 min. Only low frequency intensity changes are statistically significant as the time resolution is much longer than the bin width used.

an overall preference for injection through the anode as measured by the pulse polarity experiments described in chapter 4.

Further magnification of the electroluminescence image projected onto the fiber entrance enabled improved spatial discrimination and direct measurement of the intensity autocorrelation from individual nanocluster emission (Fig. 5.3(b)). In this case, antibunched electroluminescence is clearly observed as a significantly reduced coincidence count rate at zero delay. Additionally, the peaks shifted by π (resulting from cross-correlation of anode and cathode EL) are also significantly smaller than in the ensemble measurement, indicating the asymmetric coupling of the individual nanocluster to each electrode. Although emission appears pulsed due to ac excitation and preferential injection through the semiconducting anode, it is important to point out that the behavior of $g^{(2)}(\tau)$ near zero time delay is more similar to that produced by DC or CW excitation[93] due to the fast emission lifetime relative to the AC excitation period and the relatively long detector response, as shown in the simulation in Fig. 5.3(b). Convolution of the single dot intensity autocorrelation with the finite instrument response has the overall experimental effect of attenuating the peak height at zero delay and giving an effectively constant offset to the overall function. Consequently, the high frequency (76 ps bins) intensity fluctuations are statistical noise as the time resolution is limited by the relatively long collective avalanche photodiode (APD) response of ~1.1 ns. This particular manifestation of the antibunching signature is well represented in simulations incorporating the 220 MHz excitation, 400 ps electroluminescence lifetime, and 80% (20%) injection efficiency through the anode (cathode) (Fig. 5.3(b)). The experimentally observed degree of antibunching ($g^{(2)}(0) / g^{(2)}(2\pi) \sim 35\%$) is consistent with simulations

of an ideal single-photon source having essentially zero probability of simultaneous two-photon emission. However, we must acknowledge the possibility of a finite two-photon generation probability of ≤0.3 as a result of the obscuration of the true value of $g^{(2)}(0)$ that results solely from our detector time response.

The antibunched emission proves that Au nanoclusters behave as individual artificial atoms, and it opens new avenues for the study and application of small metal quantum dots in nanoscale quantum optoelectronics. The nanoclusters are small enough to have discrete, size-tunable emission at room temperature that can be harnessed to easily create arrays of electrically addressable single-photon sources. The high excitation rates (220 MHz) and short lifetimes produce high bit rates, at frequencies amenable to electro-optic polarization modulation, offering the ability to simultaneously drive an electro-optic modulator for in phase control of either polarization or intensity. Combined with the facile creation and utilization of room-temperature electrically excited single-photon source arrays, this offers the opportunity for synchronized modulation of both intensity and polarization for potential encryption schemes[123] using nonorthogonal polarization bases. In addition to their ease of fabrication, noble metal quantum dots are easily made to electroluminesce for several days of stable, room-temperature operation. These features could result in more easily transportable devices, making quantum cryptography much simpler to implement with true room-temperature nanoscale quantum optoelectronic elements.

VI. ELECTRICALLY-PUMPED GOLD NANODOT EMISSION SPECTROSCOPY

6.1 Emission Line Broadening in Quantum Optoelectronic Systems

In this chapter, we discuss gold nanocluster electroluminescence in terms of its emission spectrum. EL emission spectra can provide information about the molecule HOMO-LUMO gap as well as the coupling between the excited states and electrode states. In addition, EL spectral lineshapes reflect the energy distribution of tunneling electrons. Together with excitation spectroscopy, a study of the emission energy distributions can provide insight into the vibronic structures and dynamic interactions that govern inelastic nanoscale transport. First, an overview of some relevant spectral line broadening mechanisms is useful.

In the absence of system inhomogeneity and dynamics (i.e., a system of identical, non-interacting sources at equilibrium) the emission lineshape is dominated by homogeneous broadening. This type of broadening includes the effect of temperature on the emitter density of states and the occupation energy distribution of electrons in metal electrodes. Known as the Fermi function, this distribution is given by[1]

$$f(E) = \left[1 + \exp \frac{E - E_f}{k_B T} \right]^{-1} \tag{6.1}$$

where k_B is the Boltzmann constant, T is temperature, and E_f is the equilibrium chemical potential or Fermi energy. In bulk gold, E_f is approximately 5.5 eV.[82] This function can

also be used to describe the occupation of electrons in the metallic contacts of a MIM junction[2, 152] under an applied potential, V. In an ideal junction of parallel metal plates, the chemical potential of the left and right electrodes is shifted from the equilibrium Fermi energy by ±eV/2 producing a shifted distribution given by[16]

$$f_{L,R}(E) = \left[1 + \exp \frac{E - \left(E_f \pm \frac{eV}{2} \right)}{k_B T} \right]^{-1}, \tag{6.2}$$

where e is the electron charge and V is the applied potential. In the case of molecule-doped MIM junctions discussed in chapter 1 such as those studied by Lambe et al.,[2] the inelastic contribution to the current from vibronically coupled electron tunneling is proportional to the overlap integral of each state with the electrode Fermi distributions,[2] i.e.

$$I \propto \int dE \cdot f_L(E) \cdot [1 - f_R(E - \hbar\omega)]. \tag{6.3}$$

Here, $\hbar\omega$ is the energy of the molecular transition coupled to electron tunneling. Expression 6.3 can be evaluated and differentiated twice with respect to voltage as described by Lambe and Jalkevic,[2] i.e.,

$$I \propto k_B T \cdot \Theta \cdot \left[\frac{\exp(\Theta)}{\exp(\Theta) - 1} \right] \tag{6.4}$$

and,

$$\frac{d^2I}{dV^2} \propto \frac{e^2}{k_B T}\left[\exp(\Theta)\frac{(\Theta-2)\exp(\Theta)+(\Theta+2)}{(\exp(\Theta)-1)^3}\right], \tag{6.5}$$

where

$$\Theta \equiv \frac{E-\hbar\omega}{k_B T}. \tag{6.6}$$

A plot of the current vs. voltage (eq. 6.4) gives a monotonically increasing curve with no peaks. Plotting the second derivative of current with respect to voltage (eq. 6.5) results in an inelastic electron tunneling peak centered at an applied potential given by $\frac{\hbar\omega}{e}$ with an ideal temperature-limited full width at half maximum (FWHM) of 5.4 kT.[2] This is the expected width of the second derivative peak with respect to voltage in the limit of very narrow molecular excitation and arises solely from the electron distribution in the metal electrodes. In practice, other effects such as thermal and coupling-induced broadening of the molecular states will produce broader peaks.

In the case of field emitted electrons inelastically-coupled to molecular transitions, the total electron distribution peaks close to the electrode chemical potential with a distribution that is much narrower in energy.[44, 153, 154] The appearance of a peak and the narrow nature of the distribution arise from multiplication of the Fermi function by an exponential term in the expression for the field-emission current density.[155] The fall off of this exponential term, and hence the width of the current density, depend on the field

strength and the metal electrode's work function.[155] For example, the FWHM of the electron distribution emitted from a metal surface (work function ~ 4.5 V) falls between 100 meV and 200 meV even at room temperature and field strengths exceeding 10^9 V/m.[155] At room temperature, the width of the field-emitted electron distribution is much narrower than that of Fermi distribution limited inelastic tunneling current (*second derivative linewidth is limited to* ~140 meV FWHM)[2] in doped MIM junctions. So, in the presence of adsorbates or molecules separated from the surface by a tunneling gap, the much narrower energy distribution of field-emitted electrons enables a more selective probe of discrete molecular states.

The distributions described above give rise to homogeneous broadening of the electroluminescence and affect even *individual* molecule spectra in the absence of fluctuations due to transport dynamics. Sample inhomogeneity can also produce a broadened ensemble spectrum due to different molecule structures present in the junction as well as differences in the local environments surrounding individual molecules.[39]

Inhomogeneous broadening arises from effects that act differently on different radiating or absorbing species. For example, the linewidth of an atomic transition in the gas phase may be broadened by the different velocities of the atoms. Similarly, a molecular transition from molecules in a heterogeneous arrangement can be broadened by the different interactions of these molecules with different environments in the medium. In gold nanocluster EL, environmental differences in each molecule's position and orientation within the junction as well as the local electrode geometry, work function, and spatial distribution of the electrostatic potential can give each emitter a unique spectral signature[39] and broaden the ensemble spectrum In addition, some of these

parameters (i.e., the electrode-molecule coupling and temporary charging effects) fluctuate over time[49] and likely act as a source of inhomogeneous broadening in individual molecule spectra.

Narrowing of the spectral distribution from spontaneous emission (such as fluorescence and electroluminescence) can occur when there is sufficient optical gain through an effect called amplified spontaneous emission (ASE).[156-158] The optical gain is not uniform for all frequencies and selectively amplifies light matching the resonant cavity modes. Due to this finite gain bandwidth, the resulting emission spectrum is narrower than that of the original fluorescence or EL. ASE, which has been observed from semiconductor quantum dots in close packed solids,[159, 160] is characterized by good spatial coherence but (unlike stimulated emission) low temporal coherence.

The optical gain required for ASE can be achieved in an optical cavity with resonant cavity modes that fall within the emission bandwidth.[74] The degree of amplification, or gain, of the cavity must compete with the optical resonator's losses, which are related to the cavity's quality factor, Q, given by[74]

$$Q = \frac{\nu}{\Delta\nu}, \tag{6.7}$$

where ν is the resonant frequency of the mode being amplified and $\Delta\nu$ is the linewidth. The quality factor is essentially a ratio of energy stored per energy dissipated by the resonator, so a high Q corresponds to high gain. Other factors needed for ASE (as in semiconductor QDs) include a high volume fraction of emitters and the suppression of non-radiative recombination pathways.[159]

6.2 Emission Spectrum Field-Dependence

The EL spectrum from a typical gold nanocluster array excited by a ±2.5 V AC field (220 MHz) is shown in figure 5.2. The relatively high excitation voltage results in broad bulk emission (~400 meV FWHM) ranging from the near-IR (>800 nm) to about 575 nm with an emission maximum at ~690 nm. Individual gold nanocluster EL (see figure 5.2) is both homogeneously and inhomogeneously broadened with emission maxima ranging from ~650 nm to ~750 nm. Typical AC-driven spectral widths at room temperature range from ~100 meV to ~250 meV (FWHM), much narrower than the total junction emission and consistent with linewidths expected from inelastic electron scattering theory and the expected distribution of field-emitted electrons.[2, 155]

The field-dependence of electroluminescence intensity was discussed in chapter 3 (see figure 3.2), and we now expand the discussion to include the frequency and voltage dependence of EL spectra from individual nanoclusters. A contour plot of electroluminescence intensity from a typical individual molecule (Fig. 6.1(a)) summarizes the emission spectrum over a range of AC driving frequencies. The total EL intensity from the cluster exhibits several small peaks within the ~17-MHz window with a dominant resonance peak at 213 MHz. This particular molecule, excited with 1.8 Vpp has an emission maximum at 700 nm. As mentioned in chapter 3, the observed total EL enhancement at a particular resonance frequency is the direct result of the junction transmission window and represents an average of the individual molecule frequency responses. The specific resonance frequency for exciting a particular cluster depends on the transmission characteristics of the local electrode structure and nanoscale gap surrounding the molecule. While these factors certainly affect electrode-molecule

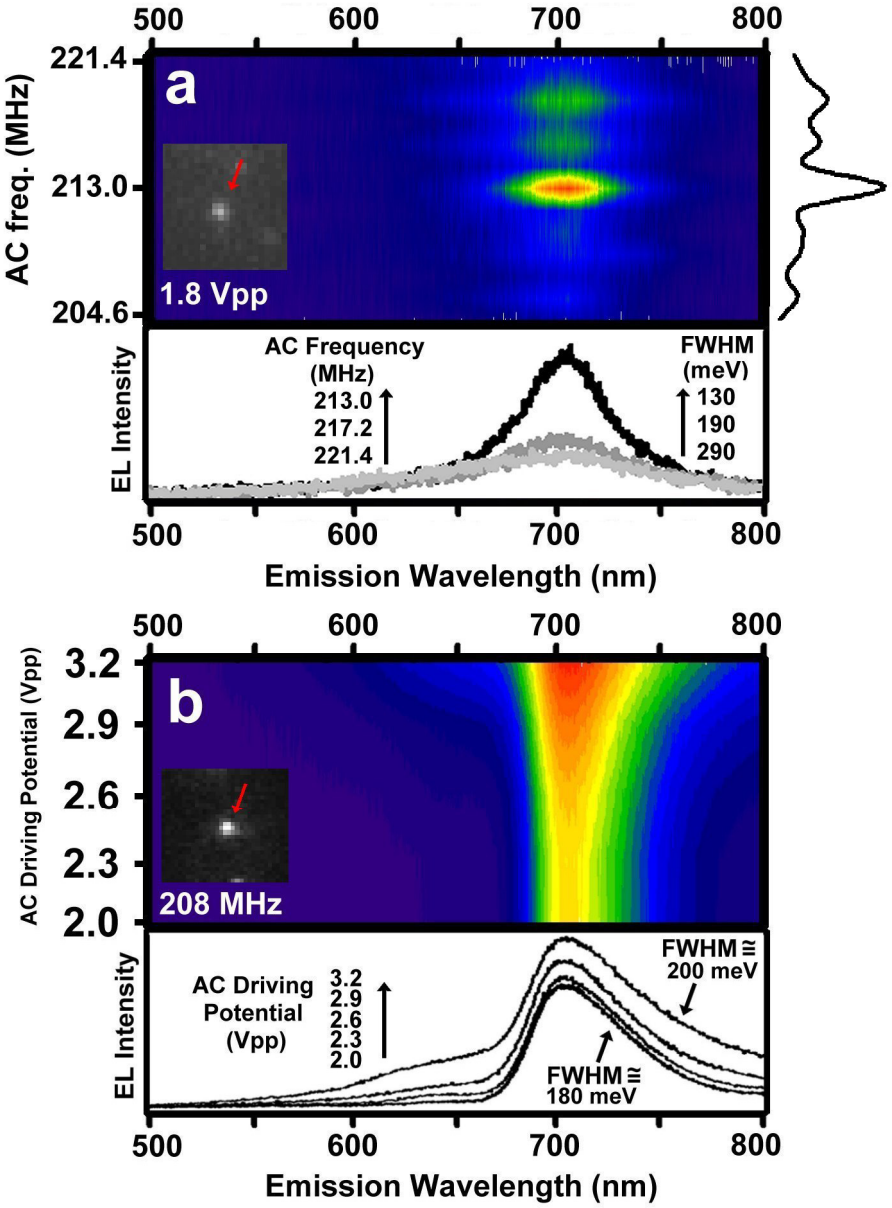

Figure 6.1. (a) Frequency and (b) voltage dependence of individual molecule AC-driven EL spectra. The two examples shown here are from different molecules. All spectra were collected through a 300 mm imaging monochromator (Acton) with a 150 1/mm grating. The collection time for each trace is 1 minute.

coupling, differences in carrier injection energy and timing are likely minimal. As such, the spectral maximum is not influenced by the AC driving frequency (Fig. 6.1(a)). However, the EL linewidth shows a modest decrease when driven at the resonance frequency. When detuned from its natural resonance frequency, the junction impedance rises creating a small amount of heat. The observed peak broadening under off-resonance excitation may be due to local heating of the junction surrounding the molecule.

The voltage-dependence of emission spectra is more dramatic and was demonstrated in EL from an ensemble of silver nanoclusters.[40] The contour plot in figure 6.1(b) shows how the EL spectrum from a typical individual gold cluster (excited at its resonance frequency) changes with applied voltage. The emission maximum (700 nm) exhibits no voltage dependence. Raising the AC voltage from 2.0 to 2.3 Vpp has very little effect on the EL spectrum, but spectral broadening is clearly observed for excitation above 2.3 Vpp. As the voltage is increased, nanoclusters exhibit a disproportionate increase in electroluminescence between 550 nm to 675 nm (Fig. 6.1(b)), suggesting emission from higher energy levels. The observed broadening with increased voltage is inhomogeneous and is likely due to changes in the excitation electron energy distribution with increased driving potential.[44]

6.3 A Special Case of Electrically-Pumped Cluster Emission

Of the more than 200 individual AC-driven gold nanocluster spectra recorded, seven exhibit a very narrow (<80 meV), temporary emission line (Fig. 6.2) growing in from a broad background EL peak over the course of a few minutes. While we see emission narrowing at a variety of driving frequencies and voltages, the effect has also

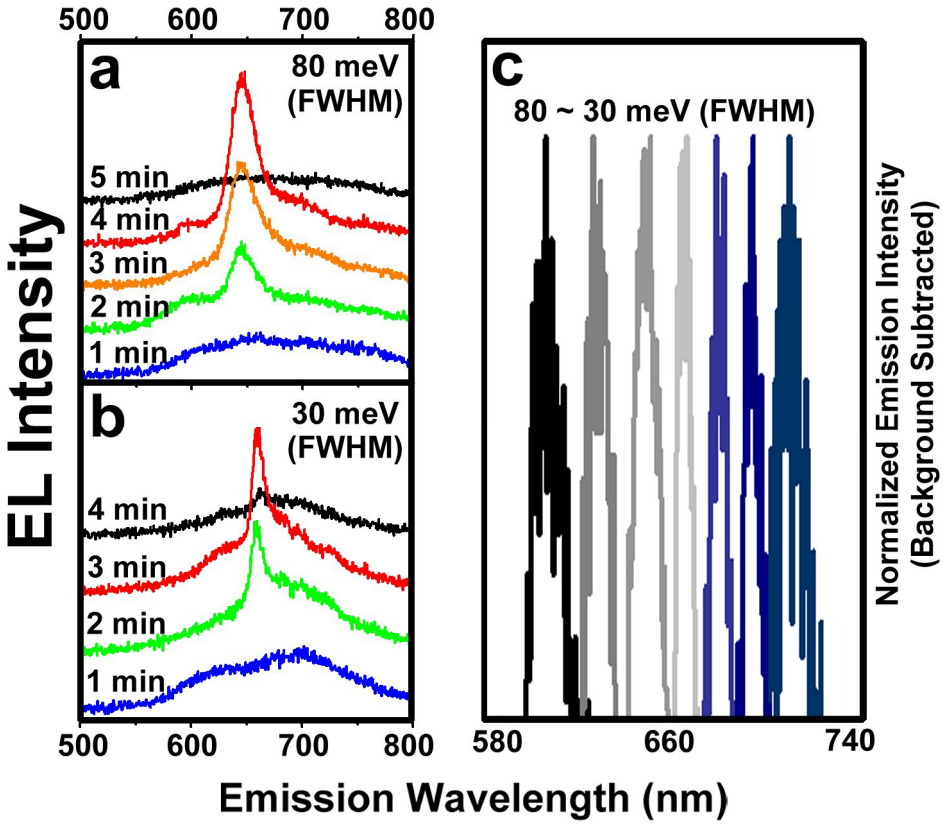

Figure 6.2. Temporary emission narrowing in individual molecule EL. Time traces of EL spectra from two different molecules (a) and (b) are shown lasting 4 and 5 minutes, respectively. (c) A summary of seven observed narrow peak spectra ranging in emission maximum from ~600 nm to ~720 nm. All spectra have been normalized, and the broad background EL has been subtracted. All spectra were collected through a 300 mm imaging monochromator (Acton) with a 150 1/mm grating. The collection time for each trace is 1 minute.

been observed without changing any excitation parameters. Collection of individual molecule EL spectra at reasonably high resolution and relatively low voltage requires long collection times (~1 minute per frame). For narrow lines lasting longer than one minute, a gradual increase in intensity is always observed followed by sudden disappearance of the peak (Fig. 6.2(a, b)). While the narrow spectral feature disappears after a few minutes, the broad background EL remains for the duration of the experiment. The emission maxima for the seven observed narrow features range from ~600 nm to ~720 nm (Fig. 6.2(c)).

The ASE mechanism of line narrowing was considered as a possible origin of the observed peaks. But while gold electromigrated junctions act as electrical resonators, there is no clear evidence of an optical cavity present to provide any optical gain. However, other optical effects may arise from electrostatic charging and interactions with electrical resonances. As mentioned in previous chapters, the gold electrodes of these nanoscale junctions act as series-RLC *electrical* resonators with Q ~ 20 measured by dividing the junction resonance frequency by the FWHM of the EL intensity vs. frequency plot (see chapter 3). The local value of Q for the electrodes surrounding an individual molecule can be much higher (Q ~ 70) as shown in figure 6.1 and the dynamic nature of the electrode-molecule coupling suggests that this value may fluctuate over time.

The conditions that give rise to the observed peak are unclear, but the apparent time-dependence of this effect under constant excitation suggests that the emission narrowing may arise from system transport dynamics such as coupling fluctuations, temporary charging near the molecule, or electrode restructuring effects.[49] First, we consider the role of electrode-molecule coupling fluctuations in line narrowing. Emission

narrowing is observed under AC excitation and never for DC excitation, suggesting that preferential electrode coupling likely plays a role. Typically, AC-driven EL can proceed by either simultaneous or sequential injection. In the latter case, *highly* preferred coupling to one of the electrodes can drive carrier injection almost exclusively from the preferred electrode resulting in a longer waiting period between hole- and electron-injection (~2.5 ns). The injected hole may, in principle, hop between several degenerate (or nearly-degenerate) momentum states in the cluster valence-band. Since direct electron-hole recombination requires an electron and hole of matching momentum, localization of the hole in one of these momentum states could give rise to a narrower EL spectrum. However, both the radiative lifetime of the electron-hole pair[48] and the reorganization time of valence-band holes[39] are much faster than this waiting period and are not likely to be involved in the observed emission narrowing.

The second effect under consideration is the temporary electrostatic charging discussed in chapter 3. In this case, the presence of a large charge reservoir (e.g, a large gold grain or nanoparticle) near the molecule may act as a temporary reference electrode effectively shifting the molecule levels relative to the electrode Fermi energy. In principle, a large enough shift of the molecule DOS could lower the coupling rate between degenerate momentum states. This change could result in a highly localized hole with preferred momentum and a well-defined energy for vertically allowed radiative recombination. The relatively low incidence (~4%) of clusters exhibiting this effect and its temporary nature are suggestive of electrostatic charging as discussed in chapter 3, but this is not conclusive and more work will be needed to determine the origin of these narrow peaks.

Finally, we consider the role of electrode restructuring in emission line narrowing. As in the electromigration-induced fabrication process, any applied bias on the electrodes will cause some degree of restructuring. Even though the applied potentials and current densities during AC operation are much lower than used in junction creation, a small amount of dynamic restructuring of the electrodes is to be expected. Rearrangements of the electrode surface result in a change of the electrostatic potential spatial distribution, and the formation of atomic scale adsorbates near the emitting gold cluster or molecule can act to narrow the excitation electron energy distribution. This is a more plausible mechanism for the observed emission line narrowing than the decoupling of momentum states described above, but it is also inconclusive requiring further study.

Our unique ability to track transport dynamics may allow further investigation of this phenomenon. One avenue for continued study of this effect is the incorporation of a third electrode separated from the junction by an oxide layer. The gate electrode would act as a reference to float the molecule DOS in a controlled manner, and could help elucidate the effects of electrostatic charging on the EL spectrum. In addition, temperature-dependent studies of the transport dynamics and spectra may provide a better understanding of the system's heterogeneity.

VII. CONCLUSIONS AND OUTLOOK

Fulfilling the promise of molecular electronics will require an understanding of the physical phenomena that govern nanoscale transport as well as the emergent dynamics that arise from the molecule's quantum-mechanical nature and interaction with its surroundings. A thorough appreciation of the electrode-molecule contacts is crucial in this respect because of the electrodes' heterogeneity and changing structure that can lead to electrode-molecule coupling fluctuations. But, for several reasons, a good grasp of the contact couplings is unattainable by electrical measurements alone. There are several alternate transport pathways through a junction at any one time and, each one is regulated by dynamic variables. Revealed by this research, electrode-molecule couplings are readily probed by the individual molecule's light emission resulting from inelastic transport. Most importantly, single-molecule electroluminescence is a non-controversial, corroborative tool to track nanoscale transport dynamics in real time through a molecular electronic structure.

Common to molecular electronics studies, nanoscale break junctions created through electromigration also naturally produce electroluminescent arrays of individual gold nanoclusters spanning the electrodes. These nanoclusters exhibit bright, field-dependent emission in the near infrared (650–800 nm). Intensity autocorrelation of spatially isolated individual nanocluster emission driven at high electrical frequency (f_{AC} ~ 200 MHz) reveals antibunched electroluminescence at room temperature. These results demonstrate the single quantum nature of several-atom gold molecules and suggest their use as room-temperature electrically driven single-photon sources.

Arrival time stamping of detected photons demonstrates that charge injection to the clusters is directly modulated by dynamic coupling to individual electrodes. These several-atom nanoclusters ($Au_{\sim 18\text{-}22}$) electroluminesce due to inelastic electron tunneling into cluster electronic energy levels. AC electrical excitation with time-stamping of photon arrival times enables fast and local tracking of electrode-nanocluster coupling dynamics. The electrode-nanocluster coupling rate fluctuates by nearly an order of magnitude and, due to the asymmetry of the electromigration process, exhibits preferential charge injection from the anode. Directly reporting on (and often facilitating) nanoscale charge transport, time-tagged single-molecule electroluminescence reveals a significant mechanism for nanoscale charge transport in nanoscale gold break junctions, and offers direct readout of the electrode-molecule interactions that can be correlated with current flow.

Electromigration junction formation is amenable to three terminal device fabrication and, this would allow tuning of the nanodot electronic structure with a gate electrode. As mentioned in previous chapters, electrical measurements in cold electromigration-induced gold break junctions exhibit many-body electron spin correlations (Kondo effect) and coulomb blockade attributed to the *in situ* formed gold nanodots. At cryogenic temperature, these effects should manifest themselves as observable changes in the nanocluster EL with the use of a third gate electrode as reference. Modulation of the gate electrode could also be used to dynamically tune the electrode-molecule coupling and reduce electroluminescence intensity fluctuations. Serving as a convenient source of room-temperature single-photons, one could also imagine a variety of novel uses for metal nanodot EL as an analytic tool. For example,

placement of an absorbing biomolecule between a gold emitter and the detector could, in principle, enable room temperature single-molecule absorbance measurements or very precise spectroscopy with squeezed light.

APPENDIX

IDL Programs


```
Pro sumframes_dat ;turns a 32-bit deep movie.dat file into a tiff readable by iImage
;These parameters must be changed for each file
;-------------------------------------------------------------------------------------
;-------------------------------------------------------------------------------------
;absolute coordinates in pixels
left  = 1
right = 134
bottom= 1
top   = 512

number_of_images = 365
;image_start = 0          ;first image is 0
;image_end=299           ;last image is <number_of_images - 1>
;-------------------------------------------------------------------------------------
;-------------------------------------------------------------------------------------
width = right - left + 1
height = top - bottom + 1
;declarations
images=lonarr(width,height,number_of_images)
filein=strarr(200)
fileout=strarr(200)
total_image = ulon64arr(width, height)
;choose the data file
filein=dialog_pickfile(path='F:\jose\data\', filter='*.dat', title='Open file to be read...')
;open the output file and print header line
fileout=dialog_pickfile(path='F:\data', filter='*.tif', title='Save the output file...')
;open the input data file and read in the 3-D array called "images"
if( filein ne "")then openr,lun,filein,/get_lun
readu,lun,images
free_lun,lun
total_image = total(images, 3, /preserve_type)
write_tiff, fileout, total_image, /long
END

Pro spotbyspot_dat
;reads in and integrates up to 75 spots from a multiframe ixon file exported in 16-bit .dat
format.
;update all parameters in between double dash lines before executing.
```

```
;These parameters must be changed for each file
;-------------------------------------------------------------------------------
;-------------------------------------------------------------------------------
;absolute coordinates in pixels
left  = 131
right = 251
bottom= 1
top   = 512

number_of_images = 151
image_start = 0                                    ;first image is 0
image_end=150                ;last image is <number_of_images - 1>
offset = 1                ;background subtraction in x ("1"), in y ("2"), or off ("0")
;-------------------------------------------------------------------------------
;-------------------------------------------------------------------------------

width = right - left + 1
height = top - bottom + 1

;declarations
images=intarr(width,height,number_of_images)
filein=strarr(200)
fileout=strarr(200)
total_intensity = lon64arr(75)
total_blank = lon64arr(75)
sub_intensity = lon64arr(75)
xarea = long64(0)
yarea = long64(0)
area = long64(0)



;pixel addresses
st=intarr(2,75)
ed=intarr(2,75)
ofst=intarr(75)


;choose the data file
filein[0]=dialog_pickfile(path='F:\data', filter='*.dat', title='Open file to be read...')


;Adjust these pixel addresses to define spot ranges in .dat file
;-------------------------------------------------------------------------------
;-------------------------------------------------------------------------------
```

```
st(0,0)=208             ;x start  (-1 stops the count)
ed(0,0)=214             ;x end
st(1,0)=508             ;y start
ed(1,0)=512             ;y end
ofst(0)=-40             ;shift of spot (in pixels) to calculate background intensity



;-------------------------------------------------------------------------------------
;-------------------------------------------------------------------------------------

number_of_spots = 75                                    ;this counts the number of spots
for iii = 74,0,-1 do begin
if st(0,iii) eq -1 then number_of_spots = iii
endfor

; create the header line
print_string = ""
for i=0, number_of_spots-1 do begin
        ;xarea = fix(ed(0,i)-st(0,i)+1)
        ;yarea = fix(ed(1,i)-st(1,i)+1)
        ;area = fix(xarea*yarea)
        ;print_string = strcompress(print_string + "," + string(fix(area)), /remove_all)
        print_string = strcompress(print_string + "," + "spot" + string(i+1), /remove_all)
endfor


;open the output file and print header line
fileout=dialog_pickfile(path='F:\data', filter='*.dat', title='Save the output file...')
        openw, 1, fileout
        printf,1,print_string


;open the input data file and read in the 3-D array called "images"
if( filein(0) ne "")then openr,lun,filein(0),/get_lun
readu,lun,images
free_lun,lun


;sum the intensity over each frame (one spot at a time) and subtract background if
"offset" option is turned on
        for j=0, number_of_spots-1 do begin
                for k=image_start, image_end do begin
                        for l=st(0,j)-left, ed(0,j)-left do begin
                                for m=st(1,j)-bottom, ed(1,j)-bottom do begin
```

```
                                        total_intensity(j) = total_intensity(j) +
images(l,m,k)
                                        total_blank(j) = (offset ne 0) * (total_blank(j)$
                                        + (offset eq 1)*images((offset eq
1)*(l+ofst(j)),m,k)$
                                        + (offset eq 2)*images(l,(offset eq
2)*(m+ofst(j)),k))
                                        sub_intensity(j) = total_intensity(j) - total_blank(j)
                                endfor
                        endfor
                endfor

                print_string = ""

                for o=0, number_of_spots-1 do begin
                        print_string = strcompress(print_string + "," +
strtrim(string(sub_intensity(o)),2), /remove_all)
                        total_intensity(o)=0
                        total_blank(o)=0
                endfor


                printf,1,print_string
        endfor



free_lun, 1 & close, 1



END

Pro spec_compare

;declare variables
filein = strarr(200)
fileout= strarr(200)

;request input file from user and read it using the read_ascii routine
filein = dialog_pickfile(filter='*.txt', title='Select a tabbed txt file...')
tem=ASCII_TEMPLATE(filein) ;group all spots as field003
excitation = READ_ASCII(filein, TEMPLATE=tem,COUNT=count, HEADER=hdr)

num_fpvs=4
num_spvs=71
```

```
num_spots=123

;create structure array called spots
spot={spectrum:lonarr(num_fpvs,num_spvs),power:dblarr(num_fpvs,num_spvs)}
spots=REPLICATE(spot, num_spots)

;create array of frequencies
if (num_spvs mod 2) then begin
M = (INDGEN(num_spvs)-(num_spvs/2-0.5))
F = M / (num_spvs*0.05)
endif else begin
M = (INDGEN(num_spvs)-(num_spvs/2-1))
F = M / (num_spvs*0.05)
endelse

;reformat the excitation spectrum and compute its power spectrum
for i=0,num_spots-1 do begin
for j=0,num_fpvs-1 do begin
spots[i].spectrum[j,0:num_spvs-1]=excitation.field003[i,j*num_spvs:(j+1)*num_spvs-1]
spots[i].power[j,0:num_spvs-1] = (ABS(FFT(spots[i].spectrum[j,0:num_spvs-1])))
endfor
endfor

;compute the sum of squares array for spot pairs (m,n),m<=n called "dsq"
dsq = dblarr(num_spots,num_spots)
for m=0,num_spots-1 do begin
for n=m,num_spots-1 do begin
dsq[m,n] = total(((alog10(spots[m].power[num_fpvs-1,0:num_spvs-1]))-
(alog10(spots[n].power[num_fpvs-1,0:num_spvs-1])))^2)
endfor
endfor


temp=[[sort(dsq) mod num_spots], [floor(sort(dsq)/num_spots)], [dsq(sort(dsq))]]
dsqsort=dblarr(3,((num_spots^2)-num_spots)/2)
dsqsort=transpose(temp[((num_spots^2-num_spots)/2)+num_spots:(num_spots^2)-1,*])




;print, dsqsort[*,0:99]

;plot the excitation spectra with its power spectrum
;WINDOW, XSIZE=700, YSIZE=700
;!P.MULTI = [2,0,2]
```

```
;for k=0,num_spots-1 do begin
;plot, excitation.field002[0:num_spvs-1],spots[k].spectrum[num_fpvs-1,0:num_spvs-1]
;plot, F,alog10(spots[k].power[num_fpvs-1,0:num_spvs-1])
;wait, 0.2
;endfor

;name and open the output file
;extension = strpos(filein, '.txt', /reverse_search)
;fileout = strmid(filein, 0, extension)+ "_freq.dat"
;openw, 1, fileout

;write the output file
;printf, 1, hdr
;for i=0,  do begin
;    printf,1,
;endfor

;close, 1
;extension = strpos(fileout, '_clean.dat', /reverse_search)
;fileout = strmid(filein, 0, extension)+ "_newphotons.sav"
;save, spots, filename="F:\jose\joseshared\idl programs\spots.sav"


print, "done"
END

Pro framebyframe
;common datain, zin, noise
;common datafiles, fileout
;common params, xm,xp,yp,ym,images, temp,framestart,dimx,dimy
;background=0;0
                        ;background level to be subtracted off
;device, decompose=0
                ;quirk of IDL to display graphs in color...must be typed once per session,
more than that is fine
;loadct, 39
                        ;load color table
;Open the .spe file:


header_size=4100
number_of_scans = 1
number_of_spots = 9
start_image = 0                                         ; first frame = 0
offsetaxis=1                                            ; 0 = x-axis, 1 = y-axis
```

```
hdr=bytarr(header_size)
xarea = long64(0)
yarea = long64(0)
area = long64(0)

filein=dialog_pickfile(filter='*.spe', title='Open data to add...')




openw, 1, 'F:\data\test2.dat'


if( filein ne "")then openr,lun,filein,/get_lun                    ;allow IDL to choose
the logical file unit
readu,lun,hdr

width = hdr(42) + hdr(43)*256
        ;read width info from header
height = hdr(656) + hdr(657)*256                                                    ;read
heigth info from header
number_of_images = hdr(1446) + hdr(1447)*256                        ;read # of
frames info from header

images=intarr(width,height,number_of_images)

                                ;read the file header (to be discarded)
readu,lun,images
                ;read in the images array... change this to images if float array is read in.
free_lun,lun
                ;fre


cross=TOTAL(TOTAL(images,3),2)/(height*number_of_images)

printf,1,string(cross)




close, 1
```

```
END

Pro framebyframe_dat
;reads in and integrates up to 75 spots from a multiframe ixon file exported in 16-bit .dat
format.
;update all parameters in between double dash lines before executing.


;These parameters must be changed for each file
;-------------------------------------------------------------------------------------
;-------------------------------------------------------------------------------------
;absolute coordinates in pixels
left  = 1
right = 134
bottom= 1
top   = 512

number_of_images = 1100
image_start = 0         ;first image is 0
image_end=1091          ;last image is <number_of_images - 1>
offset = 1              ;background subtraction in x ("1"), in y ("2"), or off ("0")
num_frames = 3          ;number of image frames per parameter
;-------------------------------------------------------------------------------------
;-------------------------------------------------------------------------------------
width = right - left + 1
height = top - bottom + 1

;declarations
images=lonarr(width,height,number_of_images)
filein=strarr(200)
fileout=strarr(200)
total_intensity = lon64arr(75)
total_blank = lon64arr(75)
sub_intensity = lon64arr(75)
xarea = long64(0)
yarea = long64(0)
area = long64(0)



;pixel addresses
st=intarr(2,75)
ed=intarr(2,75)
ofst=intarr(75)
```

```
;choose the data file
filein[0]=dialog_pickfile(path='F:\jose\data\', filter='*.dat', title='Open file to be read...')


;Adjust these pixel addresses to define spot ranges in .dat file
;-------------------------------------------------------------------------------------
;-------------------------------------------------------------------------------------
st(0,0)=90   ;x start  (-1 stops the count)
ed(0,0)=101     ;x end
st(1,0)=483     ;y start
ed(1,0)=493     ;y end
ofst(0)=-50     ;shift of spot (in pixels) to calculate background intensity

st(0,1)=93
ed(0,1)=99
st(1,1)=507
ed(1,1)=511
ofst(1)=-50

st(0,2)=95
ed(0,2)=98
st(1,2)=500
ed(1,2)=503
ofst(2)=-50

st(0,3)=89
ed(0,3)=92
st(1,3)=453
ed(1,3)=456
ofst(3)=-50

[more spot addresses…]

;-------------------------------------------------------------------------------------
;-------------------------------------------------------------------------------------

number_of_spots = 75          ;this counts the number of spots
for iii = 74,0,-1 do begin
if st(0,iii) eq -1 then number_of_spots = iii
endfor
print, "number of spots integrating:" + string(number_of_spots)
print, "number of excitation points:" + string((image_end-image_start+1)/num_frames)

; create the header line
print_string = ""
for i=0, number_of_spots-1 do begin
```

```
   ;xarea = fix(ed(0,i)-st(0,i)+1)
   ;yarea = fix(ed(1,i)-st(1,i)+1)
   ;area = fix(xarea*yarea)
   ;print_string = strcompress(print_string + "," + string(fix(area)), /remove_all)
   print_string = strcompress(print_string + "," + "spot" + string(i+1), /remove_all)
endfor


;open the output file and print header line
fileout=dialog_pickfile(path='F:\data', filter='*.dat', title='Save the output file...')
   openw, 1, fileout
   printf,1,print_string


;open the input data file and read in the 3-D array called "images"
if( filein(0) ne "")then openr,lun,filein(0),/get_lun
readu,lun,images
free_lun,lun


;sum the intensity over each spot and subtract background if "offset" option is turned on
   for jj=image_start, image_end-num_frames+1, num_frames do begin

   for j=jj, jj+num_frames-1 do begin
     for k=0, number_of_spots-1 do begin
       for l=st(0,k)-left, ed(0,k)-left do begin
        for m=st(1,k)-bottom, ed(1,k)-bottom do begin
           total_intensity(k) = total_intensity(k) + images(l,m,j)
           total_blank(k) = (offset ne 0) * (total_blank(k)$
           + (offset eq 1)*images((offset eq 1)*(l+ofst(k)),m,j)$
           + (offset eq 2)*images(l,(offset eq 2)*(m+ofst(k)),j))
           sub_intensity(k) = total_intensity(k) - total_blank(k)
        endfor
       endfor
     endfor
   endfor

     print_string = ""

     for o=0, number_of_spots-1 do begin
       print_string = strcompress(print_string + "," + strtrim(string(sub_intensity(o)),2),
/remove_all)
       total_intensity(o)=0
       total_blank(o)=0
     endfor
```

```
    printf,1,print_string
  endfor


free_lun, 1 & close, 1


END

Pro resync

;-----------------modify these parameters yourself--------------------
macro_res = 50                  ;macro time resolution in nsec
micro_res = 0.024414063     ;micro time resolution in nsec
ex_freq = 200.035               ;measured excitation frequency in megahertz
num_periods = 10                ;number of periods desired in resynced window
delay = 930                     ;inter-channel delay in nsec
;generate_histogram = 1       ;1 for true or 0 for false
;-------------------------------------------------------------


macro_res =float(macro_res)
micro_res =float(micro_res)
ex_freq = float(ex_freq)
delay = float(delay)
resync_period = FLOAT(num_periods*1000/ex_freq)          ;in nanoseconds
macro_delay = float(((delay - (delay MOD 50))/macro_res))    ;unitless
micro_delay = float(((delay MOD 50)/micro_res))          ;unitless

;switch to picoseconds
macro_res = macro_res*1000
micro_res = micro_res*1000
resync_period = resync_period*1000

;declare variables
filein = strarr(200)
fileout= strarr(200)

;request input file from user and read it using the read_ascii routine
filein = dialog_pickfile(filter='*.asc', title='Select an ascii file...')
t = SYSTIME(1)
photons = READ_ASCII(filein, COUNT=photons_read, DATA_START=19,
HEADER=hdr)
```

```
;check validity of each photon and sort ch1 from ch2
ch1s = WHERE((photons.field1[3,*] EQ 0) AND (photons.field1[2,*] EQ 0))
ch2s = WHERE((photons.field1[3,*] EQ 0) AND (photons.field1[2,*] EQ 1))
num_ch1s = N_ELEMENTS(ch1s)
num_ch2s = N_ELEMENTS(ch2s)
resynced_size = (num_ch1s GT num_ch2s) ? num_ch1s : num_ch2s

;declare the output time array
resynced= ulon64arr(2,resynced_size)

;calulate absolute photon arrival times, subtract delay from ch2, and resync
resynced[0,*] = ((photons.field1[0,ch1s]*macro_res + photons.field1[1,ch1s]*micro_res)
mod resync_period)
resynced[1,0] = (((photons.field1[0,ch2s]-macro_delay)*macro_res $
                                    + (photons.field1[1,ch2s]-micro_delay)*micro_res) mod
resync_period)

;name and open the output file
extension = strpos(filein, '.asc', /reverse_search)
fileout = strmid(filein, 0, extension)+ "_"+ strtrim(long(delay),2) + "ns_" +
strtrim(ex_freq/num_periods,2) + "MHz.txt"
openw, 1, fileout
printf, 1, hdr
printf, 1, " "
printf, 1, "***All invalid photons were thrown out."
printf, 1, "***An interchannel delay of" + " " + strtrim(long(delay),2) + " "+ "nsec" + " "
+ "was subtracted from CH2."
printf, 1, "***Micro times artificially resynced at"+ " " + strtrim(ex_freq,2)+ " " +
"MHz"+ " " + "every" +" "$
                            + strtrim(num_periods,2) + " " + "periods."
printf, 1, "CH1[ps],CH2[ps]"

;limit indices to 1.5 million per loop
fotons=0
while (resynced_size GT 1500000) do begin
        fotons=fotons+1
        resynced_size = resynced_size - 1500000
endwhile

for j=0, fotons-1 do begin
        for i=0, resynced_size-1 do begin
                printf,1, string(resynced[0,i]) + "," + string(resynced[1,i])
        endfor
endfor
```

```
close, 1

;if (generate_histogram EQ 1) then begin
;bin = 10
;hist = histogram(resynced[0,*], BINSIZE=bin) + histogram(resynced[1,*],
BINSIZE=bin)
;;;plot_info = {plot_info, XAXIS:"picoseconds", YAXIS:"counts per " + strtrim(bin) + "
ps bin"}
;LIVE_PLOT, hist,/HISTOGRAM,XRANGE=[2,resync_period/bin];,
REFERENCE_OUT=plot_info
;endif

print, SYSTIME(1) - t, "seconds."
END


--------------------------------
--------------------------------
Visual Basic programs
--------------------------------
--------------------------------

' ------------------------------------------------------------------------
'  Distributed by VXIplug&play Systems Alliance
'  Do not modify the contents of this file.
' ------------------------------------------------------------------------
'  Title   : VISA32.BAS
'  Date    : 11-04-96
'  Purpose : Include file for the VISA Library 1.1 spec
' ------------------------------------------------------------------------

Global Const VI_SPEC_VERSION = &H100100

' - Resource Template Functions and Operations ----------------------------

Declare Function viOpenDefaultRM Lib "VISA32.DLL" Alias "#141" (sesn As Long)
As Long
Declare Function viGetDefaultRM Lib "VISA32.DLL" Alias "#128" (sesn As Long) As
Long
Declare Function viFindRsrc Lib "VISA32.DLL" Alias "#129" (ByVal sesn As Long,
ByVal expr As String, vi As Long, retCount As Long, ByVal desc As String) As Long
Declare Function viFindNext Lib "VISA32.DLL" Alias "#130" (ByVal vi As Long,
ByVal desc As String) As Long
Declare Function viOpen Lib "VISA32.DLL" Alias "#131" (ByVal sesn As Long, ByVal
viDesc As String, ByVal mode As Long, ByVal timeout As Long, vi As Long) As Long
Declare Function viClose Lib "VISA32.DLL" Alias "#132" (ByVal vi As Long) As Long
```

```
Declare Function viGetAttribute Lib "VISA32.DLL" Alias "#133" (ByVal vi As Long,
ByVal attrName As Long, attrValue As Any) As Long
Declare Function viSetAttribute Lib "VISA32.DLL" Alias "#134" (ByVal vi As Long,
ByVal attrName As Long, ByVal attrValue As Long) As Long
Declare Function viStatusDesc Lib "VISA32.DLL" Alias "#142" (ByVal vi As Long,
ByVal status As Long, ByVal desc As String) As Long
Declare Function viLock Lib "VISA32.DLL" Alias "#144" (ByVal vi As Long, ByVal
lockType As Long, ByVal timeout As Long, ByVal requestedKey As String, ByVal
accessKey As String) As Long
Declare Function viUnlock Lib "VISA32.DLL" Alias "#145" (ByVal vi As Long) As
Long
Declare Function viEnableEvent Lib "VISA32.DLL" Alias "#135" (ByVal vi As Long,
ByVal eventType As Long, ByVal mechanism As Integer, ByVal context As Long) As
Long
Declare Function viDisableEvent Lib "VISA32.DLL" Alias "#136" (ByVal vi As Long,
ByVal eventType As Long, ByVal mechanism As Integer) As Long
Declare Function viDiscardEvents Lib "VISA32.DLL" Alias "#137" (ByVal vi As Long,
ByVal eventType As Long, ByVal mechanism As Integer) As Long
Declare Function viWaitOnEvent Lib "VISA32.DLL" Alias "#138" (ByVal vi As Long,
ByVal inEventType As Long, ByVal timeout As Long, outEventType As Long,
outEventContext As Long) As Long

' - Basic I/O Operations ----------------------------------------------------

Declare Function viRead Lib "VISA32.DLL" Alias "#256" (ByVal vi As Long, ByVal
Buffer As String, ByVal count As Long, retCount As Long) As Long
Declare Function viWrite Lib "VISA32.DLL" Alias "#257" (ByVal vi As Long, ByVal
Buffer As String, ByVal count As Long, retCount As Long) As Long
Declare Function viAssertTrigger Lib "VISA32.DLL" Alias "#258" (ByVal vi As Long,
ByVal protocol As Integer) As Long
Declare Function viReadSTB Lib "VISA32.DLL" Alias "#259" (ByVal vi As Long,
status As Integer) As Long
Declare Function viClear Lib "VISA32.DLL" Alias "#260" (ByVal vi As Long) As Long

' - Formatted I/O Operations -----------------------------------------------

Declare Function viSetBuf Lib "VISA32.DLL" Alias "#267" (ByVal vi As Long, ByVal
mask As Integer, ByVal bufSize As Long) As Long
Declare Function viFlush Lib "VISA32.DLL" Alias "#268" (ByVal vi As Long, ByVal
mask As Integer) As Long
Declare Function viVPrintf Lib "VISA32.DLL" Alias "#270" (ByVal vi As Long, ByVal
writeFmt As String, params As Any) As Long
Declare Function viVScanf Lib "VISA32.DLL" Alias "#272" (ByVal vi As Long, ByVal
readFmt As String, params As Any) As Long
Declare Function viVQueryf Lib "VISA32.DLL" Alias "#280" (ByVal vi As Long,
ByVal writeFmt As String, ByVal readFmt As String, params As Any) As Long
```

```
' - Memory I/O Operations ------------------------------------------------

Declare Function viIn8 Lib "VISA32.DLL" Alias "#273" (ByVal vi As Long, ByVal
accSpace As Integer, ByVal offset As Long, val8 As Byte) As Long
Declare Function viOut8 Lib "VISA32.DLL" Alias "#274" (ByVal vi As Long, ByVal
accSpace As Integer, ByVal offset As Long, ByVal val8 As Byte) As Long
Declare Function viIn16 Lib "VISA32.DLL" Alias "#261" (ByVal vi As Long, ByVal
accSpace As Integer, ByVal offset As Long, val16 As Integer) As Long
Declare Function viOut16 Lib "VISA32.DLL" Alias "#262" (ByVal vi As Long, ByVal
accSpace As Integer, ByVal offset As Long, ByVal val16 As Integer) As Long
Declare Function viIn32 Lib "VISA32.DLL" Alias "#281" (ByVal vi As Long, ByVal
accSpace As Integer, ByVal offset As Long, val32 As Long) As Long
Declare Function viOut32 Lib "VISA32.DLL" Alias "#282" (ByVal vi As Long, ByVal
accSpace As Integer, ByVal offset As Long, ByVal val32 As Long) As Long
Declare Function viMoveIn8 Lib "VISA32.DLL" Alias "#283" (ByVal vi As Long,
ByVal accSpace As Integer, ByVal offset As Long, ByVal length As Long, buf8 As
Byte) As Long
Declare Function viMoveOut8 Lib "VISA32.DLL" Alias "#284" (ByVal vi As Long,
ByVal accSpace As Integer, ByVal offset As Long, ByVal length As Long, buf8 As
Byte) As Long
Declare Function viMoveIn16 Lib "VISA32.DLL" Alias "#285" (ByVal vi As Long,
ByVal accSpace As Integer, ByVal offset As Long, ByVal length As Long, buf16 As
Integer) As Long
Declare Function viMoveOut16 Lib "VISA32.DLL" Alias "#286" (ByVal vi As Long,
ByVal accSpace As Integer, ByVal offset As Long, ByVal length As Long, buf16 As
Integer) As Long
Declare Function viMoveIn32 Lib "VISA32.DLL" Alias "#287" (ByVal vi As Long,
ByVal accSpace As Integer, ByVal offset As Long, ByVal length As Long, buf32 As
Long) As Long
Declare Function viMoveOut32 Lib "VISA32.DLL" Alias "#288" (ByVal vi As Long,
ByVal accSpace As Integer, ByVal offset As Long, ByVal length As Long, buf32 As
Long) As Long
Declare Function viMove Lib "VISA32.DLL" Alias "#200" (ByVal vi As Long, ByVal
srcSpace As Integer, ByVal srcOffset As Long, ByVal srcWidth As Integer, ByVal
destSpace As Integer, ByVal destOffset As Long, ByVal destWidth As Integer, ByVal
srcLength As Long) As Long
Declare Function viMapAddress Lib "VISA32.DLL" Alias "#263" (ByVal vi As Long,
ByVal mapSpace As Integer, ByVal mapOffset As Long, ByVal mapSize As Long,
ByVal accMode As Integer, ByVal suggested As Long, address As Long) As Long
Declare Function viUnmapAddress Lib "VISA32.DLL" Alias "#264" (ByVal vi As
Long) As Long
Declare Sub viPeek8 Lib "VISA32.DLL" Alias "#275" (ByVal vi As Long, ByVal
address As Long, val8 As Byte)
Declare Sub viPoke8 Lib "VISA32.DLL" Alias "#276" (ByVal vi As Long, ByVal
address As Long, ByVal val8 As Byte)
```

```
Declare Sub viPeek16 Lib "VISA32.DLL" Alias "#265" (ByVal vi As Long, ByVal
address As Long, val16 As Integer)
Declare Sub viPoke16 Lib "VISA32.DLL" Alias "#266" (ByVal vi As Long, ByVal
address As Long, ByVal val16 As Integer)
Declare Sub viPeek32 Lib "VISA32.DLL" Alias "#289" (ByVal vi As Long, ByVal
address As Long, val32 As Long)
Declare Sub viPoke32 Lib "VISA32.DLL" Alias "#290" (ByVal vi As Long, ByVal
address As Long, ByVal val32 As Long)

' - Shared Memory Operations ----------------------------------------------

Declare Function viMemAlloc Lib "VISA32.DLL" Alias "#291" (ByVal vi As Long,
ByVal memSize As Long, offset As Long) As Long
Declare Function viMemFree Lib "VISA32.DLL" Alias "#292" (ByVal vi As Long,
ByVal offset As Long) As Long

' - Attributes ------------------------------------------------------------

Global Const VI_ATTR_RSRC_NAME = &HBFFF0002
Global Const VI_ATTR_RSRC_IMPL_VERSION = &H3FFF0003
Global Const VI_ATTR_RSRC_LOCK_STATE = &H3FFF0004
Global Const VI_ATTR_MAX_QUEUE_LENGTH = &H3FFF0005
Global Const VI_ATTR_USER_DATA = &H3FFF0007
Global Const VI_ATTR_FDC_CHNL = &H3FFF000D
Global Const VI_ATTR_FDC_MODE = &H3FFF000F
Global Const VI_ATTR_FDC_GEN_SIGNAL_EN = &H3FFF0011
Global Const VI_ATTR_FDC_USE_PAIR = &H3FFF0013
Global Const VI_ATTR_SEND_END_EN = &H3FFF0016
Global Const VI_ATTR_TERMCHAR = &H3FFF0018
Global Const VI_ATTR_TMO_VALUE = &H3FFF001A
Global Const VI_ATTR_GPIB_READDR_EN = &H3FFF001B
Global Const VI_ATTR_IO_PROT = &H3FFF001C
Global Const VI_ATTR_ASRL_BAUD = &H3FFF0021
Global Const VI_ATTR_ASRL_DATA_BITS = &H3FFF0022
Global Const VI_ATTR_ASRL_PARITY = &H3FFF0023
Global Const VI_ATTR_ASRL_STOP_BITS = &H3FFF0024
Global Const VI_ATTR_ASRL_FLOW_CNTRL = &H3FFF0025
Global Const VI_ATTR_RD_BUF_OPER_MODE = &H3FFF002A
Global Const VI_ATTR_WR_BUF_OPER_MODE = &H3FFF002D
Global Const VI_ATTR_SUPPRESS_END_EN = &H3FFF0036
Global Const VI_ATTR_TERMCHAR_EN = &H3FFF0038
Global Const VI_ATTR_DEST_ACCESS_PRIV = &H3FFF0039
Global Const VI_ATTR_DEST_BYTE_ORDER = &H3FFF003A
Global Const VI_ATTR_SRC_ACCESS_PRIV = &H3FFF003C
Global Const VI_ATTR_SRC_BYTE_ORDER = &H3FFF003D
Global Const VI_ATTR_SRC_INCREMENT = &H3FFF0040
```

```
Global Const VI_ATTR_DEST_INCREMENT = &H3FFF0041
Global Const VI_ATTR_WIN_ACCESS_PRIV = &H3FFF0045
Global Const VI_ATTR_WIN_BYTE_ORDER = &H3FFF0047
Global Const VI_ATTR_CMDR_LA = &H3FFF006B
Global Const VI_ATTR_MAINFRAME_LA = &H3FFF0070
Global Const VI_ATTR_WIN_BASE_ADDR = &H3FFF0098
Global Const VI_ATTR_WIN_SIZE = &H3FFF009A
Global Const VI_ATTR_ASRL_AVAIL_NUM = &H3FFF00AC
Global Const VI_ATTR_MEM_BASE = &H3FFF00AD
Global Const VI_ATTR_ASRL_CTS_STATE = &H3FFF00AE
Global Const VI_ATTR_ASRL_DCD_STATE = &H3FFF00AF
Global Const VI_ATTR_ASRL_DSR_STATE = &H3FFF00B1
Global Const VI_ATTR_ASRL_DTR_STATE = &H3FFF00B2
Global Const VI_ATTR_ASRL_END_IN = &H3FFF00B3
Global Const VI_ATTR_ASRL_END_OUT = &H3FFF00B4
Global Const VI_ATTR_ASRL_RI_STATE = &H3FFF00BF
Global Const VI_ATTR_ASRL_RTS_STATE = &H3FFF00C0
Global Const VI_ATTR_WIN_ACCESS = &H3FFF00C3
Global Const VI_ATTR_RM_SESSION = &H3FFF00C4
Global Const VI_ATTR_VXI_LA = &H3FFF00D5
Global Const VI_ATTR_MANF_ID = &H3FFF00D9
Global Const VI_ATTR_MEM_SIZE = &H3FFF00DD
Global Const VI_ATTR_MEM_SPACE = &H3FFF00DE
Global Const VI_ATTR_MODEL_CODE = &H3FFF00DF
Global Const VI_ATTR_SLOT = &H3FFF00E8
Global Const VI_ATTR_INTF_INST_NAME = &HBFFF00E9
Global Const VI_ATTR_IMMEDIATE_SERV = &H3FFF0100
Global Const VI_ATTR_INTF_PARENT_NUM = &H3FFF0101
Global Const VI_ATTR_RSRC_SPEC_VERSION = &H3FFF0170
Global Const VI_ATTR_INTF_TYPE = &H3FFF0171
Global Const VI_ATTR_GPIB_PRIMARY_ADDR = &H3FFF0172
Global Const VI_ATTR_GPIB_SECONDARY_ADDR = &H3FFF0173
Global Const VI_ATTR_RSRC_MANF_NAME = &HBFFF0174
Global Const VI_ATTR_RSRC_MANF_ID = &H3FFF0175
Global Const VI_ATTR_INTF_NUM = &H3FFF0176
Global Const VI_ATTR_TRIG_ID = &H3FFF0177
Global Const VI_ATTR_GPIB_UNADDR_EN = &H3FFF0184
Global Const VI_ATTR_JOB_ID = &H3FFF4006
Global Const VI_ATTR_EVENT_TYPE = &H3FFF4010
Global Const VI_ATTR_SIGP_STATUS_ID = &H3FFF4011
Global Const VI_ATTR_RECV_TRID_ID = &H3FFF4012
Global Const VI_ATTR_INTR_STATUS_ID = &H3FFF4023
Global Const VI_ATTR_STATUS = &H3FFF4025
Global Const VI_ATTR_RET_COUNT = &H3FFF4026
Global Const VI_ATTR_BUFFER = &H3FFF4027
Global Const VI_ATTR_RECV_INTR_LEVEL = &H3FFF4041
```

```
' - Event Types -------------------------------------------------------

Global Const VI_EVENT_IO_COMPLETION = &H3FFF2009
Global Const VI_EVENT_TRIG = &HBFFF200A
Global Const VI_EVENT_SERVICE_REQ = &H3FFF200B
Global Const VI_EVENT_VXI_SIGP = &H3FFF2020
Global Const VI_EVENT_VXI_VME_INTR = &HBFFF2021

Global Const VI_ALL_ENABLED_EVENTS = &H3FFF7FFF

' - Completion and Error Codes -----------------------------------------

Global Const VI_SUCCESS = &H0&
Global Const VI_SUCCESS_EVENT_EN = &H3FFF0002
Global Const VI_SUCCESS_EVENT_DIS = &H3FFF0003
Global Const VI_SUCCESS_QUEUE_EMPTY = &H3FFF0004
Global Const VI_SUCCESS_TERM_CHAR = &H3FFF0005
Global Const VI_SUCCESS_MAX_CNT = &H3FFF0006
Global Const VI_SUCCESS_DEV_NPRESENT = &H3FFF007D
Global Const VI_SUCCESS_QUEUE_NEMPTY = &H3FFF0080
Global Const VI_SUCCESS_NESTED_SHARED = &H3FFF0099
Global Const VI_SUCCESS_NESTED_EXCLUSIVE = &H3FFF009A
Global Const VI_SUCCESS_SYNC = &H3FFF009B
Global Const VI_WARN_CONFIG_NLOADED = &H3FFF0077
Global Const VI_WARN_NULL_OBJECT = &H3FFF0082
Global Const VI_WARN_NSUP_ATTR_STATE = &H3FFF0084
Global Const VI_WARN_UNKNOWN_STATUS = &H3FFF0085
Global Const VI_WARN_NSUP_BUF = &H3FFF0088

Global Const VI_ERROR_SYSTEM_ERROR = &HBFFF0000
Global Const VI_ERROR_INV_OBJECT = &HBFFF000E
Global Const VI_ERROR_INV_SESSION = &HBFFF000E
Global Const VI_ERROR_RSRC_LOCKED = &HBFFF000F
Global Const VI_ERROR_INV_EXPR = &HBFFF0010
Global Const VI_ERROR_RSRC_NFOUND = &HBFFF0011
Global Const VI_ERROR_INV_RSRC_NAME = &HBFFF0012
Global Const VI_ERROR_INV_ACC_MODE = &HBFFF0013
Global Const VI_ERROR_TMO = &HBFFF0015
Global Const VI_ERROR_CLOSING_FAILED = &HBFFF0016
Global Const VI_ERROR_INV_DEGREE = &HBFFF001B
Global Const VI_ERROR_INV_JOB_ID = &HBFFF001C
Global Const VI_ERROR_NSUP_ATTR = &HBFFF001D
Global Const VI_ERROR_NSUP_ATTR_STATE = &HBFFF001E
Global Const VI_ERROR_ATTR_READONLY = &HBFFF001F
Global Const VI_ERROR_INV_LOCK_TYPE = &HBFFF0020
```

```
Global Const VI_ERROR_INV_ACCESS_KEY = &HBFFF0021
Global Const VI_ERROR_INV_EVENT = &HBFFF0026
Global Const VI_ERROR_INV_MECH = &HBFFF0027
Global Const VI_ERROR_HNDLR_NINSTALLED = &HBFFF0028
Global Const VI_ERROR_INV_HNDLR_REF = &HBFFF0029
Global Const VI_ERROR_INV_CONTEXT = &HBFFF002A
Global Const VI_ERROR_ABORT = &HBFFF0030
Global Const VI_ERROR_RAW_WR_PROT_VIOL = &HBFFF0034
Global Const VI_ERROR_RAW_RD_PROT_VIOL = &HBFFF0035
Global Const VI_ERROR_OUTP_PROT_VIOL = &HBFFF0036
Global Const VI_ERROR_INP_PROT_VIOL = &HBFFF0037
Global Const VI_ERROR_BERR = &HBFFF0038
Global Const VI_ERROR_INV_SETUP = &HBFFF003A
Global Const VI_ERROR_QUEUE_ERROR = &HBFFF003B
Global Const VI_ERROR_ALLOC = &HBFFF003C
Global Const VI_ERROR_INV_MASK = &HBFFF003D
Global Const VI_ERROR_IO = &HBFFF003E
Global Const VI_ERROR_INV_FMT = &HBFFF003F
Global Const VI_ERROR_NSUP_FMT = &HBFFF0041
Global Const VI_ERROR_LINE_IN_USE = &HBFFF0042
Global Const VI_ERROR_SRQ_NOCCURRED = &HBFFF004A
Global Const VI_ERROR_INV_SPACE = &HBFFF004E
Global Const VI_ERROR_INV_OFFSET = &HBFFF0051
Global Const VI_ERROR_INV_WIDTH = &HBFFF0052
Global Const VI_ERROR_NSUP_OFFSET = &HBFFF0054
Global Const VI_ERROR_NSUP_VAR_WIDTH = &HBFFF0055
Global Const VI_ERROR_WINDOW_NMAPPED = &HBFFF0057
Global Const VI_ERROR_NLISTENERS = &HBFFF005F
Global Const VI_ERROR_NCIC = &HBFFF0060
Global Const VI_ERROR_NSUP_OPER = &HBFFF0067
Global Const VI_ERROR_ASRL_PARITY = &HBFFF006A
Global Const VI_ERROR_ASRL_FRAMING = &HBFFF006B
Global Const VI_ERROR_ASRL_OVERRUN = &HBFFF006C
Global Const VI_ERROR_NSUP_ALIGN_OFFSET = &HBFFF0070
Global Const VI_ERROR_USER_BUF = &HBFFF0071
Global Const VI_ERROR_RSRC_BUSY = &HBFFF0072
Global Const VI_ERROR_NSUP_WIDTH = &HBFFF0076
Global Const VI_ERROR_INV_PARAMETER = &HBFFF0078
Global Const VI_ERROR_INV_PROT = &HBFFF0079
Global Const VI_ERROR_INV_SIZE = &HBFFF007B
Global Const VI_ERROR_WINDOW_MAPPED = &HBFFF0080
Global Const VI_ERROR_NIMPL_OPER = &HBFFF0081
Global Const VI_ERROR_INV_LENGTH = &HBFFF0083
Global Const VI_ERROR_SESN_NLOCKED = &HBFFF009C
Global Const VI_ERROR_MEM_NSHARED = &HBFFF009D
```

```
' - Other VISA Definitions ---------------------------------------------

Global Const VI_FIND_BUFLEN = 256

Global Const VI_NULL = 0
Global Const VI_TRUE = 1
Global Const VI_FALSE = 0

Global Const VI_INTF_GPIB = 1
Global Const VI_INTF_VXI = 2
Global Const VI_INTF_GPIB_VXI = 3
Global Const VI_INTF_ASRL = 4

Global Const VI_NORMAL = 1
Global Const VI_FDC = 2
Global Const VI_HS488 = 3
Global Const VI_ASRL488 = 4

Global Const VI_FDC_NORMAL = 1
Global Const VI_FDC_STREAM = 2

Global Const VI_LOCAL_SPACE = 0
Global Const VI_A16_SPACE = 1
Global Const VI_A24_SPACE = 2
Global Const VI_A32_SPACE = 3

Global Const VI_UNKNOWN_LA = -1
Global Const VI_UNKNOWN_SLOT = -1
Global Const VI_UNKNOWN_LEVEL = -1

Global Const VI_QUEUE = 1
Global Const VI_ALL_MECH = &HFFFF

Global Const VI_TRIG_SW = -1
Global Const VI_TRIG_TTL0 = 0
Global Const VI_TRIG_TTL1 = 1
Global Const VI_TRIG_TTL2 = 2
Global Const VI_TRIG_TTL3 = 3
Global Const VI_TRIG_TTL4 = 4
Global Const VI_TRIG_TTL5 = 5
Global Const VI_TRIG_TTL6 = 6
Global Const VI_TRIG_TTL7 = 7
Global Const VI_TRIG_ECL0 = 8
Global Const VI_TRIG_ECL1 = 9

Global Const VI_TRIG_PROT_DEFAULT = 0
```

```
Global Const VI_TRIG_PROT_ON = 1
Global Const VI_TRIG_PROT_OFF = 2
Global Const VI_TRIG_PROT_SYNC = 5

Global Const VI_READ_BUF = 1
Global Const VI_WRITE_BUF = 2
Global Const VI_READ_BUF_DISCARD = 4
Global Const VI_WRITE_BUF_DISCARD = 8
Global Const VI_ASRL_IN_BUF = 16
Global Const VI_ASRL_OUT_BUF = 32
Global Const VI_ASRL_IN_BUF_DISCARD = 64
Global Const VI_ASRL_OUT_BUF_DISCARD = 128

Global Const VI_FLUSH_ON_ACCESS = 1
Global Const VI_FLUSH_WHEN_FULL = 2
Global Const VI_FLUSH_DISABLE = 3

Global Const VI_NMAPPED = 1
Global Const VI_USE_OPERS = 2
Global Const VI_DEREF_ADDR = 3

Global Const VI_TMO_IMMEDIATE = &H0&
Global Const VI_TMO_INFINITE = &HFFFFFFFF
Global Const VI_INFINITE = &HFFFFFFFF

Global Const VI_NO_LOCK = 0
Global Const VI_EXCLUSIVE_LOCK = 1
Global Const VI_SHARED_LOCK = 2
Global Const VI_LOAD_CONFIG = 4

Global Const VI_NO_SEC_ADDR = &HFFFF

Global Const VI_ASRL_PAR_NONE = 0
Global Const VI_ASRL_PAR_ODD = 1
Global Const VI_ASRL_PAR_EVEN = 2
Global Const VI_ASRL_PAR_MARK = 3
Global Const VI_ASRL_PAR_SPACE = 4

Global Const VI_ASRL_STOP_ONE = 10
Global Const VI_ASRL_STOP_TWO = 20

Global Const VI_ASRL_FLOW_NONE = 0
Global Const VI_ASRL_FLOW_XON_XOFF = 1
Global Const VI_ASRL_FLOW_RTS_CTS = 2

Global Const VI_ASRL_END_NONE = 0
```

```
Global Const VI_ASRL_END_LAST_BIT = 1
Global Const VI_ASRL_END_TERMCHAR = 2
Global Const VI_ASRL_END_BREAK = 3

Global Const VI_STATE_ASSERTED = 1
Global Const VI_STATE_UNASSERTED = 0
Global Const VI_STATE_UNKNOWN = -1

Global Const VI_BIG_ENDIAN = 0
Global Const VI_LITTLE_ENDIAN = 1

Global Const VI_DATA_PRIV = 0
Global Const VI_DATA_NPRIV = 1
Global Const VI_PROG_PRIV = 2
Global Const VI_PROG_NPRIV = 3
Global Const VI_BLCK_PRIV = 4
Global Const VI_BLCK_NPRIV = 5
Global Const VI_D64_PRIV = 6
Global Const VI_D64_NPRIV = 7

Global Const VI_WIDTH_8 = 1
Global Const VI_WIDTH_16 = 2
Global Const VI_WIDTH_32 = 4

Global defaultRM As Long
Global ErrorStatus As Long
Global TotalC As Single
Global power_supply, ammeter, hp33120 As Long
Global power_supply_addr, ammeter_addr, hp33120_addr As String
Global discolored As Boolean

Sub discolorit()

' declaration

Dim Threshold, ActualI As Single
Dim I As Long
Dim VolQuery As String
Dim Time_Data_range, Volt_Data_Range, Curr_Data_Range, Coul_Data_Range,
SerName As String
Dim maxvReached, keithley, camera As Boolean
Dim startTime, endTime
Dim ScanN As Long


'definition
```

```
power_supply_addr = LTrim(RTrim(Str(Sheets(1).Cells(11, 12))))
ammeter_addr = LTrim(RTrim(Str(Sheets(1).Cells(12, 12))))
hp33120_addr = LTrim(RTrim(Str(Sheets(1).Cells(13, 12))))

StandingV = Sheets(1).Cells(6, 2)
TimeforOneStep = Sheets(1).Cells(6, 6)
camera_trg = Sheets(1).Cells(9, 6)
Threshold = Sheets(1).Cells(6, 8)

keithley = False
camera = False
If (Sheets(1).Cells(12, 14) = "y" Or Sheets(1).Cells(12, 14) = "Y") Then keithley = True
If (Sheets(1).Cells(12, 15) = "y" Or Sheets(1).Cells(12, 15) = "Y") Then camera = True


'initialize GPIB board
Init_GPIB



'open port for instruments
ErrorStatus = viOpen(defaultRM, "GPIB0::" & power_supply_addr & "::INSTR", 0,
1000, power_supply)
CheckError ByVal power_supply, "Unable to open port E3646A"

If camera Then
ErrorStatus = viOpen(defaultRM, "GPIB0::" & hp33120_addr & "::INSTR", 0, 1000,
hp33120)
CheckError ByVal power_supply, "Unable to open port 33120A"
End If

If keithley Then
ErrorStatus = viOpen(defaultRM, "GPIB0::" & ammeter_addr & "::INSTR", 0, 1000,
ammeter)
CheckError ByVal power_supply, "Unable to open port 485"
End If


'setup external triger for camera (HP33120A function generator)
If camera Then
SendSCPI ByVal hp33120, "TRIG:SOUR BUS"
SendSCPI ByVal hp33120, "TRIG:SLOP NEG"
End If

'setup power supply E3646A
SendSCPI ByVal power_supply, "*RST"
```

```
SendSCPI ByVal power_supply, "INST:NSEL 1"
SendSCPI ByVal power_supply, "VOLT:RANG HIGH"
SendSCPI ByVal power_supply, "VOLT 0.00"
SendSCPI ByVal power_supply, "OUTP ON"

'setup ampere meter (keithley 485A)
If keithley Then
SendSCPI ByVal ammeter, "*RST"
'SendSCPI ByVal ammeter, "CURR:NPLC 2"
SendSCPI ByVal ammeter, "SYST:ZCH ON"
SendSCPI ByVal ammeter, "CURR:RANG 2e-9"
SendSCPI ByVal ammeter, "INIT"
SendSCPI ByVal ammeter, "SYST:ZCOR:ACQ"
SendSCPI ByVal ammeter, "SYST:ZCOR ON"
SendSCPI ByVal ammeter, "CURR:RANG:AUTO ON"
SendSCPI ByVal ammeter, "SYST:ZCH OFF"
End If


'calculate voltage to be set
VolQuery = "VOLT " + Str(StandingV)

'query voltage to power supply (E3646A)
SendSCPI ByVal power_supply, VolQuery

I = -1
discolored = False

Do

I = I + 1

'Read Voltage
If TimeforOneStep >= 0.5 Then Sheets(2).Cells(I + 2, 2) = Val(SendSCPI(ByVal
power_supply, "Meas:Voltage?"))

'Read Current
If keithley Then
Sheets(2).Cells(I + 2, 3) = Val(SendSCPI(ByVal ammeter, "READ?"))
Else
Sheets(2).Cells(I + 2, 3) = Val(SendSCPI(ByVal power_supply, "Meas:Current?"))
End If

'Trigger Camera with HP33120
If (camera And (Int(I / camera_trg) - I / camera_trg) = 0) Then SendSCPI ByVal
hp33120, "*TRG"
```

```
'Measure Cycle Time
If I = 0 Then startTime = Timer
Do
DoEvents
Loop Until (I + 1) * TimeforOneStep < (Timer - startTime)
Sheets(2).Cells(I + 2, 1) = Timer - startTime


'Write Charge Consumption Info
If I > 0 Then
Sheets(2).Cells(I + 2, 4) = Sheets(2).Cells(I + 1, 4) + (Sheets(2).Cells(I + 2, 1) -
Sheets(2).Cells(I + 1, 1)) * Sheets(2).Cells(I + 2, 3)
Else
Sheets(2).Cells(I + 2, 4) = 0
End If

DoEvents
If (Sheets(2).Cells(I + 1, 3) - Sheets(2).Cells(I + 2, 3)) > Threshold Then discolored =
True

Loop Until discolored


'Time & Charge Consumption
   Sheets(1).Cells(12, 6) = Sheets(2).Cells(I + 2, 1)
   Sheets(1).Cells(6, 10) = Sheets(2).Cells(I + 2, 4)

SendSCPI ByVal power_supply, "OUTP OFF"
'If keithley Then SendSCPI ByVal ammeter, "*"

ClosePort ByVal power_supply
ClosePort ByVal hp33120
If keithley Then ClosePort ByVal ammeter

Term_GPIB

End Sub
Private Function Init_GPIB()

ErrorStatus = viOpenDefaultRM(defaultRM)

End Function

Private Function Term_GPIB()
```

```
ErrorStatus = viClose(defaultRM)

End Function

Private Sub OpenPort(ByVal GPIB_Address As String, ByVal instrument As Long)

ErrorStatus = viOpen(defaultRM, "GPIB0::" & GPIB_Address & "::INSTR", 0, 1000,
instrument)
CheckError ByVal instrument, "Unable to open port"

End Sub

Private Function SendSCPI(ByVal instrument As Long, command As String) As String
Dim commandString As String
Dim ReturnString As String
Dim crlfpos As Integer
Dim ReadBuffer As String * 512
Dim actual As Long
commandString = command & Chr$(10)
ErrorStatus = viWrite(instrument, ByVal commandString, Len(commandString), actual)
CheckError ByVal instrument, "Can't write to Device"

   If InStr(commandString, "?") Then
      ErrorStatus = viRead(instrument, ByVal ReadBuffer, 512, actual)
      CheckError ByVal instrument, "Can't Read From Device"
      ReturnString = ReadBuffer
      crlfpos = InStr(ReturnString, Chr$(0))
      If crlfpos Then
         ReturnString = Left(ReturnString, crlfpos - 1)
      End If
      SendSCPI = ReturnString
   End If

End Function

Private Function ClosePort(ByVal instrument As Long)
ErrorStatus = viClose(instrument)
End Function

Private Function CheckError(ByVal instrument As Long, ErrorMessage As String)
If ErrorStatus < VI_SUCCESS Then
   Sheets(1).Cells(6, 12) = ErrorMessage
   ClosePort ByVal instrument
   End
End If
End Function
```

```
Sub ReSet()

Dim I As Integer

Sheets(1).Cells(6, 10) = 0
Sheets(1).Cells(6, 12) = ""
Sheets(1).Cells(12, 6) = 0
Sheets(2).Range("A1:D10000").ClearContents

End Sub
```

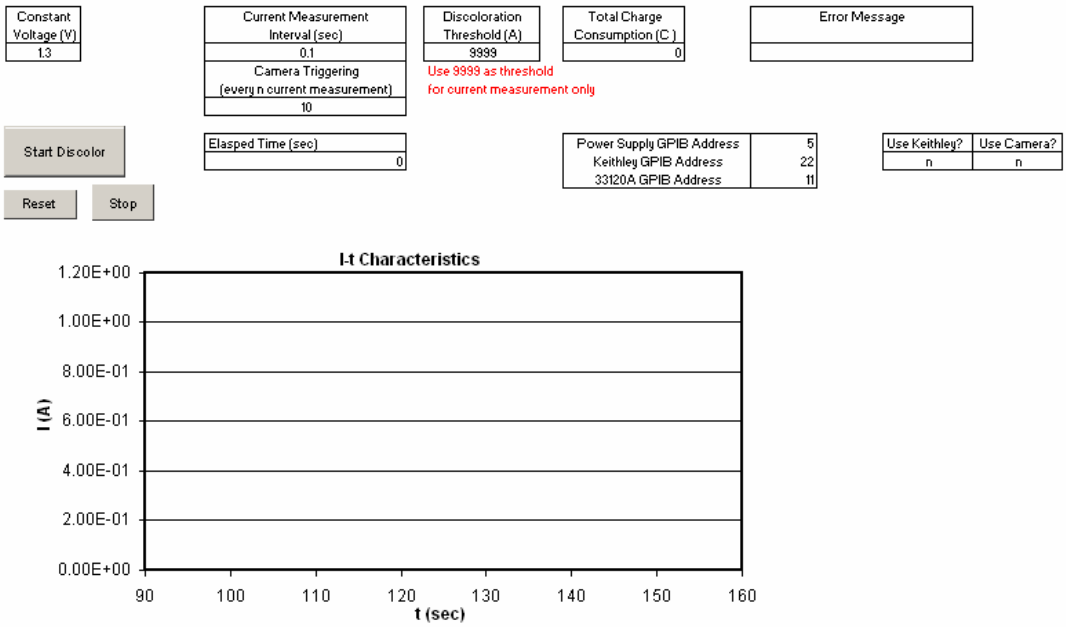
Constant Voltage (V)
1.3
Current Measurement Interval (sec)
0.1
Camera Triggering (every n current measurement)
10
Discoloration Threshold (A)
9999
Use 9999 as threshold for current measurement only
Total Charge Consumption (C)
0
Error Message
Start Discolor
Elasped Time (sec)
0
Power Supply GPIB Address
Keithley GPIB Address
33120A GPIB Address
5
22
11
Use Keithley?
Use Camera?
n
n
Reset
Stop
I-t Characteristics
1.20E+00
1.00E+00
8.00E-01
6.00E-01
4.00E-01
2.00E-01
0.00E+00
I (A)
90
100
110
120
130
140
150
160
t (sec)

```
Sub discolorit()

' declaration

Dim Threshold, ActualI As Single
Dim I As Long
Dim VolQuery As String
Dim Time_Data_range, Volt_Data_Range, Curr_Data_Range, Coul_Data_Range,
SerName As String
Dim maxvReached, keithley, camera As Boolean
Dim startTime, endTime
Dim ScanN As Long


'definition
power_supply_addr = LTrim(RTrim(Str(Sheets(1).Cells(11, 12))))
ammeter_addr = LTrim(RTrim(Str(Sheets(1).Cells(12, 12))))
hp33120_addr = LTrim(RTrim(Str(Sheets(1).Cells(13, 12))))

StandingV = Sheets(1).Cells(6, 2)
TimeforOneStep = Sheets(1).Cells(6, 6)
Triggerframe = Sheets(1).Cells(8, 6)
Threshold = Sheets(1).Cells(6, 8)

keithley = False
camera = False
If (Sheets(1).Cells(12, 14) = "y" Or Sheets(1).Cells(12, 14) = "Y") Then keithley = True
If (Sheets(1).Cells(12, 15) = "y" Or Sheets(1).Cells(12, 15) = "Y") Then camera = True


'initialize GPIB board
Init_GPIB



'open port for instruments
ErrorStatus = viOpen(defaultRM, "GPIB0::" & power_supply_addr & "::INSTR", 0,
1000, power_supply)
CheckError ByVal power_supply, "Unable to open port E3646A"

If camera Then
ErrorStatus = viOpen(defaultRM, "GPIB0::" & hp33120_addr & "::INSTR", 0, 1000,
hp33120)
CheckError ByVal power_supply, "Unable to open port 33120A"
End If
```

```
If keithley Then
ErrorStatus = viOpen(defaultRM, "GPIB0::" & ammeter_addr & "::INSTR", 0, 1000,
ammeter)
CheckError ByVal power_supply, "Unable to open port 485"
End If


'setup external triger for camera (HP33120A function generator)
If camera Then
SendSCPI ByVal hp33120, "TRIG:SOUR BUS"
SendSCPI ByVal hp33120, "TRIG:SLOP NEG"
End If

'setup power supply E3646A
SendSCPI ByVal power_supply, "*RST"
SendSCPI ByVal power_supply, "INST:NSEL 1"
SendSCPI ByVal power_supply, "VOLT:RANG HIGH"
SendSCPI ByVal power_supply, "VOLT 0.00"
SendSCPI ByVal power_supply, "OUTP ON"

'setup ampere meter (keithley 485A)
If keithley Then
SendSCPI ByVal ammeter, "*RST"
'SendSCPI ByVal ammeter, "CURR:NPLC 2"
SendSCPI ByVal ammeter, "SYST:ZCH ON"
SendSCPI ByVal ammeter, "CURR:RANG 2e-9"
SendSCPI ByVal ammeter, "INIT"
SendSCPI ByVal ammeter, "SYST:ZCOR:ACQ"
SendSCPI ByVal ammeter, "SYST:ZCOR ON"
SendSCPI ByVal ammeter, "CURR:RANG:AUTO ON"
SendSCPI ByVal ammeter, "SYST:ZCH OFF"
End If

'calculate voltage to be set
VolQuery = "VOLT " + Str(StandingV)

'query voltage to power supply (E3646A)
SendSCPI ByVal power_supply, VolQuery

I = -1
discolored = False
Frameafterlastpicture = Triggerframe

Do
```

```
I = I + 1

'Read Voltage
Sheets(2).Cells(I + 2, 2) = Val(SendSCPI(ByVal power_supply, "Meas:Voltage?"))

'Read Current
If keithley Then
Sheets(2).Cells(I + 2, 3) = Val(SendSCPI(ByVal ammeter, "READ?"))
Else
Sheets(2).Cells(I + 2, 3) = Val(SendSCPI(ByVal power_supply, "Meas:Current?"))
End If

'Trigger Camera with HP33120
If camera Then
If Frameafterlastpicture = Triggerframe Then
SendSCPI ByVal hp33120, "*TRG"
Frameafterlastpicture = 0
End If
End If
Frameafterlastpicture = Frameafterlastpicture + 1


'Measure Cycle Time
If I = 0 Then startTime = Timer
Do
Loop Until (I + 1) * TimeforOneStep < (Timer - startTime)
Sheets(2).Cells(I + 2, 1) = Timer - startTime


'Write Charge Consumption Info
If I > 0 Then
Sheets(2).Cells(I + 2, 4) = Sheets(2).Cells(I + 1, 4) + (Sheets(2).Cells(I + 2, 1) -
Sheets(2).Cells(I + 1, 1)) * Sheets(2).Cells(I + 2, 3)
Else
Sheets(2).Cells(I + 2, 4) = 0
End If

If (Sheets(2).Cells(I + 1, 3) - Sheets(2).Cells(I + 2, 3)) > Threshold Then discolored =
True

Loop Until discolored


'Time & Charge Consumption
   Sheets(1).Cells(12, 6) = Sheets(2).Cells(I + 2, 1)
   Sheets(1).Cells(6, 10) = Sheets(2).Cells(I + 2, 4)
```

```
SendSCPI ByVal power_supply, "OUTP OFF"
If keithley Then SendSCPI ByVal ammeter, "*"

ClosePort ByVal power_supply
ClosePort ByVal hp33120
If keithley Then ClosePort ByVal ammeter

Term_GPIB

End Sub
Private Function Init_GPIB()

ErrorStatus = viOpenDefaultRM(defaultRM)

End Function

Private Function Term_GPIB()

ErrorStatus = viClose(defaultRM)

End Function

Private Sub OpenPort(ByVal GPIB_Address As String, ByVal instrument As Long)

ErrorStatus = viOpen(defaultRM, "GPIB0::" & GPIB_Address & "::INSTR", 0, 1000,
instrument)
CheckError ByVal instrument, "Unable to open port"

End Sub

Private Function SendSCPI(ByVal instrument As Long, command As String) As String
Dim commandString As String
Dim ReturnString As String
Dim crlfpos As Integer
Dim ReadBuffer As String * 512
Dim actual As Long
commandString = command & Chr$(10)
ErrorStatus = viWrite(instrument, ByVal commandString, Len(commandString), actual)
CheckError ByVal instrument, "Can't write to Device"

   If InStr(commandString, "?") Then
      ErrorStatus = viRead(instrument, ByVal ReadBuffer, 512, actual)
      CheckError ByVal instrument, "Can't Read From Device"
      ReturnString = ReadBuffer
      crlfpos = InStr(ReturnString, Chr$(0))
```

```
        If crlfpos Then
            ReturnString = Left(ReturnString, crlfpos - 1)
        End If
        SendSCPI = ReturnString
    End If

End Function

Private Function ClosePort(ByVal instrument As Long)
ErrorStatus = viClose(instrument)
End Function

Private Function CheckError(ByVal instrument As Long, ErrorMessage As String)
If ErrorStatus < VI_SUCCESS Then
    Sheets(1).Cells(6, 12) = ErrorMessage
    ClosePort ByVal instrument
    End
End If
End Function

Sub ReSet()

Dim I As Integer

Sheets(1).Cells(6, 10) = 0
Sheets(1).Cells(6, 12) = ""
Sheets(1).Cells(12, 6) = 0
Sheets(2).Range("A1:IV1000").ClearContents

End Sub

---------------------------------------------------------------------


Sub poweron()

' declaration

Dim Voltage As Single
Dim ZOS300, ZOS150 As Boolean
Dim VolQuery As String

ZOS300 = False
ZOS150 = False

If Sheets(1).OptionButton1.Value = True Then ZOS300 = True
```

```
If Sheets(1).OptionButton2.Value = True Then ZOS150 = True



If ((Sheets(1).Cells(10, 4) > 0.9) And (Sheets(1).Cells(10, 4) < 16.1)) Then

Power_on = True
Sheets(1).Cells(14, 6) = ""


'Voltage = 0
Voltage = Sheets(1).Cells(10, 4)
'If ZOS300 Then Voltage = -0.000002 * Fq ^ 3 + 0.0007 * Fq ^ 2 + 0.0643 * Fq - 17.372
'If ZOS150 Then Voltage = 0.157 * Fq - 9.937
VolQuery = "VOLT " + LTrim(RTrim(Str(Voltage)))

'channel 2
SendSCPI ByVal power_supply, "INST:NSEL 2"
SendSCPI ByVal power_supply, "VOLT 12.00"
SendSCPI ByVal power_supply, "OUTP ON"
'channel 1
SendSCPI ByVal power_supply, "INST:NSEL 1"
SendSCPI ByVal power_supply, VolQuery
SendSCPI ByVal power_supply, "OUTP ON"

V1 = Val(SendSCPI(ByVal power_supply, "Meas:Voltage?"))
If ZOS300 Then V2 = (-1318.2 * V1 ^ 4 + 44172 * V1 ^ 3 - 240196 * V1 ^ 2 +
10000000 * V1 + 100000000) / 1000000
If ZOS150 Then V2 = 6.3689 * V1 + 63.288

'actual frequncy
Sheets(1).Cells(14, 4) = V2
'actual voltage
Sheets(1).Cells(16, 4) = V1

Else
Sheets(1).Cells(14, 6) = "Frequency Out of Range"

End If

End Sub
Sub poweroff()

If Power_on Then
Power_on = False
```

```
'channel 2
SendSCPI ByVal power_supply, "INST:NSEL 1"
SendSCPI ByVal power_supply, "VOLT 0.00"
SendSCPI ByVal power_supply, "OUTP OFF"
'channel 1
SendSCPI ByVal power_supply, "INST:NSEL 2"
SendSCPI ByVal power_supply, "VOLT 0.00"
SendSCPI ByVal power_supply, "OUTP OFF"

V1 = Val(SendSCPI(ByVal power_supply, "Meas:Voltage?"))
If ZOS300 Then V2 = 1 / (7E-16 * V1 ^ 6 - 0.00000000000004 * V1 ^ 5 +
0.0000000000008 * V1 ^ 4 _
- 0.000000000007 * V1 ^ 3 + 0.00000000003 * V1 ^ 2 - 0.0000000003 * V1 +
0.000000007) / 1000000
If ZOS150 Then V2 = 6.3689 * V1 + 63.288

Sheets(1).Cells(14, 4) = V2
Sheets(1).Cells(16, 4) = V1

End If

End Sub

Sub initialize()

'definition
power_supply_addr = LTrim(RTrim(Str(Sheets(1).TextBox2.Value)))


'initialize GPIB board
Init_GPIB


'open port for instruments
ErrorStatus = viOpen(defaultRM, "GPIB0::" & power_supply_addr & "::INSTR", 0,
1000, power_supply)
CheckError ByVal power_supply, "Unable to open port E3646A"

'setup power supply E3646A
SendSCPI ByVal power_supply, "*RST"
'channel 2
SendSCPI ByVal power_supply, "INST:NSEL 2"
SendSCPI ByVal power_supply, "VOLT:RANG HIGH"
SendSCPI ByVal power_supply, "VOLT 0.00"
SendSCPI ByVal power_supply, "OUTP OFF"
'channel 1
```

```
SendSCPI ByVal power_supply, "INST:NSEL 1"
SendSCPI ByVal power_supply, "VOLT:RANG HIGH"
SendSCPI ByVal power_supply, "VOLT 0.00"
SendSCPI ByVal power_supply, "OUTP OFF"

Sheets(1).CommandButton1.Enabled = True
Sheets(1).CommandButton2.Enabled = True
Sheets(1).Cells(14, 6) = ""

End Sub
Sub ReSet()

Sheets(1).Cells(14, 6) = ""
Sheets(1).Cells(16, 4) = ""
Sheets(1).Cells(14, 4) = ""

End Sub
Private Function Init_GPIB()

ErrorStatus = viOpenDefaultRM(defaultRM)

End Function

Private Function Term_GPIB()

ErrorStatus = viClose(defaultRM)

End Function

Private Sub OpenPort(ByVal GPIB_Address As String, ByVal instrument As Long)

ErrorStatus = viOpen(defaultRM, "GPIB0::" & GPIB_Address & "::INSTR", 0, 1000,
instrument)
CheckError ByVal instrument, "Unable to open port"

End Sub

Private Function SendSCPI(ByVal instrument As Long, command As String) As String
Dim commandString As String
Dim ReturnString As String
Dim crlfpos As Integer
Dim ReadBuffer As String * 512
Dim actual As Long
commandString = command & Chr$(10)
ErrorStatus = viWrite(instrument, ByVal commandString, Len(commandString), actual)
CheckError ByVal instrument, "Can't write to Device"
```

```
    If InStr(commandString, "?") Then
        ErrorStatus = viRead(instrument, ByVal ReadBuffer, 512, actual)
        CheckError ByVal instrument, "Can't Read From Device"
        ReturnString = ReadBuffer
        crlfpos = InStr(ReturnString, Chr$(0))
        If crlfpos Then
            ReturnString = Left(ReturnString, crlfpos - 1)
        End If
        SendSCPI = ReturnString
    End If

End Function

Private Function ClosePort(ByVal instrument As Long)
ErrorStatus = viClose(instrument)
End Function

Private Function CheckError(ByVal instrument As Long, ErrorMessage As String)
If ErrorStatus < VI_SUCCESS Then
    Sheets(1).Cells(14, 6) = ErrorMessage
    ClosePort ByVal instrument
    End
End If
End Function
```

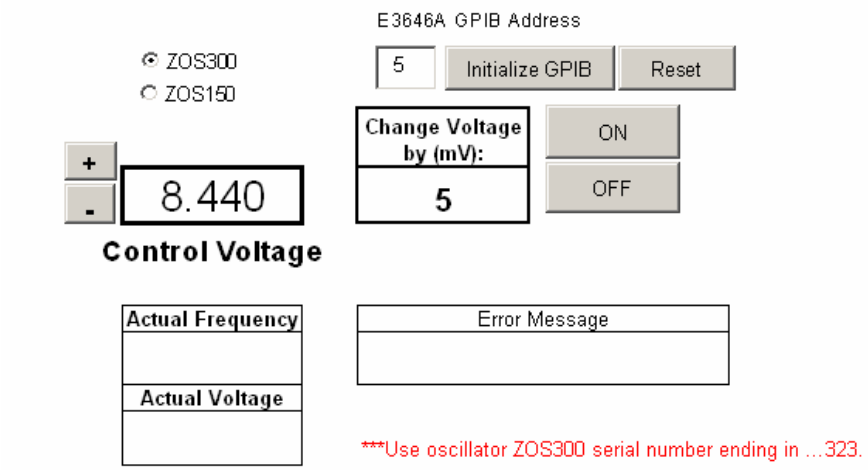
E3646A GPIB Address
ZOS300
ZOS150
5
Initialize GPIB
Reset
Change Voltage by (mV):
5
ON
OFF
+
-
8.440
Control Voltage
Actual Frequency
Actual Voltage
Error Message
***Use oscillator ZOS300 serial number ending in ...323.

```
---------------------------------------------------------------------------------


Sub discolorit()

' declaration

Dim FrameInt As Single
Dim endTime
Dim FrameN, recordlength As Integer
Dim fs, f, ts, s
Dim filestring As String

' definition
datron2000_addr = LTrim(RTrim(Str(Sheets(1).Cells(17, 8))))
hp33120_addr = LTrim(RTrim(Str(Sheets(1).Cells(18, 8))))
'tds5000b_addr = LTrim(RTrim(Str(Sheets(1).Cells(16, 8))))

' pulse repetion period
repperiod = LTrim(RTrim(Sheets(1).Cells(2, 6))) + "n"

' first pulse range and resolution
fpwmin = Sheets(1).Cells(6, 2)
fpwmax = Sheets(1).Cells(6, 4)
fpwres = Sheets(1).Cells(6, 6)
fpamplow = LTrim(RTrim(Sheets(1).Cells(6, 8))) + "m"
fpamphigh = LTrim(RTrim(Sheets(1).Cells(6, 10))) + "m"

' second pulse range and resolution
spwmin = Sheets(1).Cells(10, 2)
spwmax = Sheets(1).Cells(10, 4)
spwres = Sheets(1).Cells(10, 6)
spamplow = LTrim(RTrim(Sheets(1).Cells(10, 8))) + "m"
spamphigh = LTrim(RTrim(Sheets(1).Cells(10, 10))) + "m"

' delay between pulses maximum and resolution
delaymax = Sheets(1).Cells(14, 4)
delayres = Sheets(1).Cells(14, 6)

' camera setting
FrameN = Sheets(1).Cells(6, 12)
FrameInt = (Sheets(1).Cells(6, 14) + 500) / 1000



' initialize GPIB board
```

```
Init_GPIB

'open port for instruments
ErrorStatus = viOpen(defaultRM, "GPIB0::" & datron2000_addr & "::INSTR", 0, 1000,
datron2000)
CheckError ByVal datron2000, "Unable to open port Datron2000"

ErrorStatus = viOpen(defaultRM, "GPIB0::" & hp33120_addr & "::INSTR", 0, 1000,
hp33120)
CheckError ByVal hp33120, "Unable to open port 33120A"

'ErrorStatus = viOpen(defaultRM, "GPIB0::" & tds5000b_addr & "::INSTR", 0, 1000,
tds5000b)
'CheckError ByVal tds5000b, "Unable to open port Tek Scope"


'initialize pulser
SendSCPI ByVal datron2000, "*RST"
SendSCPI ByVal datron2000, "EXTTRIG:OFF"
SendSCPI ByVal datron2000, "INTTRIG:ON"
SendSCPI ByVal datron2000, "PER:" + LTrim(RTrim(Sheets(1).Cells(2, 6))) + "n"
SendSCPI ByVal datron2000, "CHTRIG:OFF,1"
SendSCPI ByVal datron2000, "CHTRIG:OFF,2"
SendSCPI ByVal datron2000, "DBL:OFF,1"
SendSCPI ByVal datron2000, "DBL:OFF,2"
'channel 1 initilization
SendSCPI ByVal datron2000, "CH:1"
SendSCPI ByVal datron2000, "DLY:2.0n"
SendSCPI ByVal datron2000, "WID:2.0n"
SendSCPI ByVal datron2000, "LED:1.0ns"
SendSCPI ByVal datron2000, "TED:1.0ns"
SendSCPI ByVal datron2000, "VLO:0"
SendSCPI ByVal datron2000, "VHI:0"
SendSCPI ByVal datron2000, "INV:OFF"
If Sheets(1).Cells(2, 2) = "n" Or Sheets(1).Cells(2, 2) = "N" Then SendSCPI ByVal
datron2000, "INV:ON"
'channel 2 initilization
SendSCPI ByVal datron2000, "CH:2"
SendSCPI ByVal datron2000, "DLY:2.0n"
SendSCPI ByVal datron2000, "WID:2.0n"
SendSCPI ByVal datron2000, "LED:1.0ns"
SendSCPI ByVal datron2000, "TED:1.0ns"
SendSCPI ByVal datron2000, "VLO:0"
SendSCPI ByVal datron2000, "VHI:0"
SendSCPI ByVal datron2000, "INV:OFF"
```

```
If Sheets(1).Cells(2, 4) = "n" Or Sheets(1).Cells(2, 4) = "N" Then SendSCPI ByVal
datron2000, "INV:ON"

'initialize scope
'recordlength = Sheets(1).Cells(11, 14)
'SendSCPI ByVal tds5000b, "DAT:SOU CH1"
'SendSCPI ByVal tds5000b, "DAT:ENG ASCI"
'SendSCPI ByVal tds5000b, "WFMO:BYT_N 2"
'SendSCPI ByVal tds5000b, "DAT SNA"
'SendSCPI ByVal tds5000b, "DAT:STAR 1"
'SendSCPI ByVal tds5000b, "DAT:STOP" + recordlength

'start scanning
SendSCPI ByVal datron2000, "VLO:" + fpamplow + ",1"
SendSCPI ByVal datron2000, "VHI:" + fpamphigh + ",1"
SendSCPI ByVal datron2000, "VLO:" + spamplow + ",2"
SendSCPI ByVal datron2000, "VHI:" + spamphigh + ",2"

'Create a file for scope waveforms
'filestring = Sheets(1).Cells(18, 12)
'Set fs = CreateObject("Scripting.FileSystemObject")
'fs.CreateTextFile filestring
'Set f = fs.GetFile(filestring)
'Set ts = f.OpenAsTextStream(3, 0)

m = 1
aaa = 0
For I = fpwmin To fpwmax Step fpwres
fpw_cmd = "WID:" + LTrim(RTrim(Str(I))) + "n"
SendSCPI ByVal datron2000, "CH:1"
SendSCPI ByVal datron2000, "WID:" + LTrim(RTrim(Str(I))) + "n"

For j = spwmin To spwmax Step spwres
spw_cmd = "WID:" + LTrim(RTrim(Str(j))) + "n"
SendSCPI ByVal datron2000, "CH:2"
SendSCPI ByVal datron2000, "WID:" + LTrim(RTrim(Str(j))) + "n"

If delaymax >= (I + j) / 2 Then
Delay = delaymax + (I - j) / 2 + 3.2
delay_cmd = "DLY:" + LTrim(RTrim(Str(Delay))) + "n"
SendSCPI ByVal datron2000, "DLY:" + LTrim(RTrim(Str(Delay))) + "n"


Sheets(1).Cells(24, 6) = I
Sheets(1).Cells(25, 6) = j
'counter
```

```
aaa = aaa + 1
Sheets(1).Cells(27, 6) = aaa

'Read & record Data from Datron
m = m + 1
Sheets(2).Cells(m, 1) = Val(SendSCPI(ByVal datron2000, "WID?:1"))
Sheets(2).Cells(m, 2) = Val(SendSCPI(ByVal datron2000, "WID?:2"))
Sheets(2).Cells(m, 3) = Val(SendSCPI(ByVal datron2000, "DLY?:2"))
Sheets(2).Cells(m, 4) = Val(SendSCPI(ByVal datron2000, "VHI?:1"))
Sheets(2).Cells(m, 5) = Val(SendSCPI(ByVal datron2000, "VLO?:1"))
Sheets(2).Cells(m, 6) = SendSCPI(ByVal datron2000, "INV?:1")
Sheets(2).Cells(m, 7) = Val(SendSCPI(ByVal datron2000, "VHI?:2"))
Sheets(2).Cells(m, 8) = Val(SendSCPI(ByVal datron2000, "VLO?:2"))
Sheets(2).Cells(m, 9) = SendSCPI(ByVal datron2000, "INV?:2")
Sheets(2).Cells(m, 10) = Val(SendSCPI(ByVal datron2000, "PER?"))

'call waveform from Tek scope tds5000b
'Sheets(3).Cells(m, 1) = Val(SendSCPI(ByVal tds5000b, "WFMOutpre?"))
'ts.Write SendSCPI(ByVal tds5000b, "CURV?")
'endTime2 = Timer + 1    'allows extra time (sec) for waveform transfer
'Do                      'scope cannot be called until each transfer is finished
'Loop Until endTime2 <= Timer


'Trigger Camera with HP33120
For l = 1 To FrameN
SendSCPI ByVal hp33120, "*TRG"
endTime = Timer + FrameInt
DoEvents
Do
Loop Until endTime <= Timer
Next l

End If

Next j
Next I

'ts.Close
SendSCPI ByVal datron2000, "ZEROCHAN:1"
SendSCPI ByVal datron2000, "ZEROCHAN:2"

ClosePort ByVal datron2000
ClosePort ByVal hp33120
'ClosePort ByVal tds5000b
```

```
Term_GPIB

End Sub
Private Function Init_GPIB()

ErrorStatus = viOpenDefaultRM(defaultRM)

End Function

Private Function Term_GPIB()

ErrorStatus = viClose(defaultRM)

End Function

Private Sub OpenPort(ByVal GPIB_Address As String, ByVal instrument As Long)

ErrorStatus = viOpen(defaultRM, "GPIB0::" & GPIB_Address & "::INSTR", 0, 1000,
instrument)
CheckError ByVal instrument, "Unable to open port"

End Sub

Private Function SendSCPI(ByVal instrument As Long, command As String) As String
Dim commandString As String
Dim ReturnString As String
Dim crlfpos As Integer
Dim ReadBuffer As String * 512
Dim actual As Long
commandString = command & Chr$(10)
ErrorStatus = viWrite(instrument, ByVal commandString, Len(commandString), actual)
CheckError ByVal instrument, "Can't write to Device"

   If InStr(commandString, "?") Then
      ErrorStatus = viRead(instrument, ByVal ReadBuffer, 512, actual)
      CheckError ByVal instrument, "Can't Read From Device"
      ReturnString = ReadBuffer
      crlfpos = InStr(ReturnString, Chr$(0))
      If crlfpos Then
         ReturnString = Left(ReturnString, crlfpos - 1)
      End If
      SendSCPI = ReturnString
   End If

End Function
```

```
Private Function ClosePort(ByVal instrument As Long)
ErrorStatus = viClose(instrument)
End Function

Private Function CheckError(ByVal instrument As Long, ErrorMessage As String)
If ErrorStatus < VI_SUCCESS Then
   Sheets(1).Cells(21, 6) = ErrorMessage
   ClosePort ByVal instrument
   End
End If
End Function

Sub ReSet()

Dim I As Integer

Sheets(1).Cells(21, 6) = ""
Sheets(2).Range("A2:IV1000").ClearContents
'Sheets(3).Range("A1:IV1000").ClearContents
End Sub
```

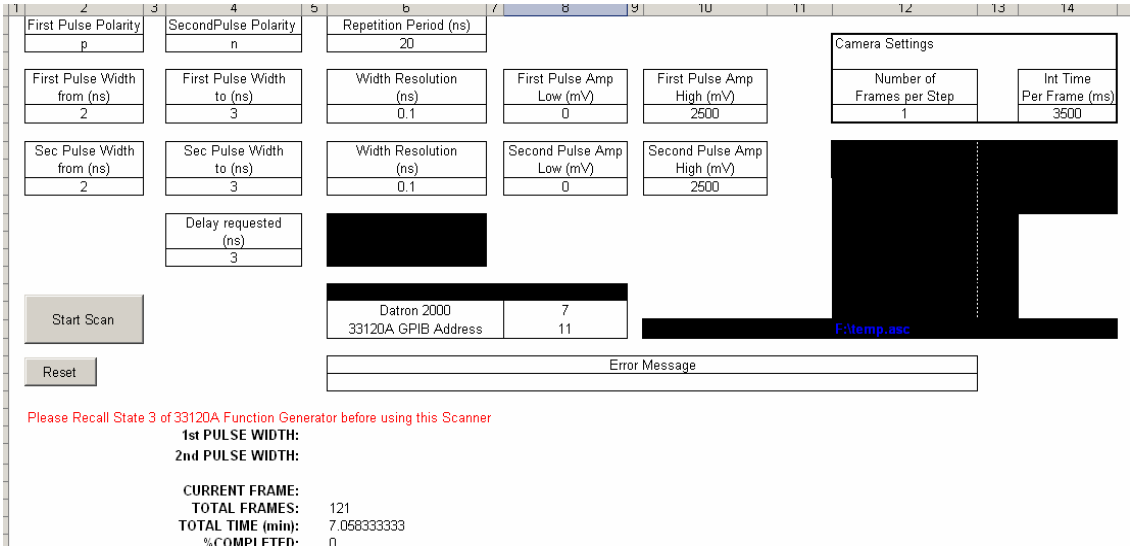
First Pulse Polarity
p
SecondPulse Polarity
n
Repetition Period (ns)
20
Camera Settings
First Pulse Width from (ns)
2
First Pulse Width to (ns)
3
Width Resolution (ns)
0.1
First Pulse Amp Low (mV)
0
First Pulse Amp High (mV)
2500
Number of Frames per Step
1
Int Time Per Frame (ms)
3500
Sec Pulse Width from (ns)
2
Sec Pulse Width to (ns)
3
Width Resolution (ns)
0.1
Second Pulse Amp Low (mV)
0
Second Pulse Amp High (mV)
2500
Delay requested (ns)
3
Start Scan
Datron 2000
33120A GPIB Address
7
11
F:\temp.asc
Reset
Error Message
Please Recall State 3 of 33120A Function Generator before using this Scanner
1st PULSE WIDTH:
2nd PULSE WIDTH:
CURRENT FRAME:
TOTAL FRAMES: 121
TOTAL TIME (min): 7.058333333
%COMPLETED: 0

```
--------------------------------------------------------------------------
Sub doit()

' declaration

Dim FrameInt As Single
Dim endTime
Dim FrameN As Integer

' definition
datron2000_addr = LTrim(RTrim(Str(Sheets(1).Cells(17, 8))))
hp33120_addr = LTrim(RTrim(Str(Sheets(1).Cells(18, 8))))
If Sheets(1).Cells(9, 12) = "y" Or Sheets(1).Cells(9, 12) = "Y" Then tekscope_addr =
LTrim(RTrim(Str(Sheets(1).Cells(16, 8))))


' pulse repetion period
repperiod = LTrim(RTrim(Sheets(1).Cells(2, 6))) + "n"

' first pulse range and resolution
fphmin = Sheets(1).Cells(6, 2)
fphmax = Sheets(1).Cells(6, 4)
fphres = Sheets(1).Cells(6, 6)
fpw = LTrim(RTrim(Sheets(1).Cells(6, 10)))

' second pulse range and resolution
sphmin = Sheets(1).Cells(10, 2)
sphmax = Sheets(1).Cells(10, 4)
sphres = Sheets(1).Cells(10, 6)
spw = LTrim(RTrim(Sheets(1).Cells(10, 10)))

' delay between pulses maximum and resolution
delayreq = Sheets(1).Cells(14, 4)
delay = delayreq + (fpw - spw) / 2 + 3.2
If Sheets(1).Cells(2, 2) = Sheets(1).Cells(2, 4) Then delay = delay + fpw / 2
' camera setting
FrameN = Sheets(1).Cells(6, 12)
FrameInt = (Sheets(1).Cells(6, 14) + 500) / 1000



' initialize GPIB board
Init_GPIB

'open port for instruments
```

```
ErrorStatus = viOpen(defaultRM, "GPIB0::" & datron2000_addr & "::INSTR", 0, 1000,
datron2000)
CheckError ByVal datron2000, "Unable to open port Datron2000"

ErrorStatus = viOpen(defaultRM, "GPIB0::" & hp33120_addr & "::INSTR", 0, 1000,
hp33120)
CheckError ByVal datron2000, "Unable to open port 33120A"

If Sheets(1).Cells(9, 12) = "y" Or Sheets(1).Cells(9, 12) = "Y" Then
ErrorStatus = viOpen(defaultRM, "GPIB0::" & tekscope_addr & "::INSTR", 0, 1000,
tekscope)
CheckError ByVal tekscope, "Unable to open port for tekscope"

'initialize tekscope
SendSCPI ByVal tekscope, "*RCL 4"
SendSCPI ByVal tekscope, "CH1:BAN FUL"
SendSCPI ByVal tekscope, "ACQ:MOD AVE 128"
SendSCPI ByVal tekscope, "SAV:WAVE:FILEF SPREADSHEETT"
End If

'initialize pulser
SendSCPI ByVal datron2000, "*RST"
SendSCPI ByVal datron2000, "EXTTRIG:OFF"
SendSCPI ByVal datron2000, "INTTRIG:ON"
SendSCPI ByVal datron2000, "PER:" + LTrim(RTrim(Sheets(1).Cells(2, 6))) + "n"
SendSCPI ByVal datron2000, "CHTRIG:OFF,1"
SendSCPI ByVal datron2000, "CHTRIG:OFF,2"
SendSCPI ByVal datron2000, "DBL:OFF,1"
SendSCPI ByVal datron2000, "DBL:OFF,2"
'channel 1 initilization
SendSCPI ByVal datron2000, "CH:1"
SendSCPI ByVal datron2000, "DLY:2.0n"
SendSCPI ByVal datron2000, "WID:" + LTrim(RTrim(Str(fpw))) + "n"
SendSCPI ByVal datron2000, "LED:1.0n"
SendSCPI ByVal datron2000, "TED:1.0n"
SendSCPI ByVal datron2000, "VLO:0m"
SendSCPI ByVal datron2000, "VHI:0m"
SendSCPI ByVal datron2000, "INV:OFF"
If Sheets(1).Cells(2, 2) = "n" Or Sheets(1).Cells(2, 2) = "N" Then SendSCPI ByVal
datron2000, "INV:ON"
'channel 2 initilization
SendSCPI ByVal datron2000, "CH:2"
SendSCPI ByVal datron2000, "DLY:" + LTrim(RTrim(Str(delay))) + "n"
SendSCPI ByVal datron2000, "WID:" + LTrim(RTrim(Str(spw))) + "n"
SendSCPI ByVal datron2000, "LED:1.0n"
SendSCPI ByVal datron2000, "TED:1.0n"
```

```
SendSCPI ByVal datron2000, "VLO:0m"
SendSCPI ByVal datron2000, "VHI:0m"
SendSCPI ByVal datron2000, "INV:OFF"
If Sheets(1).Cells(2, 4) = "n" Or Sheets(1).Cells(2, 4) = "N" Then SendSCPI ByVal
datron2000, "INV:ON"

stopit = False

m = 1

For I = fphmin To fphmax Step fphres

SendSCPI ByVal datron2000, "CH:1"
If Sheets(1).Cells(2, 2) = "n" Or Sheets(1).Cells(2, 2) = "N" Then
SendSCPI ByVal datron2000, "VLO:-" + LTrim(RTrim(Str(I))) + "V"
Else
SendSCPI ByVal datron2000, "VHI:" + LTrim(RTrim(Str(I))) + "V"
End If

For j = sphmin To sphmax Step sphres

SendSCPI ByVal datron2000, "CH:2"
If Sheets(1).Cells(2, 4) = "n" Or Sheets(1).Cells(2, 4) = "N" Then
SendSCPI ByVal datron2000, "VLO:-" + LTrim(RTrim(Str(j))) + "V"
Else
SendSCPI ByVal datron2000, "VHI:" + LTrim(RTrim(Str(j))) + "V"
End If

'Read & record Data
Sheets(1).Cells(28, 6) = I
Sheets(1).Cells(29, 6) = j
m = m + 1
Sheets(2).Cells(m, 1) = Val(SendSCPI(ByVal datron2000, "WID?:1"))
Sheets(2).Cells(m, 2) = Val(SendSCPI(ByVal datron2000, "WID?:2"))
Sheets(2).Cells(m, 3) = Val(SendSCPI(ByVal datron2000, "DLY?:2"))
Sheets(2).Cells(m, 4) = Val(SendSCPI(ByVal datron2000, "VHI?:1"))
Sheets(2).Cells(m, 5) = Val(SendSCPI(ByVal datron2000, "VLO?:1"))
Sheets(2).Cells(m, 6) = SendSCPI(ByVal datron2000, "INV?:1")
Sheets(2).Cells(m, 7) = Val(SendSCPI(ByVal datron2000, "VHI?:2"))
Sheets(2).Cells(m, 8) = Val(SendSCPI(ByVal datron2000, "VLO?:2"))
Sheets(2).Cells(m, 9) = SendSCPI(ByVal datron2000, "INV?:2")
Sheets(2).Cells(m, 10) = Val(SendSCPI(ByVal datron2000, "PER?"))
Sheets(2).Cells(m, 11) = 1

'Trigger Camera with HP33120
For l = 1 To FrameN
```

```
SendSCPI ByVal hp33120, "*TRG"
If Sheets(1).Cells(9, 12) = "y" Or Sheets(1).Cells(9, 12) = "Y" Then SendSCPI ByVal
tekscope, "ACQ:STATE RUN"
endTime = Timer + FrameInt
Do
DoEvents
If stopit = True Then GoTo line1
Loop Until endTime <= Timer

If Sheets(1).Cells(9, 12) = "y" Or Sheets(1).Cells(9, 12) = "Y" Then
SendSCPI ByVal tekscope, "SAV:WAVE CH1, C:\TekScope\waveforms\" +
LTrim(RTrim(Str(m))) + "rowwave.wfm"
SendSCPI ByVal tekscope, "*WAI"
End If

Next l
Next j
Next I

line1:
SendSCPI ByVal datron2000, "ZEROCHAN:1"
SendSCPI ByVal datron2000, "ZEROCHAN:2"
SendSCPI ByVal datron2000, "VLO:0.0m,1"
SendSCPI ByVal datron2000, "VHI:0.0m,1"
SendSCPI ByVal datron2000, "VLO:0.0m,2"
SendSCPI ByVal datron2000, "VHI:0.0m,2"

If Sheets(1).Cells(9, 12) = "y" Or Sheets(1).Cells(9, 12) = "Y" Then ClosePort ByVal
tekscope
ClosePort ByVal datron2000
ClosePort ByVal hp33120

Term_GPIB

End Sub
Private Function Init_GPIB()

ErrorStatus = viOpenDefaultRM(defaultRM)

End Function

Private Function Term_GPIB()

ErrorStatus = viClose(defaultRM)

End Function
```

```
Private Sub OpenPort(ByVal GPIB_Address As String, ByVal instrument As Long)

ErrorStatus = viOpen(defaultRM, "GPIB0::" & GPIB_Address & "::INSTR", 0, 1000,
instrument)
CheckError ByVal instrument, "Unable to open port"

End Sub

Private Function SendSCPI(ByVal instrument As Long, command As String) As String
Dim commandString As String
Dim ReturnString As String
Dim crlfpos As Integer
Dim ReadBuffer As String * 512
Dim actual As Long
commandString = command & Chr$(10)
ErrorStatus = viWrite(instrument, ByVal commandString, Len(commandString), actual)
CheckError ByVal instrument, "Can't write to Device"

   If InStr(commandString, "?") Then
      ErrorStatus = viRead(instrument, ByVal ReadBuffer, 512, actual)
      CheckError ByVal instrument, "Can't Read From Device"
      ReturnString = ReadBuffer
      crlfpos = InStr(ReturnString, Chr$(0))
      If crlfpos Then
         ReturnString = Left(ReturnString, crlfpos - 1)
      End If
      SendSCPI = ReturnString
   End If

End Function

Private Function ClosePort(ByVal instrument As Long)
ErrorStatus = viClose(instrument)
End Function

Private Function CheckError(ByVal instrument As Long, ErrorMessage As String)
If ErrorStatus < VI_SUCCESS Then
   Sheets(1).Cells(21, 6) = ErrorMessage
   ClosePort ByVal instrument
   End
End If
End Function

Sub ReSet()
```

```
Dim I As Integer

Sheets(1).Cells(21, 6) = ""
Sheets(1).Cells(28, 6) = ""
Sheets(1).Cells(29, 6) = ""
Sheets(2).Range("A2:IV1000").ClearContents

End Sub
```

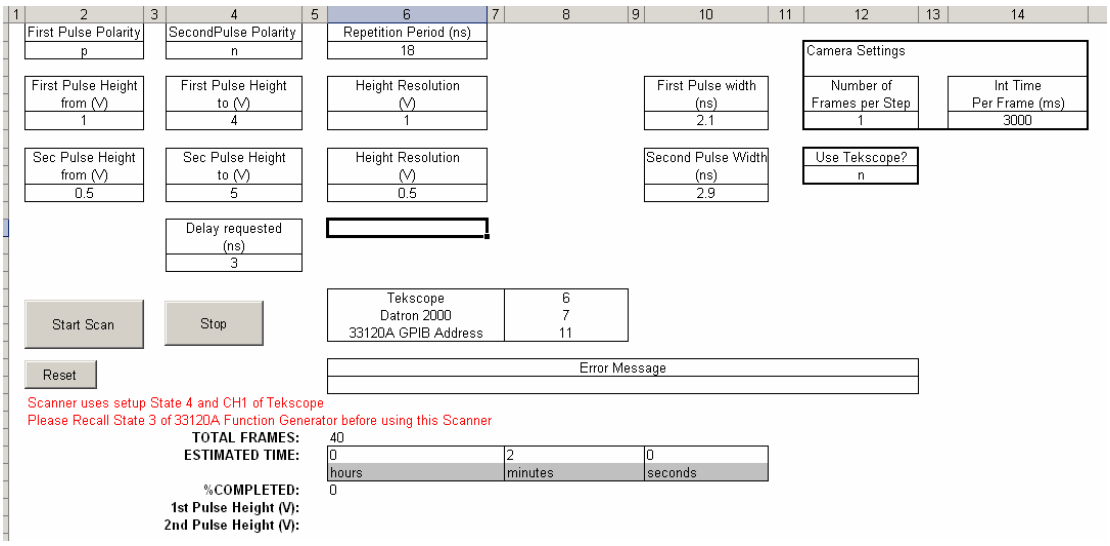
First Pulse Polarity
p
SecondPulse Polarity
n
Repetition Period (ns)
18
Camera Settings
First Pulse Height from (V)
1
First Pulse Height to (V)
4
Height Resolution (V)
1
First Pulse width (ns)
2.1
Number of Frames per Step
1
Int Time Per Frame (ms)
3000
Sec Pulse Height from (V)
0.5
Sec Pulse Height to (V)
5
Height Resolution (V)
0.5
Second Pulse Width (ns)
2.9
Use Tekscope?
n
Delay requested (ns)
3
Start Scan
Stop
Tekscope
Datron 2000
33120A GPIB Address
6
7
11
Reset
Error Message
Scanner uses setup State 4 and CH1 of Tekscope
Please Recall State 3 of 33120A Function Generator before using this Scanner
TOTAL FRAMES:
40
ESTIMATED TIME:
0
hours
2
minutes
0
seconds
%COMPLETED:
0
1st Pulse Height (V):
2nd Pulse Height (V):

REFERENCES

(1) Singh, J. *Optoelectronics: An Introduction to Materials and Devices;* McGraw Hill: New York, 1996.

(2) Lambe, J. and Jaklevic, R. C. Molecular vibration spectra by inelastic electron tunneling *Physical Review* **1968,** *165*, 821-32.

(3) Ratner, M. Molecular electronics: Pushing electrons around *Nature* **2000,** *404*, 137-138.

(4) Nitzan, A. and Ratner, M. A. Electron Transport in Molecular Wire Junctions *Science* **2003,** *300*, 1384-1389.

(5) Aviram, A. and Ratner, M. A. Molecular rectifiers *Chemical Physics Letters* **1974,** *29*, 277-283.

(6) Buttiker, M., Imry, Y., Landauer, R. and Pinhas, S. Generalized many-channel conductance formula with application to small rings *Physical Review B* **1985,** *31*, 6207-6215.

(7) Mujica, V., Nitzan, A., Datta, S., Ratner, M. A. and Kubiak, C. P. Molecular Wire Junctions: Tuning the Conductance *Journal Of Physical Chemistry B* **2003,** *107*, 91-95.

(8) Samanta, M. P., Tian, W., Datta, S., Henderson, J. I. and Kubiak, C. P. Electronic Conduction Through Organic Molecules *Physical Review B* **1996,** *53*, R7626.

(9) Jaklevic, R. C., Lambe, J., Kirtley, J. and Hansma, P. K. Structure At 0.8 Ev In Metal-Insulator-Metal Tunneling Junctions *Physical Review B* **1977,** *15*, 4103-4104.

(10) Khanna, S. K. and Lambe, J. Inelastic Electron-Tunneling Spectroscopy *Science* **1983,** *220*, 1345-1351.

(11) Lorente, N., Persson, M., Lauhon, L. J. and Ho, W. Symmetry Selection Rules for Vibrationally Inelastic Tunneling *Physical Review Letters* **2001,** *86*, 2593-2596.

(12) Persson, B. N. J. and Baratoff, A. Inelastic Electron Tunneling from a Metal Tip: The Contribution from Resonant Processes *Physical Review Letters* **1987,** *59*, 339.

(13) Olson, M., Mao, Y., Windus, T., Kemp, M., Ratner, M., Leon, N. and Mujica, V. A Conformational Study of the Influence of Vibrations on Conduction in Molecular Wires *Journal Of Physical Chemistry B* **1998,** *102*, 941-947.

(14) Segal, D., Nitzan, A., Ratner, M. and Davis, W. B. Activated conduction in microscopic molecular junctions *Journal Of Physical Chemistry B* **2000,** *104*, 2790-2793.

(15) Tian, W., Datta, S., Hong, S., Reifenberger, R., Henderson, J. I. and Kubiak, C. P. Conductance spectra of molecular wires *Journal Of Chemical Physics* **1998,** *109*, 2874-2882.

(16) Xue, Y., Datta, S. and Ratner, M. A. First-principles based matrix Green's function approach to molecular electronic devices: general formalism *Chemical Physics* **2002,** *281*, 151-170.

(17) Damle, P. S., Ghosh, A. W. and Datta, S. Unified Description of Molecular Conduction: From Molecules to Metallic Wires *Physical Review B* **2001,** *64*, 201403.

(18) Zhitenev, N. B., Meng, H. and Bao, Z. Conductance of Small Molecular Junctions *Physical Review Letters* **2002,** *88*, 226801-226804.

(19) Klein, D. L., McEuen, P. L., Katari, J. E. B., Roth, R. and Alivisatos, A. P. An approach to electrical studies of single nanocrystals *Applied Physics Letters* **1996,** *68*, 2574-2576.

(20) Chen, J., Reed, M. A., Rawlett, A. M. and Tour, J. M. Large on-off ratios and negative differential resistance in a molecular electronic device *Science* **1999,** *286*, 1550-1552.

(21) Reichert, J., Ochs, R., Beckmann, D., Weber, H. B., Mayor, M. and Löhneyse, H. v. Driving Current through Single Organic Molecules *Physical Review Letters* **2002,** *88*, 176804-176806.

(22) Reed, M. A., Zhou, C., Muller, C. J., Burgin, T. P. and Tour, J. M. Conductance of a molecular junction *Science* **1997,** *278*, 252-254.

(23) Park, H., Lim, A. K. L., Alivisatos, A. P., Park, J. and McEuen, P. L. Fabrication of metallic electrodes with nanometer separation by electromigration *Applied Physics Letters* **1999,** *75*, 301-303.

(24) Park, H., Park, J., Lim, A. K. L., Anderson, E. H., Alivisatos, A. P. and McEuen, P. L. Nanomechanical oscillations in a single-C60 transistor *Nature* **2000,** *407*, 58-60.

(25) Cui, X. D., Primak, A., Zarate, X., Tomfohr, J., Sankey, O. F., Moore, A. L., Moore, T. A., Gust, D., Harris, G. and Lindsay, S. M. Reproducible Measurement of Single-Molecule Conductivity *Science* **2001,** *294*, 571.

(26) Wold, D. J. and Frisbie, C. D. Fabrication and Characterization of Metal-Molecule-Metal Junctions by Conducting Probe Atomic Force Microscopy *Journal Of The American Chemical Society* **2001,** *123*, 5549.

(27) Xue, Y., Datta, S., Hong, S., Reifenberger, R., Henderson, J. I. and Kubiak, C. P. Negative differential resistance in the scanning-tunneling spectroscopy of organic molecules *Physical Review B* **1999,** *59*, R7852-R7855.

(28) Lauhon, L. J. and Ho, W. Electronic and vibrational excitation of single molecules with a scanning tunneling microscope *Science* **2000,** *451*, 219-225.

(29) Datta, S., Tian, W., Hong, S., Reifenberger, R., Henderson, J. I. and Kubiak, C. P. Current-voltage characteristics of self-assembled monolayers by scanning tunneling microscopy *Physical Review Letters* **1997,** *79*, 2530-2533.

(30) Donhauser, Z. J., Mantooth, B. A., Kelly, K. F., Bumm, L. A., Monnell, J. D., Stapleton, J. J., Price, D. W., Rawlett, A. M., Allara, D. L., Tour, J. M. and Weiss, P. S. Conductance Switching in Single Molecules Through Conformational Changes *Science* **2001,** *292*, 2303.

(31) Muller, C. J., Vleeming, B. J., Reed, M. A., Lamba, J. J. S., Hara, R., Jones, L. and Tour, J. M. Atomic probes: a search for conduction through a single molecule *Nanotechnology* **1996,** *7*, 409-411.

(32) Park, J., Pasupathy, A. N., Goldsmith, J. I., Chang, C., Yaish, Y., Petta, J. R., Rinkoski, M., Sethna, J. P., Abruna, H. D., McEuen, P. L. and Ralph, D. C. Coulomb blockade and the Kondo effect in single-atom transistors *Nature* **2002,** *417*, 722-725.

(33) Liang, W., Shores, M. P., Bockrath, M., Long, J. R. and Park, H. Kondo resonance in a single-molecule transistor *Nature* **2002,** *417*, 725-729.

(34) Pasupathy, A. N., Park, J., Chang, C., Soldatov, A. V., Lebedkin, S., Bialczak, R. C., Grose, J. E., Donev, L. A. K., Sethna, J. P., Ralph, D. C. and McEuen, P. L. Vibration-assisted electron tunneling in C-140 transistors *Nano Letters* **2005,** *5*, 203-207.

(35) Yu, L. H. and Natelson, D. The Kondo effect in C-60 single-molecule transistors *Nano Letters* **2004,** *4*, 79-83.

(36) Houck, A. A., Labaziewicz, J., Chan, E. K., Folk, J. A. and Chuang, I. L. Kondo effect in electromigrated gold break junctions *Nano Letters* **2005,** *5*, 1685-1688.

(37) Heersche, H. B., de Groot, Z., Folk, J. A., Kouwenhoven, L. P., van der Zant, H. S. J., Houck, A. A., Labaziewicz, J. and Chuang, I. L. Kondo effect in the presence of magnetic impurities *Physical Review Letters* **2006,** *96*, 017205.

(38) Sordan, R., Balasubramanian, K., Burghard, M. and Kern, K. Coulomb blockade phenomena in electromigration break junctions *Applied Physics Letters* **2005,** *87*, 013106.

(39) Lee, T. H., Gonzalez, J. I., Zheng, J. and Dickson, R. M. Single-molecule optoelectronics *Accounts Of Chemical Research* **2005,** *38*, 534-541.

(40) Lee, T. H., Gonzalez, J. I. and Dickson, R. M. Strongly enhanced field-dependent single-molecule electrolurninescence *Proceedings Of The National Academy Of Sciences Of The United States Of America* **2002,** *99*, 10272-10275.

(41) Reed, M. A., Zhou, C., Deshpande, M. R., Muller, C. J., Burgin, T. P., Jones, L., II and Tour, J. M. The electrical measurement of molecular junctions *Science* **1998,** *852*, 133-144.

(42) Hahn, J. R., Lee, H. J. and Ho, W. Electronic Resonance and Symmetry in Single-Molecule Inelastic Electron Tunneling *Physical Review Letters* **2000,** *85*, 1914-1917.

(43) Swanson, L. W. and Crouser, L. C. Total-energy distribution of field-emitted electrons and single-plane work functions for tungsten *Physical Review* **1967,** *163*, 622-41.

(44) Gadzuk, J. W. and Plummer, E. W. Field emission energy distribution (FEED) *Reviews of Modern Physics* **1973,** *45*, 487-548.

(45) Bagchi, A., Gomer, R. and Penn, D. R. Field emission total energy distribution in the presence of adsorbates *Science* **1974,** *40*, 555-8.

(46) Ho, P. S. and Kwok, T. Electromigration in metals *Reports on Progress in Physics* **1989,** *52*, 301-48.

(47) Lloyd, J. R. Electromigration in thin film conductors *Science* **1997,** *12*, 1177-1185.

(48) Gonzalez, J. I., Lee, T. H., Barnes, M. D., Antoku, Y. and Dickson, R. M. Quantum mechanical single-gold-nanocluster electroluminescent light source at room temperature *Physical Review Letters* **2004,** *93*, 147402.

(49) Gonzalez, J. I., Vosch, T. and Dickson, R. M. Asymmetric electrode-molecule transport dynamics tracked by nanoscale electroluminescence *Physical Review B* **2006,** Submitted.

(50) Xie, X. S. and Dunn, R. C. Probing Single-Molecule Dynamics *Science* **1994,** *265*, 361-364.

(51) Xie, X. S. Single-Molecule Spectroscopy and Dynamics at Room Temperature *Accounts of Chemical Research* **1996,** *29*, 598-606.

(52) Yang, H. and Xie, X. S. Probing single-molecule dynamics photon by photon *Journal Of Chemical Physics* **2002,** *117*, 10965-10979.

(53) Ha, T., Enderle, T., Chemla, D. S., Selvin, P. R. and Weiss, S. Single molecule dynamics studied by polarization modulation *Physical Review Letters* **1996,** *77*, 3979-3972.

(54) Dickson, R. M., Cubitt, A. B., Tsien, R. Y. and Moerner, W. E. On/off blinking and switching behaviour of single molecules of green fluorescent protein *Nature* **1997,** *388*, 355-358.

(55) Brown, R. and Orrit, M. *Spectral Jumps of Single Molecules;* Single Molecule Optical Detection, Imaging, and Spectroscopy*;* Verlag-Chemie: Munich, 1997.

(56) Ambrose, W. P. and Moerner, W. E. Fluorescence Spectroscopy and Spectral Diffusion of Single Impurity Molecules in a Crystal *Nature* **1991,** *349*, 225-227.

(57) Bartko, A. P., Xu, K. W. and Dickson, R. M. Three-dimensional single molecule rotational diffusion in glassy state polymer films *Physical Review Letters* **2002,** *89*, 026101.

(58) Kilin, S., Maevskaya, T. M., Nizovtsev, A. P., Shatokhin, V. N., Berman, P. R., Borczyskowski, C. v., Wrachtrup, J. and Fleury, L. Stochastic dynamics of a single impurity molecule from the viewpoint of continuous measurement theory *Physical Review A* **1998,** *57*, 1400.

(59) Zilker, S. J., Kador, L., Friebel, J., Vainer, Y. G., Kol'chenko, M. A. and Personov, R. I. Comparison of photon echo, hole burning, and single molecule spectroscopy data on low-temperature dynamics of organic amorphous solids *Journal Of Chemical Physics* **1998,** *109*, 6780-6790.

(60) Bauer, M. and Kador, L. Single-molecule spectra split by the interaction with two-level systems (TLSs) *Journal of Luminescence* **2004,** *107*, 32.

(61) Nie, S., Chiu, D. T. and Zare, R. N. Probing individual molecules with confocal fluorescence microscopy *Science* **1994,** *266*, 1018-21.

(62) Farrer, R. A., Previte, M. J. R., Olson, C. E., Peyser, L. A., Fourkas, J. T. and So, P. T. C. Single-molecule detection with a two-photon fluorescence microscope with fast-scanning capabilities and polarization sensitivity *Optics Letters* **1999,** *24*, 1832-1834.

(63) Plakhotnik, T., Donley, E. A. and Wild, U. P. Single-molecule spectroscopy *Annual Review of Physical Chemistry* **1997,** *48*, 181-212.

(64) Betzig, E. and Chichester, R. J. Single molecules observed by near-field scanning optical microscopy *Science* **1993,** *262*, 1422-1428.

(65) Ambrose, W. P., Goodwin, P. M., Martin, J. C. and Keller, R. A. Alterations of single molecule fluorescence lifetimes in near-field optical microscopy *Science* **1994,** *265*, 364-67.

(66) Moerner, W. E., Plakhotnik, T., Irngartinger, T., Wild, U. P., Pohl, D. W. and Hecht, B. Near-Field Optical Spectroscopy of Individual Molecules in Solids *Physical Review Letters* **1994,** *73*, 2764-2767.

(67) Empedocles, S. A., Neuhauser, R. and Bawendi, M. G. Three-dimensional orientation measurements of symmetric single chromophores using polarization microscopy *Nature* **1999,** *399*, 126-130.

(68) Kumar, P., Mehta, A., Dadmun, M. D., Zheng, J., Peyser, L., Bartko, A. P., Dickson, R. M., Thundat, T., Sumpter, B. G., Noid, D. W. and Barnes, M. D. Narrow-bandwidth spontaneous luminescence from oriented semiconducting polymer nanostructures *Journal Of Physical Chemistry B* **2003,** *107*, 6252-6257.

(69) Deniz, A. A., Laurence, T. A., Beligere, G. S., Dahan, M., Martin, A. B., Chemla, D. S., Dawson, P. E., Schultz, P. G. and Weiss, S. Single-molecule protein folding: Diffusion fluorescence resonance energy transfer studies of the denaturation of chymotrypsin inhibitor 2 *Proceedings Of The National Academy Of Sciences Of The United States Of America* **2000,** *97*, 5179-5184.

(70) Ha, T., Enderle, T., Ogletree, D. F., Chemla, D. S., Selvin, P. R. and Weiss, S. Probing the interaction between two single molecules: Fluorescence resonance energy transfer between a single donor and a single acceptor *Proceedings of the National Academy of Sciences, USA* **1996,** *93*, 6264-6268.

(71) Grunwell, J. R., Glass, J. L., Lacoste, T. D., Deniz, A. A., Chemla, D. S. and Schultz, P. G. Monitoring the conformational fluctuations of DNA hairpins using single-pair fluorescence resonance energy transfer *Journal Of The American Chemical Society* **2001,** *123*, 4295-4303.

(72) Xie, X. S. and Lu, H. P. Single-molecule enzymology *Journal of Biological Chemistry* **1999,** *274*, 15967-15970.

(73) Yang, H. and Xie, X. S. Statistical approaches for probing single-molecule dynamics photon-by-photon *Chemical Physics* **2002,** *284*, 423-437.

(74) O'Shea, D., Callen, W. and Rhodes, W. *An introduction to lasers and their applications;* Addison-Wesley Publishing Company: Reading, MA, 1978.

(75) Pankove, J. I. Tunneling-Assisted Photon Emission in Gallium Arsenide pn Junctions *Physical Review Letters* **1962,** *9*, 283.

(76) Jaklevic, R. C. and Lambe, J. Molecular vibration spectra by electron tunneling *Physical Review Letters* **1966,** *17*, 1139-40.

(77) Lambe, J. and McCarthy, S. L. Light emission from inelastic electron tunneling *Physical Review Letters* **1976,** *37*, 923-5.

(78) McCarthy, S. L. and Lambe, J. Enhancement of light emission from metal-insulator-metal tunnel junctions *Applied Physics Letters* **1977,** *30*, 427-9.

(79) Hansma, P. K. and Broida, H. P. Light Emission from Gold Particles Excited by Electron Tunneling *Applied Physics Letters* **1978,** *32*, 545.

(80) de Chevigne, S., Klein, J., Leger, A., Belin, M. and Defourneau, D. Molecular Electronic Transitions Observed by Inelastic Tunneling Spectroscopy *Physical Review B* **1977,** *15*, 750.

(81) Jaklevic, R. C. and Lambe, J. Inelastic tunneling due to vibrational modes of yttrium and chromium oxides *Physical Review B* **1970,** *[3]2*, 808-12.

(82) Zheng, J., Zhang, C. and Dickson, R. M. Highly fluorescent, water-soluble, size-tunable gold quantum dots *Physical Review Letters* **2004,** *93*, 077402.

(83) Zheng, J. *Ph. D. Thesis;* Georgia Institute of Technology: Atlanta, GA, 2005.

(84) Zheng, J. and Dickson, R. M. Individual water-soluble dendrimer-encapsulated silver nanodot fluorescence *Journal Of The American Chemical Society* **2002,** *124*, 13982-13983.

(85) Petty, J. T., Zheng, J., Hud, N. V. and Dickson, R. M. DNA-Templated Ag Nanocluster Formation *Journal Of The American Chemical Society* **2004,** *126*, 5207-5212.

(86) Korotkov, A. N. Coulomb blockade and digital single-electron devices *Molecular Electronics* **1997,** 157-189.

(87) Metzger, R. M. and Cava, M. P. *Rectification by a single molecule of hexadecylquinolinium tricyanoquinodimethanide;* Molecular Electronics: Science and Technology*;* 1998.

(88) Avouris, P. Molecular Electronics with Carbon Nanotubes *Accounts of Chemical Research* **2002,** *35*, 1026-1034.

(89) Mujica, V., Kemp, M., Roitberg, A. and Ratner, M. Current-voltage characteristics of molecular wires: Eigenvalue staircase, Coulomb blockade, and rectification *Journal Of Chemical Physics* **1996,** *104*, 7296-7305.

(90) Barner, J. B. and Ruggiero, S. T. Observation of the incremental charging of silver particles by single electrons *Physical Review Letters* **1987,** *59*, 807-10.

(91) Jiang, C. S., Nakayama, T. and Aono, M. Spatially resolved observation of Coulomb blockade and negative differential conductance on a Ag cluster on the clean GaAs(110) surface *Applied Physics Letters* **1999,** *74*, 1716-1718.

(92) Fowler, R. H. and Nordheim, L. Electron emission in intense electric fields *Proceedings Of The Royal Society Of London Series A-Containing Papers Of A Mathematical And Physical Character* **1928,** *119*, 173-181.

(93) Yuan, Z. L., Kardynal, B. E., Stevenson, R. M., Shields, A. J., Lobo, C. J., Cooper, K., Beattie, N. S., Ritchie, D. A. and Pepper, M. Electrically driven single-photon source *Science* **2002,** *295*, 102-105.

(94) Gudiksen, M. S., Maher, K. N., Ouyang, L. and Park, H. Electroluminescence from a Single-Nanocrystal Transistor *Nano Letters* **2005,** *5*, 2257-2261.

(95) Lee, H. J. and Ho, W. Structural determination by single-molecule vibrational spectroscopy and microscopy: Contrast between copper and iron carbonyls *Physical Review B* **2000,** *61*, R16347-R16350.

(96) Nilius, N., Wallis, T. M. and Ho, W. Vibrational spectroscopy and imaging of single molecules: Bonding of CO to single palladium atoms on NiAl(110) *Journal Of Chemical Physics* **2002,** *117*, 10947-10952.

(97) Lee, T.-H. and Dickson, R. M. Single-Molecule LEDs from Nanoscale Electroluminescent Junctions *Journal Of Physical Chemistry B* **2003,** *107*, 7387-7390.

(98) Lee, T. H. and Dickson, R. M. Discrete two-terminal single nanocluster quantum optoelectronic logic operations at room temperature *Proceedings Of The National Academy Of Sciences Of The United States Of America* **2003,** *100*, 3043-3046.

(99) Schimschak, M. and Krug, J. Electromigration-Induced Breakup of Two-Dimensional Voids *Physical Review Letters* **1998,** *80*, 1674-1677.

(100) Irissou, E., Denis, M. C., Chaker, M. and Guay, D. Gold oxide thin film grown by pulsed laser deposition in an O-2 atmosphere *Thin Solid Films* **2005,** *472*, 49-57.

(101) Juodkazis, K., Juodkazyte, J., Jasulaitiene, V., Lukinskas, A. and Sebeka, B. XPS studies on the gold oxide surface layer formation *Electrochemistry Communications* **2000,** *2*, 503-507.

(102) Vosch, T., Cotlet, M. and Hofkens, J. *Journal of Physical Chemistry A* **2003,** *107*, 6920.

(103) The average injection efficiency for one cluster was measured by exciting the EL with pulse-pairs of opposite polarity at varying repetition rates. A ~±1.5 VAC field (measured into 50Ω) produces approximately 1 photon for every 5000 excitation periods.

(104) Moerner, W. E. and Kador, L. Optical detection and spectroscopy of single molecules in a solid *Physical Review Letters* **1989,** *62*, 2535-38.

(105) Reilly, P. D. and Skinner, J. L. Spectral diffusion of single molecule fluorescence: a probe of low-frequency localized excitations in disordered crystals *Physical Review Letters* **1993,** *71*, 4257-4260.

(106) Orrit, M., Bernard, J. and Personov, R. I. High-Resolution Spectroscopy of Organic Molecules in Solids: From Fluorescence Line Narrowing and Hole Burning to Single Molecule Spectroscopy *Journal Of Physical Chemistry* **1993,** *97*, 10256-10268.

(107) Basché, T., Kummer, S. and Bräuchle, C. Direct Spectroscopic Observation of Quantum Jumps of a Single Molecule *Nature* **1995,** *373*, 132-134.

(108) Dickson, R. M., Norris, D. J., Tzeng, Y.-L. and Moerner, W. E. Three Dimensional Imaging of Single Molecules in Pores of Poly(acrylamide) Gels *Science* **1996,** *274*, 966-69.

(109) Novotny, L. Single molecule fluorescence in inhomogeneous environments *Applied Physics Letters* **1996,** *69*, 3806-3808.

(110) Ruiter, A. G. T., Veerman, J. A., Garcia-Parajo, M. F. and van Hulst, N. F. Single molecule rotational and translational diffusion observed by near-field scanning optical microscopy *Journal of Physical Chemistry A* **1997,** *101*, 7318-7323.

(111) Ha, T., Glass, J., Enderle, T., Chemla, D. S. and Weiss, S. Hindered Rotational Diffusion and Rotational Jumps of Single Molecules *Physical Review Letters* **1998,** *80*, 2093-2096.

(112) Zheng, J., Petty, J. T. and Dickson, R. M. High Quantum Yield Blue Emission from Water-Soluble Au_8 Nanodots *Journal Of The American Chemical Society* **2003,** *125*, 7780-7781.

(113) Wilcoxon, J. P., Martin, J. E., Parsapour, F., Wiedenman, B. and Kelley, D. F. Photoluminescence from nanosize gold clusters *Journal Of Chemical Physics* **1998,** *108*, 9137-9143.

(114) Li, J., Li, X., Zhai, H. J. and Wang, L. S. Au-20: A tetrahedral cluster *Science* **2003,** *299*, 864-867.

(115) Clemenger, K. Ellipsoidal Shell Structure in Free-Electron Metal-Clusters *Physical Review B* **1985,** *32*, 1359-1362.

(116) Deheer, W. A. The Physics of Simple Metal-Clusters - Experimental Aspects and Simple-Models *Reviews of Modern Physics* **1993,** *65*, 611-676.

(117) Lin, Z. Y., Kanters, R. P. F. and Mingos, D. M. P. Closed-Shell Electronic Requirements for Condensed Clusters of the Group-11 Elements *Inorganic Chemistry* **1991,** *30*, 91-95.

(118) Hakkinen, H. and Landman, U. Gold clusters (Au-N, 2 <= N <= 10) and their anions *Physical Review B* **2000,** *62*, R2287-R2290.

(119) Palpant, B., Prevel, B., Lerme, J., Cottancin, E., Pellarin, M., Treilleux, M., Perez, A., Vialle, J. L. and Broyer, M. Optical properties of gold clusters in the size range 2-4 nm *Physical Review B* **1998,** *57*, 1963-1970.

(120) Schlesser, R., McClure, M. T., McCarson, B. L. and Sitar, Z. Mechanisms of field emission from diamond coated Mo emitters *Diamond and Related Materials* **1998,** *7*, 636-639.

(121) McCarson, B. L., Schlesser, R. and Sitar, Z. Field emission energy distribution analysis of cubic-BN-coated Mo emitters: Nonlinear behavior *Journal of Applied Physics* **1998,** *84*, 3382-3385.

(122) Bennett, C. H. and DiVincenzo, D. P. Quantum information and computation *Nature* **2000,** *404*, 247-255.

(123) Bennett, C. H. and Brassard, G. *Quantum cryptography: Public key distribution and coin tossing;* Proceedings of the IEEE International Conference on Copmputers, systems, and Signal Processing*;* Bangalore, India, 1984.

(124) Beveratos, A., Brouri, R., Gacoin, T., Villing, A., Poizat, J.-P. and Grangier, P. Single Photon Quantum Cryptography *Physical Review Letters* **2002,** *89*, 187901.

(125) Ekert, A. K. Quantum Cryptography Based On Bell Theorem *Physical Review Letters* **1991,** *67*, 661-663.

(126) Bennett, C. H. and DiVincenzo, D. P. Quantum Computing: Towards an engineering era? *Nature* **1995,** *377*, 389-90.

(127) Torma, P. and Stenholm, S. Quantum logic using polarized photons *Physical Review A: Atomic, Molecular, and Optical Physics* **1996,** *54*, 4701-4706.

(128) McKeever, J., Boca, A., Boozer, A. D., Miller, R., Buck, J. R., Kuzmich, A. and Kimble, H. J. Deterministic generation of single photons from one atom trapped in a cavity *Science* **2004,** *303*, 1992-1994.

(129) Kuzmich, A., Bowen, W. P., Boozer, A. D., Boca, A., Chou, C. W., Duan, L. M. and Kimble, H. J. Generation of nonclassical photon pairs for scalable quantum communication with atomic ensembles *Nature* **2003,** *423*, 731-734.

(130) Kimble, H. J., Dagenais, M. and Mandel, L. Photon Anti-Bunching In Resonance Fluorescence *Physical Review Letters* **1977,** *39*, 691-695.

(131) Duan, L. M., Lukin, M. D., Cirac, J. I. and Zoller, P. Long-distance quantum communication with atomic ensembles and linear optics *Nature* **2001,** *414*, 413-418.

(132) Scully, M. O. and Zubairy, M. S. *Quantum Optics;* Cambridge University Press: Cambridge, 1997.

(133) Loudon, R. *The Quantum Theory of Light;* Clarendon: Oxford, 1983.

(134) Muller, A., Zbinden, H. and Gisin, N. Quantum cryptography over 23 km in installed under-lake telecom fiber *Europhysics Letters* **1996,** *33*, 335-9.

(135) Carmichael, H. J. Photon Antibunching And Squeezing For A Single Atom In A Resonant Cavity *Physical Review Letters* **1985,** *55*, 2790-2793.

(136) Schubert, M., Siemers, I., Blatt, R., Neuhauser, W. and Toschek, P. E. Photon Antibunching And Non-Poissonian Fluorescence Of A Single 3-Level Ion *Physical Review Letters* **1992,** *68*, 3016-3019.

(137) Lyublinskaya, I. E. and Vyas, R. Single-Atom Fluorescence With Nonclassical Light *Physical Review A* **1993,** *48*, 3966-3979.

(138) Brunel, C., Lounis, B., Tamarat, P. and Orrit, M. Triggered source of single photons based on controlled single molecule fluorescence *Physical Review Letters* **1999,** *83*, 2722-2725.

(139) Lounis, B. and Moerner, W. E. Single photons on demand from a single molecule at room temperature *Nature* **2000,** *407*, 491-493.

(140) Kumar, P., Lee, T. H., Mehta, A., Sumpter, B. G., Dickson, R. M. and Barnes, M. D. Photon antibunching from oriented semiconducting polymer nanostructures *Journal Of The American Chemical Society* **2004,** *126*, 3376-3377.

(141) Huser, T., Yan, M. and Rothberg, L. J. Single chain spectroscopy of conformational dependence of conjugated polymer photophysics *Proceedings Of The National Academy Of Sciences Of The United States Of America* **2000,** *97*, 11187-11191.

(142) Beveratos, A., Brouri, R., Gacoin, T., Poizat, J. P. and Grangier, P. Nonclassical radiation from diamond nanocrystals *Physical Review A* **2001,** *6406*,

(143) Kurtsiefer, C., Mayer, S., Zarda, P. and Weinfurter, H. Stable solid-state source of single photons *Physical Review Letters* **2000,** *85*, 290-293.

(144) Michler, P., Imamoglu, A., Mason, M. D., Carson, P. J., Strouse, G. F. and Buratto, S. K. Quantum correlation among photons from a single quantum dot at room temperature *Nature* **2000,** *406*, 968-970.

(145) Michler, P., Kiraz, A., Becher, C., Schoenfeld, W. V., Petroff, P. M., Zhang, L. D., Hu, E. and Imamoglu, A. A quantum dot single-photon turnstile device *Science* **2000,** *290*, 2282-+.

(146) Moreau, E., Robert, I., Gerard, J. M., Abram, I., Manin, L. and Thierry-Mieg, V. Single-mode solid-state single photon source based on isolated quantum dots in pillar microcavities *Applied Physics Letters* **2001,** *79*, 2865-2867.

(147) Misewich, J. A., Martel, R., Avouris, P., Tsang, J. C., Heinze, S. and Tersoff, J. Electrically induced optical emission from a carbon nanotube FET *Science* **2003,** *300*, 783-786.

(148) Gudiksen, M. S., Lauhon, L. J., Wang, J., Smith, D. C. and Lieber, C. M. Growth of nanowire superlattice structures for nanoscale photonics and electronics *Nature* **2002,** *415*, 617-620.

(149) Brown, R. H. and Twiss, R. Q. Question Of Correlation Between Photons In Coherent Light Rays *Nature* **1956,** *178*, 1447-1448.

(150) Lee, T. H., Kumar, P., Mehta, A., Xu, K. W., Dickson, R. M. and Barnes, M. D. Oriented semiconducting polymer nanostructures as on-demand room-temperature single-photon sources *Applied Physics Letters* **2004,** *85*, 100-102.

(151) Zrenner, A. A close look on single quantum dots *Journal Of Chemical Physics* **2000,** *112*, 7790-7798.

(152) Lambe, J. and Jaklevic, R. C. Inelastic Tunneling *Solid State Communications* **1967,** *5*, R16-&.

(153) Young, R. D. and Muller, E. W. Experimental measurement of the total-energy distribution of field-emitted electrons *Physical Review* **1959,** *113*, 115-20.

(154) Young, R. D. Theoretical total-energy distribution of field-emitted electrons *Physical Review* **1959,** *113*, 110-14.

(155) Bell, A. E. and Swanson, L. W. Total energy distributions of field-emitted electrons at high current density *Physical Review B* **1979,** *19*, 3353-64.

(156) Yokoyama, H., Suzuki, M. and Nambu, Y. Spontaneous Emission and Laser Oscillation Properties of Microcavities Containing a Dye Solution *Appl. Phys. Lett.* **1991,** *58*, 2598.

(157) Barnes, M. D., Whitten, W. B., Arnold, S. and Ramsey, J. M. Homogeneous linewidths of Rhodamine 6G at room temperature from cavity-enhanced spontaneous emission rates *Journal Of Chemical Physics* **1992,** *97*, 7842.

(158) Barnes, M. D., Whitten, W. B. and Ramsey, J. M. Probing femtosecond dynamics in solution on a picosecond time scale. Cavity enhancement of spontaneous emission rates in microdroplets *Chemical Physics Letters* **1994,** *227*, 628.

(159) Klimov, V. I., Mikhailovsky, A. A., Xu, S., Malko, A., Hollingsworth, J. A., Leatherdale, C. A., Eisler, H.-J. and Bawendi, M. G. Optical gain and stimulated emission in nanocrystal quantum dots *Science* **2000,** *290*, 314.

(160) Caruge, J. M., Chan, Y., Sundar, V., Eisler, H.-J. and Bawendi, M. G. Transient photoluminescence and simultaneous amplified spontaneous emission from multiexciton states in CdSe quantum dots *Physical Review B* **2004,** *70*, 085316.

VITA

Jose I. Gonzalez is a native of Barranquilla, Colombia and moved to the United States in 1987. He attended Chattahoochee high school in Alpharetta, GA. As an undergraduate, he conducted research under Suzanne Shuker at GA Tech and Andrei Tokmakoff at MIT. Jose received B.S. degrees in chemistry and mathematics from the Massachusetts Institute of Technology in 2001 and finished his Ph.D. at the Georgia Institute of Technology under Prof. Robert Dickson in 2006.